List of Contributors

Eric Akkermans
Department of Physics,
Israel Institute of Technology,
Technion City 32000, Israel
eric@physics.technion.ac.il

Eric Anglaret
Groupe de Dynamique des Phases Condensées (UMR 5581),
University Montpellier II,
34095 Montpellier, Cedex 5 France
eric@gdpc.univ-montp2.fr

François Béguin
Centre de Recherche sur la Matière Divisée, CNRS-Université d'Orléans,
1B rue de la Férollerie,
45071 Orléans Cedex 02, France
beguin@cnrs-orleans.fr

Xavier Blase
Laboratoire de Physique de la Matière Condensée et Nanostructures, CNRS and Université Lyon I,
43 bld du 11 novembre 1918, 69622 Villeurbanne, France
xblase@lpmcn.univ-lyon1.fr

Jean-Marc Bonard
Rolex S.A., 3-7, rue François-Dussaud, CH-1211 Genève 24,
Switzerland
jmbonard@gmx.ch

Sylvie Bonnamy
Centre de Recherche sur la Matière Divisée (UMR CNRS 6619)
1b rue de la Férollerie
45071, Orléans Cedex 2, France
bonnamy@cnrs-orleans.fr

Jean-Christophe Charlier
Unité PCPM., Université Catholique de Louvain, Place Croix du Sud, 1 (Boltzmann)
1348 Louvain-la-Neuve, Belgium
charlier@pcpm.ucl.ac.be

Olivier Chauvet
Institut des Matériaux J. Rouxel
2 rue de la Houssinière
44322 Nantes, France
chauvet@cnrs-imn.fr

Pierre Delhaès
Centre de Recherche Paul Pascal (UPR CNRS 8641)
Université Bordeaux-I
Avenue Schweitzer, 33600, Pessac, France
delhaes@crpp-bordeaux.cnrs.fr

Georges Désarmot
ONERA,
29 avenue de la Division Leclerc,
92322 Châtillon cedex, France
Georges.Desarmot@onera.fr

François Ducastelle
Laboratoire d'Etude des Microstructures, ONERA-CNRS, BP72, 92322 Châtillon Cedex, France
Francois.Ducastelle@onera.fr

Emmanuel Flahaut
CIRIMAT - UMR CNRS 5085,
Université Paul Sabatier,
118 Route de Narbonne, Bâtiment 2R1,
31062 TOULOUSE Cedex 04,
France
flahaut@chimie.ups-tlse.fr

Patrice Gadelle
Laboratoire de Thermodynamique et Physico-Chimie Métallurgiques, CNRS-INPG-UJF, ENSEEG, BP 75, 38402 St Martin d'Hères, France

Catherine Gauthier
GEMPPM, CNRS, INSA Lyon
7 avenue Capelle,
69621 Villeurbanne cedex, France
Catherine.Gauthier@insa-lyon.fr

Frank Hekking
LPMMC-CNRS
25 avenue des Martyrs
38042 Grenoble, France
hekking@grenoble.cnrs.fr

Jean-Paul Issi
PCPM, Univ. Louvain la Neuve,
Place Croix du Sud, 1
(Bât. Boltzmann)
B-1348 Louvain-la-Neuve, Belgium
issi@pcpm.ucl.ac.be

Catherine Journet
Laboratoire de Physique de la Matière Condensée et Nanostructures, CNRS and Université Lyon I, 43 bld du 11 novembre 1918, 69622 Villeurbanne, France
cjournet@lpmcn.univ-lyon1.fr

Philippe Lambin
Département de Physique, FUNDP,
61 Rue de Bruxelles
B5000 Namur, Belgium
philippe.lambin@fundp.ac.be

Pascale Launois
Laboratoire de Physique des Solides,
Université Paris-Sud (Bât. 510)
91405 Orsay, France
launois@lps.u-psud.fr

Christophe Laurent
Centre Interuniversitaire de Recherche et d'Ingénierie des Matériaux, UMR CNRS 5085, Toulouse, France
laurent@chimie.ups-tlse.fr

Angel Linares-Solano
Departamento de Química Inorgánica, Universidad de Alicante,
Apartado 99,
E-03080, Alicante, Spain
linares@ua.es

Annick Loiseau
LEM, ONERA BP 72,
Avenue de la Division Leclerc
F92322 Châtillon, France
annick.loiseau@onera.fr

Richard Martel
University of Montréal,
C.P. 6128 Succursale Centre-ville
Montral (QC) Canada H3C-3J7
r.martel@umontreal.ca

Gilles Montambaux
Laboratoire de Physique des Solides,
Université Paris-Sud (Bât. 510)
91405 Orsay, France
montambaux@lps.fr

Marc Monthioux
CEMES BP 4347,
29 Rue Jeanne Marvig
F31055 Toulouse Cedex 4, France
marc.monthioux@cemes.fr

Alain Peigney
Centre Interuniversitaire de Recherche et d'Ingénierie des Matériaux, UMR CNRS 5085, Toulouse, France
peigney@chimie.ups-tlse.fr

Pierre Petit
Institut Charles Sadron, 6 rue Bousaingault, 67083 Strasbourg, France
Petit@ics.u-strasbg.fr

Jean Pinson
Alchimer,
15 rue du Buisson aux Fraises,
91300 Massy, France
jean.pinson@alchimer.com

Philippe Poncharal
GDPC UMR 5581,
Université Montpellier II
5 place Eugène Bataillon
34095 Montpellier cedex 5, France
Poncharal@gdpc.univ-montp2.fr

Philippe Poulin
CRPP, CNRS, Université Bordeaux I
Avenue Albert Schweitzer,
33600 Pessac, France
poulin@crpp-bordeaux.cnrs.fr

Stephan Roche
Commissariat à l'Energie Atomique,
DSM/DRFMC/SPSMS
17 avenue des Martyrs
38054 Grenoble, France
stephan.roche@cea.fr

Stéphane Rols
Groupe de Dynamique des Phases Condensées (UMR 5581),
University Montpellier II,
34095 Montpellier, Cedex 5 France
rols@gdpc.univ-montp2.fr

Jean-Paul Salvetat
CRMD, CNRS, Université d'Orléans
1B rue de la Férollerie,
45071 Orléans cedex 2, France
salvetat@cnrs-orleans.fr

Jean-Louis Sauvajol
Groupe de Dynamique des Phases Condensées (UMR 5581),
University Montpellier II,
34095 Montpellier, Cedex 5 France
sauva@gdpc.univ-montp2.fr

Odile Stephan
Laboratoire de Physique des Solides,
Batiment 510,
University Paris-Sud 91405 Orsay Cedex, France
stephan@lps.u-psud.fr

Jany Thibault
CEA-DRFMC,
17 Rue des Martyrs
F38054 Grenoble, France
jthibault@cea.fr

Synthesis Methods and Growth Mechanisms

A. Loiseau, X. Blase, J.-Ch. Charlier, P. Gadelle, C. Journet, Ch. Laurent and A. Peigney

Summary. In this chapter, our purpose is to present how carbon nanotubes are synthesized and how their formation and growth can be studied, understood and modelized. The identification of what we call carbon nanotubes today is dated from 1991 thanks to the work of S. Iijima. However the story of their synthesis is a sequence of serendipities in the expansion of synthesis routes to C_{60} molecules and to carbon fibers which merits to be evoked in this introduction in order to explain the organisation of this chapter.

The C_{60} molecule was discovered in 1985 by Kroto, Smalley and co-workers [1] thanks to an original synthesis set up which consists in ablating a graphite target with an energetic pulsed laser. However, the full expansion of the synthesis and the research on fullerenes did not truly begin until the mass production of these material was invented by Krätschmer and Huffman in 1990 [2]. The principle of this synthesis route was ingeniously simple and cheap since it consisted to establish an electric arc between two electrodes made in graphite under an helium atmosphere. Therefore, it has been popularized immediately and research groups all over the world built carbon-arc fullerene generators and started to investigate the C60 molecules.

This could be the happy end of the success story. In fact, the publication by Krätschmer and Huffman was only its beginning. It soon turned out that there were other cage structures to be found in the soot produced by the electric arc, like C_{70}, which looks a bit like a rugby-ball. Even more interesting, when the carbon arc power supply was changed to direct current instead of alternating current, strange filamentous structures could be found in one of the electrode deposits. Nobody cares on this deposit until S. Iijima looked at it in his high resolution transmission electron microscope in 1991 [3]. He observed and indentified tubular structures entirely made out of perfectly crystallized carbon and named them nanotubes, referring to their diameters, which were only a few nanometers wide. The structure of these objects attracted immediately a general attention from the research community so that the publication of S. Iijima can be considered as a true breakpoint in the history of carbon.

This is even more remarkable that tubular carbon structures turn out not to have been observed for the first time in 1991. Indeed, such structures are known since at least the 60s and the work by Bacon [4] under the generic name of filaments or carbon fibers. They were at the beginning a non desired by-product in industrial chemical processes. The diameter of the filaments is typically less than 100 nm and can be as small as a few nm as attested by the observations of M. Endo in transmission electron microscopy in the seventies [5]. The thinner filaments were therefore very close to the present nanotubes. However, their observation did not attract so much attention because at that time there was no way to study and to

use objects so small in size. This context was completely changed in the nineties and explains the expansion of the research after the observations of S. Iijima. But there is even more. Catalytic chemical vapour deposition (CCVD) processes, which are the synthesis route to filamentous carbon par excellence, have then been adapted to the synthesis of carbon nanotubes and are now able to produce mm long single wall nanotubes. More, because of their flexibility and their facility to be scaled up, they are promished to become the major way for synthesizing in a controlled way carbon nanotubes.

Today, it is very easy to synthesize nanotubes since several methods have been devised to produce carbon nanotubes (CNT) since 1991. Very generally, they can be classified into two main categories depending if they are running at high or at medium temperatures. High temperature routes are, as the electric arc method, based on the vaporization of a graphite target whereas medium temperature routes are based on CCVD processes. They are successively described in this chapter (Sect. 1 and Sect. 3) with for the latter an introductory section giving to the reader the basic notions of CCVD growth of filamentous carbon (Sect. 2). The panorama of high temperature methods is completed by a presentation of their use and their adaptation to the synthesis of parent BN nanotubes.

Sections 4 and 5 are devoted to the formation and growth mechanisms of these objects. Since all their properties are directly related to the atomic structure of the tube, it is essential to understand what controls nanotube size, the number of shells, the helicity and the structure during the synthesis. A thorough understanding of the formation mechanisms for these nanotubular carbon systems is crucial to design procedures for controlling the growth conditions to obtain more practical structures which might be directly available for applications. Section 4 focuses on carbon single wall nanotubes (C-SWNTs) and aims at understanding why this kind of nanotubes, – in contrast to carbon multi-wall nanotubes (C-MWNTs) –, can only be produced with the help of a metallic catalyst whatever the synthesis process. It presents a comprehensive and phenomenological analysis of their formation and growth based on different experimental investigations either done in situ during the synthesis or performed on the synthesis products after the synthesis. Sect. 5 presents the numerical simulations of the growth mechanisms of C MWNTs and SWNTs using ab initio and semi-empirical methods. In the final section (Sect. 6), this panorama is completed by the analysis of growth of $B_xC_yN_z$ nanotubes and the numerical simulations peformed for these parent objects.

1 High Temperature Methods for the Synthesis of Carbon and Boron Nitride MWNTs and SWNTs

1.1 Generalities on High Temperature Methods

High temperature methods are directly issued from the historical carbon-arc process invented by Krätschmer and Huffman in 1990 [2] for the production of fullerenes. They all involve sublimating graphite in a reduced atmosphere or rare (inert) gases, brought to temperatures above 3200C - that is the temperature of sublimation of graphite - , and condensing the resulting vapour under a high temperature gradient. What differentiates the various processes

is the method used for sublimating graphite. This can be an electric arc formed between two electrodes made in graphite, an ablation induced by a pulsed laser or a vaporization induced by a solar or a continuous laser beam. These processes are described in detail in the following sections.

1.2 The Electric Arc Discharge Technique

In his initial experiment, S. Iijima [3] used a DC arc discharge in argon consisting of a set of carbon electrodes. The discharge temperature was in the range of 2000-3000°C at nominal conditions of 100 Amps and 20 volts. This apparatus produced multiwall nanotubes in the soot. Later, single-walled carbon nanotubes were grown with the same set-up but by adding to the electrodes suitable catalyst particles, e.g. of Fe, Co, Ni or rare-earth metals.

Principle and Description

This method is a slightly modified version of the method used for fullerene production. An arc discharge is generated between two graphite electrodes placed face to face in the machine's principle airtight chamber (Fig. 1) under a partial pressure of helium or argon (typically 600 mbar). The electrical discharge that results brings the temperature up to 6000 °C. This is hot enough for the carbon contained in the graphite to sublimate - that is, transform from a solid state to gaseous one without turning into a liquid first. During the sublimation, pressure runs very high, ejecting carbon atoms from the solid and form a plasma. These atoms head toward colder zones within the chamber, allowing a nanotube deposit to accumulate on the cathode. The type of nanotube that is formed depends crucially upon the presence of

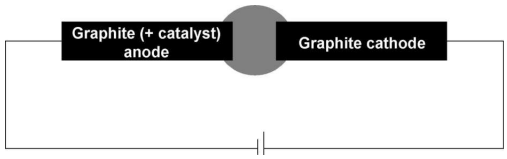

Fig. 1. Principle of the electric arc discharge technique

metal catalysts. If small amounts of transition metals such as Fe, Co, Ni or Y are introduced in the target graphite, then single-wall carbon nanotubes are the dominant product. In the absence of such catalysts, the formation of multiwall carbon nanotubes is favoured.

In Situ Diagnoses

In situ diagnostics during growth of carbon nanotubes are quite difficult to carry out in an electric arc apparatus. However methodologies for determin-

ing the temperature in the arc process for SWNTs production have been investigated by a few groups.

Generally, a lens, located about 30 or 40 cm from the centre of the arc chamber, collects light through a window in the side of the chamber. The lens focuses an image of the arc on a focal plane at which an optical fibre is located. The fibre then transfers the light from a particular spot on the image to a spectrometer. This spectrometer is used to analyse radiations emitted during the arc discharge from catalyst atomic lines, ion lines, and from C_2 Swan bands.

S. Farhat and co-workers estimate temperature dependencies and electron density distribution from these spectral lines [6]. They obtained excitation temperatures assuming Boltzmann equilibrium among the various excited states, as well as relative equilibrium concentrations of ions and atoms. Measurements taken with single catalysts and with the yttrium/nickel mixture indicated that when nickel was the only catalyst present, the inferred temperature was significantly higher, about 10000 K, than when yttrium was present, about 3000 K. As the argon/helium mixture was varied they saw a maximum in the temperature near the centre of the arc for 60% argon. Further work needs to be done to explain this behavior.

H. Lange and co-workers [7] find temperatures within 3500-6500 K and C_2 column densities within $(0.5 - 6) \times 10^{15}\,\mathrm{cm}^{-2}$ depending upon the arc current and plasma coordinates.

Synthesis of Either SWNTs or MWNTs

Two kinds of syntheses can be performed with this method:

Evaporation of Pure Graphite

In this case, two kinds of products are formed in the reactor: a deposit which grows on the end of the cathode during the arc process [3] and soot on the reactor walls. The flocky to crumbly soot contains fullerenes, amorphous carbon, some graphitic sheets but no nanotubes. The deposit consists of a hard grey outer shell and a soft fibrous black core [8]. Various microscopic observations have shown that the outer hard shell is formed of nanoparticles and MWNTs fused together whereas the core contains about one-third polyhedral graphitic nanoparticles and two-thirds MWNTs [9]. The MWNTs consist in a few to a few tens of graphitic sheets which are concentrically rolled up around each other with a constant separation between the layers nearly equal to that of the graphite layer spacing (0.34 nm). Their inner diameter varies between 1 nm up to 3 nm and their outer diameter ranges from 2 nm up to 25 nm depending on the number of concentric layers. Generally their length is not more than 1 μm but some exceeding 1 μm have been observed. The perfectness of the crystallinity of the layers and of their stacking observed in HRTEM (Fig. 2) is striking. Each concentric layer is seen as a set of two

dark lines symmetrically located with respect to the tube axis as explained in Chap. 3. The great majority of the MWNTs have closed tips by insertion of pentagonal defects into the hexagonal network, as also explained in this chapter.

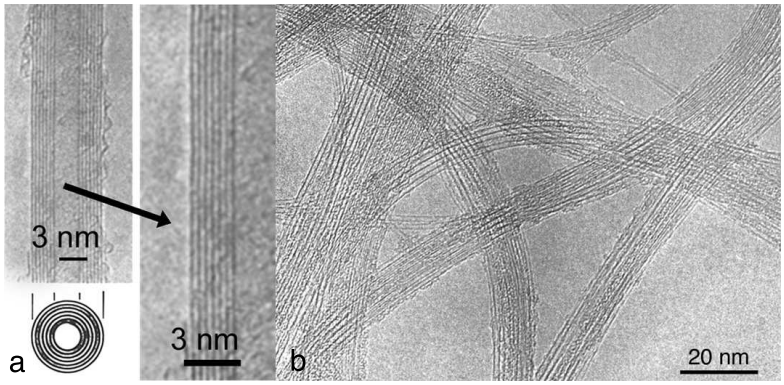

Fig. 2. High resolution transmission microscopy images of nanotubes produced by the electric arc method: (**a**) A multiwall nanotube with a magnification showing details of the layer structure (adapted from [3]) ; (**b**) set of single wall nanotubes assembled into ropes (the synthesis procedure is described in [20])

Co-vaporization of Graphite and Metal

By drilling a hole in the centre of the anode and filling it with a mixture of a metal catalyst and graphite powders, another element is introduced and co-evaporated with the carbon during the arc discharge process. As a consequence the macroscopic and the microscopic structure of the formed products changes [10]. As with pure graphite, a deposit grows at the surface of the cathode (Fig. 3a). This deposit contains MWNTs, empty or filled graphitic nanoparticles, and round spherical metallic particles when obtained with the majority of the tested elements [11]— [25]. Sometimes the MWNTs observed in the deposit are found to be filled [25]— [27]. Under certain conditions, a collaret similar to a soft belt is formed around the hard shell of the deposit [11]— [20]. In this collaret, amorphous carbon, spherical metallic nanoparticles, a few graphitic sheets, and a high density of SWNTs are found (Fig. 3b).

Single wall nanotubes can be isolated or organized in bundles consisting of a few to a few tens of single tubes stuck together in a triangular lattice and more or less covered with fullerene/soot material. Fig. 2b shows an example of bundles observed in HRTEM. Each bundle is imaged as a set of fringes parallel to their axis as explained in Chap. 3. The majority of the tubes have a diameter between 1.2 and 1.4 nm and lengths reaching up to several microns.

However no collaret is formed with some elements [10]– [14], [16]– [18], [21]– [25]. Growing from the cathode to the reactor walls and decorating the chamber are also found some kinds of "spider webs". These structures, containing fullerenes, amorphous carbon, some graphitic sheets, and a low density of SWNTs are obtained when using mixtures of Co or Ni [11]– [20]. In some cases, webs might not appear [10]– [14], [16]– [19], [21]– [25]. The soot can vary from crumbly to spongy in appearance and is formed of the same structures as those found in the webs. Depending on the element co-evaporated, it can contain SWNTs [10]– [20], [23], [28] or short SWNTs radially growing from catalytic particles like "sea urchins" [11], [24], [29] or MWNTs with a good portion of their length filled with metal [13], [14], [22] or no nanotubes at all [11], [13], [17], [19], [21]. The quantity and quality of the nanotubes obtained this way depend mainly on the metal/carbon mixture. A lot of elements and mixtures of elements have been tested by various authors and it is noted that the above-described results can vary significantly from one author to another even though the elements used are the same. This is not surprising since the experimental conditions depend on various parameters such as the metal concentration [10]– [29], the inert-gas pressure, the nature of the gas [30], the current, and the geometry of the system.

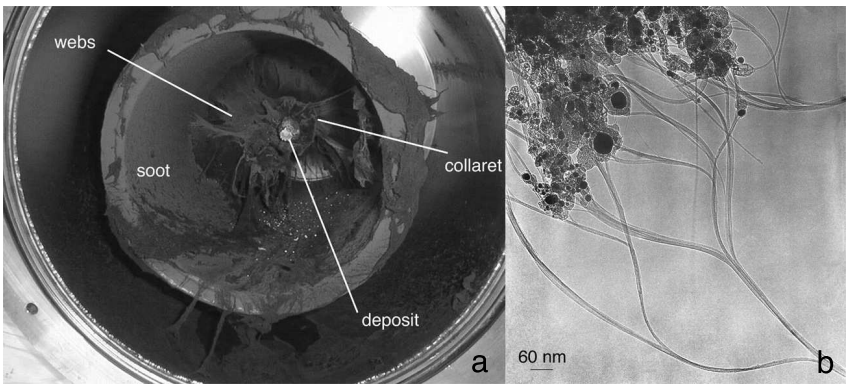

Fig. 3. (**a**) View of the reactor after synthesis where one can distinguish the various products obtained when using a mixture of carbon and catalysts ; (**b**) TEM image of the collaret containing bundles of SWNTs mixed with catalyst metallic particles and different graphitic structures

1.3 Laser Ablation

Historically, pioneer production of fullerenes was obtained with a laser ablation technique [1]. In this process, a quartz tube was heated to about 1200 °C in a furnace. Within the furnace, an argon flow at sub-atmospheric pressure

was maintained. The tube contained a block of graphite compressed. By the use of intense pulsed laser irradiation, the graphite was vaporized and fullerenes were formed in the condensed soot. Later, the same technique was used to produce carbon nanotubes [33].

Principle and Description

The laser ablation technique is rather similar to the arc method as it also consists of sublimating graphite in a reduced atmosphere of rare gases and has been proved to lead to very similar structures to those obtained by the arc method: fullerenes, SWNTs or MWNTs with the same crystalline quality, onions, ...

Ablation of a graphite target with a focused laser beam is realized in an inert atmosphere at low pressure (Fig. 4). Two kinds of methods were developed and they used either a pulsed laser [33, 34] or a continuous laser [35]. The main difference between both lasers is that the pulsed laser demands a much higher light intensity (100 kW/cm^2 compared with 12 W/cm^2). In the pulse laser configuration, a Nd-YAG laser pulse evaporates a solid target of graphite (or graphite and catalyst) into a background gas which is gently flowing through a quartz tube inside a high temperature oven. The laser converts the composite solid material into small aggregates which can only recombine if placed in an external furnace heated to 800°C minimum [36]. The role of the furnace is to create a temperature gradient suitable for the formation and growth of long nanotubes [37]. In the continuous laser configuration a 2 kW continuous wave CO_2 laser is focused on the target, heating it up to 3000–3500 K. The target is placed vertically and an inert gas (He, Ar, N_2) is flowing from the bottom to the top of the reactor chamber. During the vaporization process the flowing argon gas sweeps the produced soot inside the quartz tube. In this case, carbon nanotubes can be formed without the help of an additional furnace. Indeed, in contrast to the pulse laser configuration, the flowing gas is heated in the vicinity of the target up to the temperature reached at the surface illuminated by the laser as shown by Foutel-Richard [38] and Dorval et al. [39].

In both cases, the nanotubes nucleate in the vapour phase, coalesce, get carried away by the flowing argon and condense downstream on the water-cooled copper collector. The felt-like material, when scraped off the wall, contains MWNTs or SWNTs depending on the experimental conditions. As with the electric arc method, MWNTs are obtained when using a pure graphite target and SWNTs when the target is a mixture of graphite and metallic catalysts such as Ni-Co or Ni-Y mixtures [35, 40]. Nanotubes are accompanied by amorphous carbon, metal particles, and onions as in electric arc techniques. Many purification methods have been developed to extract high yield samples of SWNTs and MWNTs.

The main differences with the arc method are:

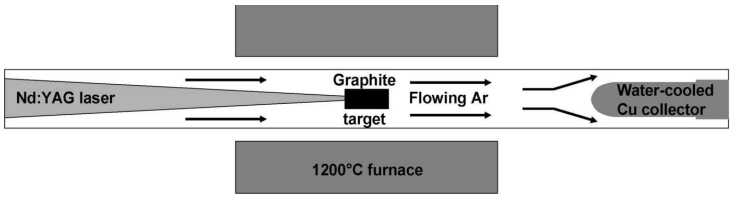

Fig. 4. Principle of the laser ablation technique, after [34]

- The material is submitted to a laser ablation instead of an arc discharge.
- No tube of reasonable length has ever been synthesized without some catalyzing particles. This implies that a certain local anisotropy is necessary to grow a nanotube.
- Particles are collected through a carrier gas on a cool plate far from the target. A secondary heating is usually added.

In situ Diagnoses

Formation and growth mechanisms of carbon nanotubes during the laser ablation process are being more and more frequently investigated [39, 41–44]. In this part, we will distinguish pulsed laser from continuous laser vaporizations.

Pulsed Laser Vaporization

Pulsed laser vaporization with nanosecond lasers is especially amenable to diagnostic investigations. The vaporizing pulse lasts only 10 ns and SWNT growth then can occur undisturbed from further excitation, even for single laser ablation events. D. B. Geohegan's group at ORNL has developed a set of unique diagnostics including spectroscopic gated-ICCD imaging, ion probe measurements and several optical spectroscopic methods to monitor the laser ablation of graphite for the synthesis of nanotubes [41, 42]. Results of these studies are summarized in Fig. 5.

Spectroscopic measurements of the luminous laser plasma are made at early times after Nd:YAG laser ablation ($< 200\mu s$) and after long-pulse CO_2 laser ablation at room temperature. However, these measurements are limited to times while the ablated material is still quite hot. It is found that carbon converts to clusters very early (~ 0.2 ms), at a temperature below 3500°C, the catalyst converts to clusters much later (2 ms) and at a much lower temperature below 1750°C and after 2 ms only carbon nanotubes can be detected. The key finding of these measurements is that the atomic and molecular species appear to feed the formation of clusters within the first 2 ms. The temperature range 1400–1300°C is found to correspond to the onset of nanotube growth. It roughly corresponds to the eutectic temperature of Ni–C and of Co–C systems [45]. The majority of nanotube growth occurs for times > 2 ms and can exceed tens of ms. Therefore, the feedstock for

the majority of nanotube growth is small carbonaceous clusters, or larger aggregates of these clusters (and not atomic or molecular species).

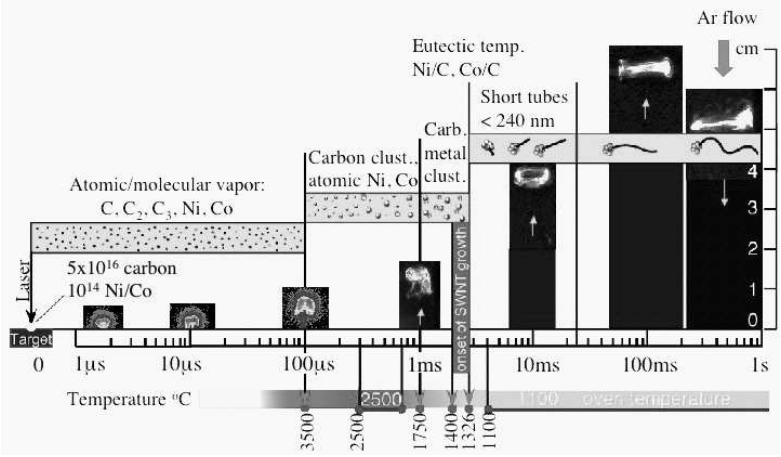

Fig. 5. A compendium of the results from Puretzky et al. [41, 42], which shows actual images of the ablation plume vs. time (log scale), the species detected spectroscopically from the plasma emission or laser-induced luminescence spectra, plume temperatures measured through blackbody emission above the oven temperature, and lengths measured from arrested-growth experiments

These main conclusions regarding plume composition versus time are confirmed by Kokai et al. [46] and Arepalli er al. [43] who used a similar time-resolved imaging and spectroscopy approach based on in situ measurements of laser-induced emission and scattering from the propagating plume.

These results are also confirmed by De Boer et al. [47] who performed in situ, laser-induced fluorescence monitoring of the atomic Ni density in the near-target region and confirm that the majority of Ni atoms also stay in the vapor phase for several milliseconds after ablation.

Finally the necessity of using an external furnace for creating the suitable temperature gradient has been shown by black-body emission spectroscopy measurements [37].

Continuous Laser Vaporization

A dedicated reactor has been developed [38, 40, 48] to investigate the gas phases during carbon nanotube formation by a complete set of optical diagnoses: laser-induced fluorescence (LIF), laser-induced incandescence (LII), coherent anti-Stokes Raman Scattering (CARS), and emission spectroscopy [39]. The temperature gradient above the target has been determined by measuring by CARS the temperature of the flowing gas [39, 40]. Three distinct spatial regions of cooling are derived from a fast cooling above 2000 K in

the first 3 mm above the vaporized target (region 1), a moderate cooling up to 7 mm where the gas temperature reaches 1600 K (region 2), and then a long plateau of temperature at about 1000 K (region 3). LII imaging yields a map of the density of the hot carbonaceous flow and revealed drastic spatial changes due to the presence of catalysts.

These observations are confirmed by gas phase LIF and spontaneous emission of Co, Ni, and C_2. The C_2 radical is well detected as in pulse laser set-up and its existence is found to be restricted to region 1. The transition between regions 1 and 2 at a temperature about 2000 K corresponds to the drop of C_2 concentration in the gas phase. As in pulse laser experiments, metal vapours remain present at much lower temperatures and disappear at the end of region 2 only. Region 2 at temperatures between 2000 and 1600 K is associated with the condensation of metal vapours into liquid metal particles. This condensation influences the process of carbon coalescence because the spatial profiles of C_2 and soot concentrations are markedly different with and without catalysts. Dissolution of carbon in liquid metal particles may explain this key observation. It is therefore suggested that at this location, growth of carbon nanotubes starts.

1.4 Vaporization Induced by a Solar Beam

In 1993, aware of the interest of the solar method, the Smalley [49] and A. Lewandowski [50] teams in the USA and groups from University of Montpellier and the Institute for Material Science and Process Engineering (IMP-CNRS) in Odeillo (France) [51] demonstrated that fullerenes could be produced by sublimation of graphite using highly concentrated sunlight from a solar furnace.

Principle and Description

This method, which can be compared with continuous laser vaporization, uses a solar furnace to focus the sunlight on a graphite sample and vaporize carbon. The soot is then condensed in a cold dark zone of the reactor.

At the solar furnace from Odeillo (France) [51], the sunlight is collected by a flat tracking mirror and is reflected towards a parabolic mirror which focuses the solar radiation directly on the graphite target. The target is placed at the centre of an experimental chamber which is first evacuated and then swept by helium or argon. Under clear sky conditions, temperatures of around 3000 K can be reached at the 2 kW set-up of the solar station and the evaporation process can start. With this reactor, evaporation of graphite is possible and gives a small amount of soot. This soot, which contains fullerenes, is collected in a filter on the water-cooled surface of the chamber. Until 1998, this process was only used to produce fullerenes. However, with an improved setup, the same team [52, 53] demonstrated that they could form nanotubes using

the solar energy. Just by changing the target composition and adjusting the experimental conditions, carbon nanotubes can be produced with exactly the same experimental setup. The target, a graphite crucible, is filled with a mixture of graphite powder and metallic catalysts and placed in a graphite pipe heated at its top by the sunlight (Fig. 6). The evaporated material is drawn

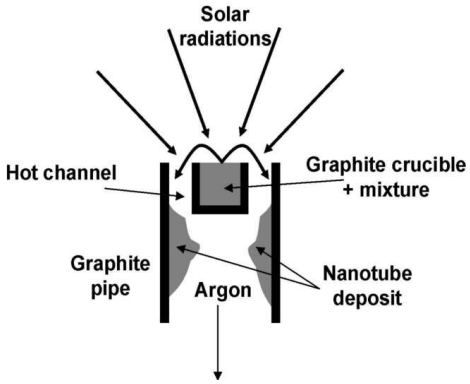

Fig. 6. Principle of the solar furnace technique

immediately through the graphite pipe, which acts as a thermal screen by reducing radiative losses. On its walls the produced soot material is in the form of rubbery sheets which can be collected. Especially nickel / cobalt and nickel / yttrium in the graphite - target mixtures result in the formation of soot containing carbon nanotubes. Depending on the pressure and flow conditions, either bamboo-like MWNTs, or MWNTs and SWNTs together, or only SWNTs in the form of long bundles can be found. Additionally, the nanotubes are accompanied by amorphous carbon and metal nanoparticles. The diameter distribution of the SWNTs lies in the range of 1.2 to 1.5 nm and the sample purity can be as good as that produced by the laser methods. The solar process can lead to production rates of 100 mg per each run (per hour) if the weather conditions allow to keep the temperature during the experiment at 3000 K.

In situ Diagnoses and Simulation of the Synthesis

Diagnostic data have been obtained by pyrometry and emission spectroscopy during the production of carbon nanotubes with a solar reactor [54]. In relation with these measurements, a numerical simulation of the vaporization has also been done. The results point out some common behavior with electric arc or laser ablation, especially concerning the great influence of the cooling rate of vapors on the structure and yield of nanostructured carbon material. The best nanotubes yield is found for a cooling speed of 1000 K/ms, while a

medium yield is obtained at 100 K/ms and no nanotubes at all at 50 K/ms. It is also found that the change of catalyst induces differences in the diameter of SWNT and change of both length and diameter of the bundles. It is finally assumed that the key parameter is the temperature at which the SWNTs are formed. This temperature range can be related to the sublimation temperature of the target and to the eutectic temperature of Ni–C and Co–C systems which is about 1300–1350°C [45].

1.5 Up Scaling

Since their discovery, carbon nanotubes have promised the development of a wide range of applications but commercial development has been constrained by the lack of a reliable large-scale manufacturing process. The availability of carbon nanotubes in commercial quantities, consistent quality and at an accessible price will unlock the potential for a wide range of industrial applications. In this section, we discuss the possibilities of scaling up the three main methods described before.

- The carbon arc discharge method is the most common and perhaps easiest way to produce carbon nanotubes as it is rather simple to undertake. It generally produces large quantities of a mixture of components which requires a purification treatment for separating nanotubes from the soot and the catalytic metals present in the crude product. The nanotubes produced have a very good structural quality. The main limitation of this technique is related to the carbon flow rate which is limited by the electrode erosion. It has been shown that the nanotube yield decreases linearly with electrode diameter increase [31]. Despite this problem, some start-up companies have taken up the challenge of scaling up this technique and they supply bulk quantities of arc-grown carbon nanotubes [32].
- Laser ablation produces a small amount of clean nanotubes and because of their good quality, scientists are trying to scale up this method. However, though promising, the results are not yet as good as for the arc-discharge method. Scaling up is possible, but the technique is rather expensive due to the laser and the large amount of power required. Finally a decisive advantage of these methods lies in their suitability for in situ diagnostics.
- Improvement in the production rate of the solar technique can be envisaged by adapting the experimental set-up to a more powerful 1 MW facility at the Odeillo station. For the production of carbon nanotubes with high purity, the temperature of the carbon vapor must be very high (3100°C). With a 1000 kW furnace, targets 100 times larger than those currently used could be heated to such high temperatures. The prototype of a reactor able to withstand such intense power has been developed at the solar furnace in Odeillo and is currently being tested at a power of 50 kW [55]. It has already provided very promising results.

1.6 Synthesis of Heteroatomic Nanotubes

For the synthesis of heteroatomic nanotubes (mainly BN and BCN), many methods were inspired from carbon: arc discharge, laser ablation, pyrolysis, CVD techniques, etc. But making an equivalent production (thin tubes over the micron scale, ropes, quantity higher that what is needed for electron microscopy observations) remained a challenge until very recent years. In this part, we will discuss about synthesis of BN and BCN nanotubes by arc discharge and laser ablation methods only.

Pure BN MWNT and SWNT

Arc Discharge

The main difficulty for synthesizing boron nitride (BN) nanotubes with an arc discharge lies in the insulating character of h-BN which prevents one from simply replacing graphite electrodes by h-BN ones. Therefore different kinds of electrodes have been successively tried, which should both be electrically conducting and contain B and/or N. The first synthesis of BN multiwall nanotubes was done in an arc discharge using a hollow tungsten electrode filled with h-BN [56]. A route to the successful arc-discharge synthesis of pure BN multiwall and single wall nanotubes was found by A. Loiseau et al. in 1996 [57]. The carbon-free plasma was established between electrodes made in hafnium diboride (HfB_2), which is a metallic compound having a high temperature melting point, in a nitrogen atmosphere. At the same time, Terrones et al. obtained nanotubes and encapsulated polyhedral particles by arcing a mixture of h-BN and of tantalum in a nitrogen atmosphere [58]. Later, Y. Saito and M. Maida used ZrB_2 electrodes instead of HfB_2 [59]. Recently, J. Cumings and A. Zettl claimed they could produce macroscopic amounts of pure BN nanotubes by arc discharge of boron electrodes mixed with nickelin nitrogen [60].

This arc discharge technique, even if realized under different conditions, always leads to the formation of BN-nanotubes in very low yields and made of very few layers including single- and double-layer tubes, as identified by high-resolution transmission-electron microscopy. Electron-energy-loss spectroscopy shows that boron and nitrogen are present in a one-to-one ratio approximately. The most frequently observed terminations are empty and flat, with layers perpendicular to the tube axis, in a square shape as explained in detail in Chap. 3.

Laser Ablation

With laser ablation, the first pure BN multiwall nanotubes were obtained by laser heating of c-BN micro-crystals at high nitrogen pressure (5–15 GPa) [61], and later, by using excimer laser ablation at 1200 °C [62]– [63]. In

2001, Lee et al. succeeded in synthesizing bulk quantities of pure BN SWNTs without using a metal catalyst [64] by heating and decomposing a h-BN target with a CO_2 continuous laser under a nitrogen pressure of one bar. A vast majority of these nanotubes had a zig-zag configuration and were organized in crystalline bundles. The end of the BN SWNTs showed encapsulated boron nanoparticles, suggesting that BN SWNTs grow via a root-based mechanism from the reaction of these boron particles with nitrogen.

B–C–N Nanotubes

B–C–N nanotubes have been synthesized using laser ablation of C/B/N mixed targets [69] and arc discharge experiments with graphite cathodes and different kinds of anodes: B/C inside graphite anode in nitrogen atmosphere [65], BC_4N anode in helium atmosphere [66], BCN anodes [67], and HfB_2 anode in nitrogen atmosphere [68].

These B–C–N nanotubes are all multiwalled. Elemental profiles obtained by spatially resolved electron energy loss spectroscopy (see Chap. 5) reveal a strong phase separation between BN layers and carbon layers along the radial direction. Most of these tubes have a sandwich structure with carbon layers both in the center and at the periphery, separated by a few BN layers [68]. These segregations reflect the tendency to phase separation between graphite and h-BN observed in the B–C–N phase diagram [70].

1.7 Conclusion

In conclusion high temperature methods have been known to produce high quality nanotubes, particularly the single wall variety, and in relatively large quantities. Depending on the experimental conditions, it is possible to selectively grow SWNTs or MWNTs. Thanks to their high structural quality, these nanotubes have been instrumental in many fundamental studies of transport, nano-optics, etc.

2 Catalytic CVD Growth of Filamentous Carbon

Catalytic Chemical Vapour Deposition (CVD) processes make possible the growth of carbon filaments of various sizes and shapes at low temperature ($\leq 1000°C$) from carbon-containing gaseous compounds which decompose catalytically on transition metal particles [71–73]. The word *catalytic* is used here to emphasize the role of metallic particles serving as decomposition sites as well as growth germs. We use *filament* here as a generic name for a large family of elongated structures of diameters less than 100 nm, which obviously includes nanotubes at the top of the structural order scale. Some authors prefer to distinguish filaments from nanotubes, and use *filament* to

describe stacked cone-shaped graphene layers; others use the term *nanofibers* instead of filaments.

Formation of filamentous carbon by catalytic decomposition of gases has been intensively studied for 50 years (soon after the introduction of the TEM) because of its detrimental effect during important industrial chemical processes such as steam reforming [72]. This detail is more than anecdotic: the approach used by specialists of catalysis to study carbon growth is based on thermodynamic and kinetic analysis of CVD, with the goal of determining growth rates as a function of various parameters. Material scientists, on the other hand, have been more interested in filament properties, seeking the best way to tailor the filament structure [73]. Many studies have been based on TEM observations after growth without any details on thermodynamics and reaction kinetics. This difference in the scientific approach is even more pronounced in the CNT community, and only rarely has the thermodynamic and kinetic approach been applied to CNT growth [74–76].

Carbon filaments are in some sense ancestors of Iijima's multiwalled carbon nanotubes and it is obvious that the huge amount of research performed in this field (before and after 1991) is useful to the CNT community. We thus find it appropriate to introduce CVD growth of nanotubes by starting with that of carbon filaments, insisting on the thermodynamics and kinetics of the formation mechanism. The chemical reactions involved in the production of carbon (such as the disproportionation of CO, see 2.1) would be infinitely slow or would produce non-filamentary carbon (by decomposition of hydrocarbons) without small particles of metal like Fe, Co or Ni. These metals are considered as catalysts because they are often recovered without any chemical change after the growth reaction. Nevertheless, it has recently been shown that nanoparticle morphology may change during the growth reaction due to high atomic mobility at the surface or because of a solid-liquid phase transition. For the same reasons it happens that elongated nanoparticles are found trapped and molded inside filament cores during growth. Atomic impurities of metals may also be incorporated in the filament structure during growth. Moreover, metals can be changed into carbides by the gaseous reactants and some authors consider that carbon filaments are the result of carbide decomposition (see 2.1). Others consider that filaments precipitate directly from carbon atoms dissolved in the metal, and it has been suggested that the (low temperature) solid-liquid transition evoked above is induced by carbon dissolution in the metal network. Catalytic growth of carbon is thus not just a surface phenomenon but a definitely more complicated one, and much work remains to be carried out before a complete understanding of the process is achieved. The long-term goal is to produce carbon filaments (and nanotubes) at will, with controlled morphology and therefore with defined properties. To do so, we need to understand the thermodynamics and kinetics of specific CVD reactions and the role of the catalytic particle.

2.1 Thermodynamics of Carbon CVD

CVD growth relies on the capability to provide the atoms needed to form the solid deposit (here carbon filaments) from a gas source that decomposes under the action of temperature. The first important point is thus to examine the thermodynamics of the gas decomposition reaction, i.e., first to determine if the reaction is possible or not at the desired working temperature and then secondly to measure the equilibrium constants, which are compared to those for the formation of graphite. Analysis of deviations from graphite equilibrium gives useful information on the filament growth process [77]. We first describe herein two important reactions that have been thoroughly studied because of their industrial interest: decomposition of hydrocarbons, particularly of methane, and disproportionation of CO.

Decomposition of Hydrocarbons

Except for methane and other light paraffins, hydrocarbons (C_nH_m) have a positive value of the Gibbs function of formation $\Delta_f G^\circ$, i.e., variation of the Gibbs free energy ($G = H - TS$) of the system that occurs during the formation reaction from graphite and hydrogen, at all temperatures under standard-state conditions. Variation of the Gibbs function during the decomposition reaction of hydrocarbons into graphite and hydrogen under standard-state conditions (partial pressures are fixed at 1 bar) is opposite ($\Delta_r G^\circ = -\Delta_f G^\circ$) and the decomposition is therefore thermodynamically possible at all temperatures. $\Delta_f G^\circ$ is a measure of how far the standard-state is from equilibrium according to the following reaction:

$$C_nH_{m(gas)} \Leftrightarrow nC_{graphite} + m/2\ H_2.$$

The relationship between the Gibbs function of reaction at any moment in time ($\Delta_r G$) and the standard-state Gibbs function of reaction ($\Delta_r G^\circ$) is described by the following equation,

$$\Delta_r G = \Delta_r G^\circ + RT \ln Q\ ,$$

where R is the ideal gas constant and Q the reaction quotient at that moment in time. At equilibrium, $\Delta_r G{=}0$ and $Q = K$, the equilibrium constant. Partial pressures of H_2 and of C_nH_m, $P(H_2)$ and $P(C_nH_m)$ (in bars), verify $K{=}P(H_2)^{m/2}/P(C_nH_m)$ and $RT \ln K = -\Delta_r G^\circ = \Delta_f G^\circ(C_nH_m)$. K and $\Delta_f G^\circ(C_nH_m)$ both depend on the temperature.

In the case of acetylene, which is often used in nanotube growth, $\Delta_f G^\circ(C_2H_2) = 225.31 - 0.054\,T$ (kJ mol^{-1}) and so $P(H_2)/P(C_2H_2) = \exp(27098/T - 6.5)$, decreasing when the temperature increases but still as high as 1151 at 2000 K. The decomposition of acetylene is therefore thermodynamically almost total at usual temperatures and is controlled by kinetics. Similar results are found with the other unsaturated hydrocarbons.

By contrast, methane has a negative standard-state Gibbs function of formation below 825 K. Therefore methane does not decompose easily. Using values given in [78], we can calculate, under a total pressure of 1 bar, the equilibrium pressures by solving the system $K = \exp[\Delta_f G^\circ(CH_4)/RT]$, $K = P(H_2)^2/P(CH_4)$ and $P(H_2) + P(CH_4) = 1$ (table 1).

T(K)	600	700	800	900	1000	1100	1200
$\Delta_f G^\circ(CH_4)$ (kJ mol^{-1})	-22.851	-12.596	-2.057	8.685	19.572	30.562	41.624
$P(H_2)_{equilibrium}$ (bar)	0.096	0.286	0.565	0.800	0.920	0.967	0.985

Table 1.

Disproportionation of carbon monoxide ($2CO \rightarrow C + CO_2$)

$\Delta_r G^\circ = \Delta_f G^\circ(CO_2) - 2\Delta_f G^\circ(CO) = -170.7 + 0.1746\,T$ is negative (and therefore the reaction is thermodynamically favourable) for temperatures lower than 978 K. Table 2 gives $P(CO_2)$ at different temperatures under 1 bar of total pressure:

T(K)	600	700	800	900	1000	1100	1200	1300
$P(CO_2)_{equilibrium}$ (bar)	0.9987	0.9846	0.907	0.67	0.305	0.082	0.02	0.006

Table 2.

As in the case of methane decomposition, a mixture containing a lower amount of product than the equilibrium pressure is thermodynamically unstable and may deposit graphite. As seen in 2.1, this reaction is favored by high temperature for methane decomposition whereas the disproportionation of CO is favored by low temperature for which the kinetics are usually slow. CO is often chosen as the carbon source because of the opposite effects of thermodynamics and kinetics.

Thermodynamic Effects of Carbon Polymorphism

The Gibbs function of formation is established from graphite which is the reference state for carbon. When carbon is deposited in a form other than that of graphite, the above-given changes of the Gibbs function must be corrected by the Gibbs function of formation of the form considered and the above-calculated equilibria are modified. For instance, at 900 K, $\Delta_r G^\circ$(diamond) = 5.54 kJ mol^{-1} and the calculated value for $P(CO_2)$ at the equilibrium with CO and diamond is 0.56 bar (under a total pressure of 1 bar) instead of 0.67 bar with CO and graphite.

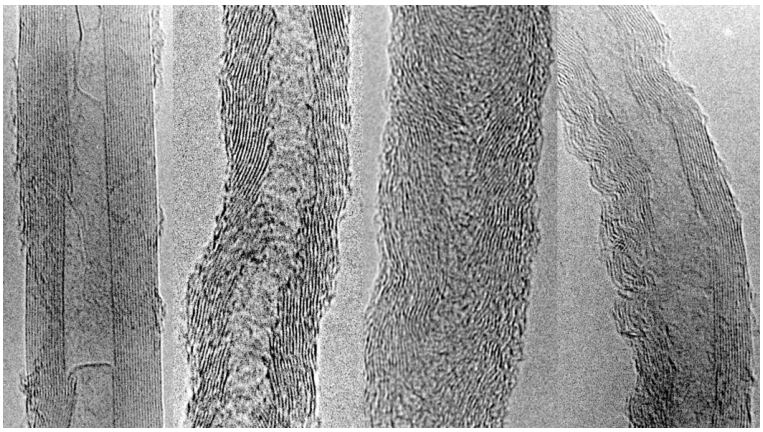

Fig. 7. High-resolution transmission electron micrograph (HRTEM) of various carbon filaments (by courtesy of T. Cacciaguerra)

Though the filamentary form of carbon is closer to graphite than to diamond, its Gibbs function differs from that of graphite. Its value depends on the geometrical arrangement (more or less perfect) of carbon layers and may (slightly) vary from one sample to another (Fig. 7). It can be measured from the composition of gaseous mixtures at the equilibrium with filamentary carbon (or other solid carbon materials). Rostrup-Nielsen [79] obtained in this way Gibbs functions as high as 24 kJ mol^{-1} for nanofibers from CO or CH_4 decomposition over nickel catalysts. He interpreted these results by assuming that "structural disorder" leads to higher surface energies than in graphite, and evidenced a relation between the Gibbs function of the nanofibers and the sizes of the nickel particles located inside the nanofibers. Tibbetts and Alstrup considered the elastic energy effect due to curvature of filament graphite planes as an important contribution to the deviation from graphite equilibrium [77,80]. Tibbetts demonstrated that it was energetically favorable for the fiber to precipitate with graphite basal planes parallel to the exterior planes, arranged around a hollow core, thus forming a wide diameter ($\sim$1 μm) multiwall tube.

Formation of Carbides as a Cause of Deviation from Equilibrium

De Bokx et al. [81] obtained results similar to those reported by Rostrup-Nielsen on deviations from equilibrium calculated from graphite data, but disagreed with the interpretation. Using nickel or iron catalyst for the decomposition of CH_4 or CO in the temperature range 650-1000 K, they evidenced formation of an intermediate carbide phase according to the following equilibrium:

$CH_4 + 3Ni \Leftrightarrow Ni_3C + 2H_2$ or $2CO + 3Ni \Leftrightarrow Ni_3C + CO_2$ (or similar with Fe) followed by $Ni_3C \rightarrow 3Ni + C$ or $Fe_3C \rightarrow 3Fe + C$.

They concluded their work stating that "The process in which filamentous carbon is formed should not be referred to as catalytic. It concerns a heterogeneous reaction with a decomposition product".

2.2 Kinetics and Mechanisms of Filament Growth

The *Dissolution-Extrusion* Mechanism

The kinetics of filamentary growth was extensively studied by Baker et al. [71, 82, 83]. They observed the growth of filaments from acetylene under the controlled atmosphere of a modified transmission electron microscope and measured the growth rate in situ over Ni, Fe, Co and Cr particles. The growth rate was inversely proportional to the diameter of the particles observed at the filament tips, which suggested a diffusion process. They demonstrated that the activation energy of the growth had the same value as the activation energy of carbon diffusion inside the catalyst, which could therefore be the limiting stage in the process. Fig. 8 (where $2CO \rightarrow C + CO_2$ can be replaced by $C_nH_m \rightarrow nC + (m/2)H_2$) pictures the four stages of the "tip-growth" dissolution-extrusion mechanism:

1. diffusion (in the gas phase) of reactive species (CO or C_nH_m) to the catalytic surface
2. gas-solid process: surface adsorption, followed by reaction between adsorbed species (Langmuir-Hinshelwood mechanism) or between an adsorbed species and a gaseous molecule (Eley-Rideal mechanism), both leading to carbon atoms
3. diffusion of carbon atoms through the catalyst particles to excretion sites
4. segregation and bonding of carbon atoms into carbon layers

The same stages are supposed to occur in the "root-growth" dissolution-extrusion mechanism when the particle remains stuck to its support [84, 85]. In experiments of Melechko et al. [86], changing the C_2H_2 partial pressure in a $NH_3 + C_2H_2$ mixture modified the growth mechanism from tip-growth to root-growth. They considered that the initial orientation of growth depended on the relative concentration of carbon at the different locations of the particle, which originated in different rates of carbon formation. Changing the composition of the gaseous mixture could change the order of these rates. Rates of filamentous carbon production from gas phases have been measured and analyzed by many authors in the framework of the dissolution-extrusion mechanism. One important point is to determine what is the driving force for the bulk diffusion of carbon. Baker et al. [83] suggested it was the temperature gradient created by the heat generated by the catalytic reaction, whereas Rostrup-Nielsen and Trim [87] supposed it was a carbon concentration gradient induced by different carbon activities at the filament-metal interface and the area where the decomposition occurs. Audier and coworkers compared carbon deposition rates from $CO–CO_2$ and $CH_4–H_2$ mixtures over FeNi and

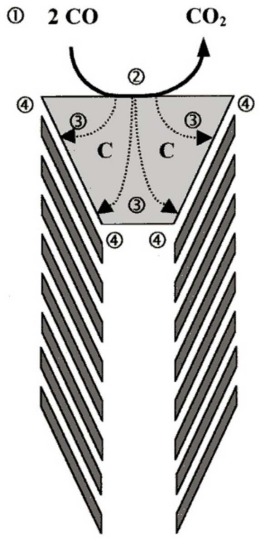

Fig. 8. Schematic illustration of truncated conical filament growth following the dissolution-extrusion model proposed by Baker et al. Stages 1–4 are described in the text.

FeCo alloys [88,89]. For gas mixture compositions not too far from thermodynamic equilibrium, the rate of carbon deposition depended on the deviation from equilibrium irrespective of the nature of the reactant gas (CO or CH_4). This strongly supports the idea that the rate-limiting step is the bulk diffusion of carbon driven by an isothermal gradient with local equilibrium at both metal-carbon and metal-gas interfaces. (A more detailed description is given below in 2.2). Snoeck et al. studied CH_4 cracking over a Ni catalyst and also proposed a growth mechanism in which the diffusion of carbon originates from a concentration gradient; the reasoning is based on thermodynamics arguments on different solubilities of carbon at the metal-carbon and metal gas interfaces [90]. Another approach involved an intermediate carbide layer which can explain both the deviation from graphite equilibrium (see 2.1) and the driving force by a difference of carbon solubilities in the metal and in the surface carbide [77]. Moreover, carbides play a role in kinetics during the activation step (by fragmentation) of massive catalysts [91, 92] and during the deactivation step (by poisoning) [93, 94].

Quantitative Kinetic Study of Carbon Deposition from CO over a Supported Fe-Co Catalyst

Disproportionation of CO on iron-cobalt alloys was thoroughly studied by Audier et al. [88] and more recently by Pinheiro et al. [95, 96]. Binary alloys

were chosen because of their larger stability range vs. carbiding and oxidizing reactions. A kinetic study is thus easier to perform with these catalytic alloys than with pure metals. This example shows that a simple kinetic approach can be applied to a real case and furnish valuable information.

Rates of disproportionation from different $CO+CO_2$ mixtures over aluminosilicate supported FeCo particles were measured around 800 K. Plots against time typically exhibited two regions: a rapid (a few minutes) increase, followed by a slow decrease. The intermediate maximum rates were considered as representative of steady states of the reaction. Following Pinheiro et al. [95] we calculate the kinetic law of carbon growth starting from the assumption that carbon diffusion in the catalytic particle (step 3 in the dissolution-extrusion model) is the limiting step. The disproportionation reaction is then at equilibrium:

$$2CO \Leftrightarrow C(\text{dissolved at the metal-gas interface}) + CO_2$$

According to the Law of Mass Action, $K = P_{CO_2} (P_{CO})^{-2} a_{C,metal-gas}$, with $a_{C,metal-gas}$ the thermodynamical activity of the dissolved carbon at the metal-gas interface, which can be written as γx_{mg} , with γ the activity coefficient in the same conditions and x_{mg} the atomic fraction of dissolved carbon at the metal-gas interface. Supposing carbon extrusion from the catalyst is not limiting (step 4 of the model), carbon that is dissolved near its interface of extrusion can be in equilibrium with filamentary carbon and have the same activity: $a_{C,filamentary} = \gamma x_{mf}$, x_{mf} being the atomic fraction of dissolved carbon at the metal-filament interface.

Diffusion of carbon proceeds through the metal particle owing to the carbon concentration gradient $(x_{mf}\text{-}x_{mg})/V_m$, where V_m is the metal atomic volume. Considering a one-dimensional flow, the diffusion current density is given by Fick's law: $J = -D\, dC_C/dl$ where D is the diffusion coefficient of carbon in the metal and dC_C/dl the concentration gradient.

Thus, $J = -D\ (x_{mf}\text{-}x_{mg})/V_m L = D(LV_m\gamma)^{-1}(K(P_{CO})^2(P_{CO_2})^{-1} - a_{C,filamentary})$ where L is the diffusion length. The rate of carbon deposition is the product of J by the total surface S of the catalyst. Maximal experimental rates are plotted against $K(P_{CO})^2/(P_{CO_2})$ on Figs 9 and 10. Their linear parts can be considered as domains where rates of deposition are limited by diffusion inside the catalyst particles in agreement with the calculation.

The intercept with the $K(P_{CO})^2/(P_{CO_2})$-axis gives $a_{C,filamentary}$ at the considered temperatures, which lead to the Gibbs function of formation $\Delta_f G^\circ = RT \ln a_{C,filamentary}$. Taking into account the uncertainties, the following values (in kJ mol^{-1}) are obtained: $8.5 \leq \Delta_f G^\circ(\text{filaments}) \leq 12.8$ at 470°C and $7.2 \leq \Delta_f G^\circ(\text{filaments}) \leq 11.8$ at 520°C. Note that at higher values of $(P_{CO})^2/(P_{CO_2})$, diffusion in the gaseous phase becomes limiting.

These results are corroborated by a more extensive study of how maximum rates vary with temperature. In the rate law $DS(LV_m\gamma)^{-1}(K(P_{CO})^2 (P_{CO_2})^{-1} - a_{C,filamentary})$, four factors are temperature-dependent: D, γ, K

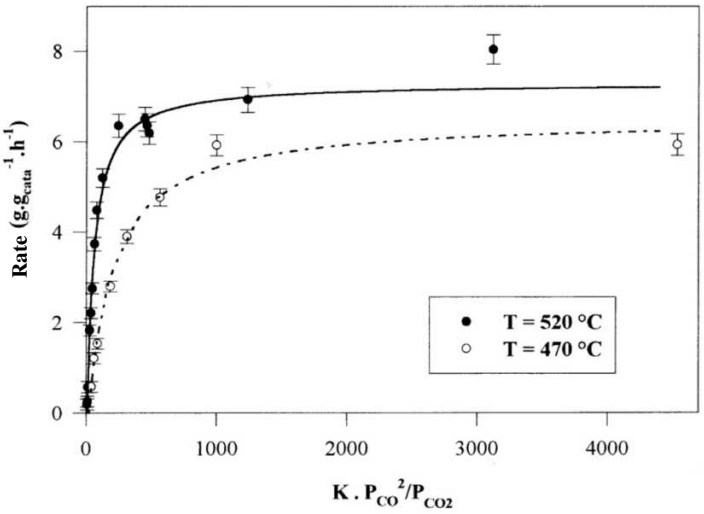

Fig. 9. Maximal rates of deposition vs $(P_{\mathrm{CO}})^2/(P_{\mathrm{CO}_2})$

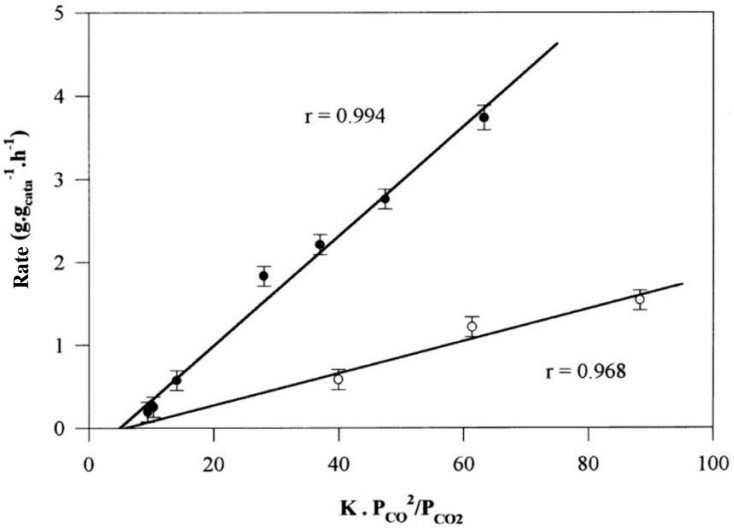

Fig. 10. Enlargement of Fig. 9 for "weak" values of $(P_{\mathrm{CO}})^2/(P_{\mathrm{CO}_2})$

and $a_{\mathrm{C,filamentary}}$. Nevertheless, $a_{\mathrm{C,filamentary}}$ varies slowly with T, γ vs. T can be taken from the literature and the (known) variation of K can be balanced by keeping constant the expression $K(P_{\mathrm{CO}})^2(P_{\mathrm{CO_2}})^{-1}$ (sometimes named carbon activity in the gas phase). Moreover, the constancy with temperature of the two geometric parameters S (active area of the catalyst) and L (length of diffusion), which both depend on the dimensions of the catalyst particles (by fragmentation or coalescence) must be checked. So, the rate varies as the D/γ ratio: D and γ are proportional to $\exp(-E/RT)$ where E is a (constant) energy of activation, therefore the logarithm of the rate should be linear against T^{-1} and the slope gives the activation energy of D/γ. After such a treatment, the measured rates for temperatures from 498 to 548°C look roughly linear (Fig. 11) and the activation energy lies between 168 and 183 kJ mol^{-1} which is consistent with usually observed values.

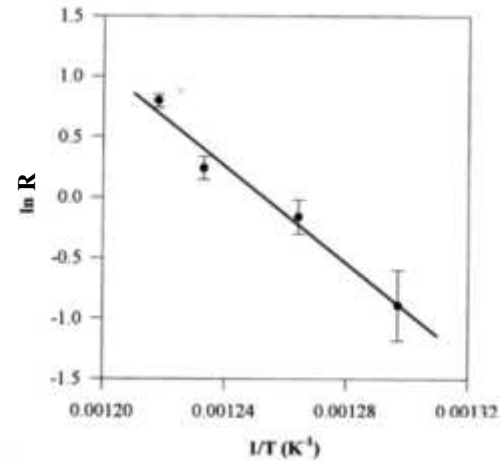

Fig. 11. Logarithm of the maxima rates vs. T^{-1}

2.3 Influence of the Morphology and Physical State of the Catalytic Particle

Catalytically grown filaments exhibit various diameters, shapes and microtexture depending on the microscopic details of the growth process. Since the filament structure greatly influences the properties, it is important to control the growth process and thus to understand why some filaments grow tubular while others are of the cup-stacked-type; why some grow straight while others are helix-shaped [97]. Numerous factors have a potential influence on the process selectivity: the reaction temperature, the reactant composition, the material supporting catalytic particles, and the morphology and physical

state of the catalytic particles. Unfortunately all these parameters cannot be varied independently one by one so that it is difficult to extract a clear phase diagram from the huge number of reported results. We chose here to focus on the catalytic particle and we review a number of studies which aimed at correlating the characteristics of the filament to those of its germ.

Structure of Filaments Grown from Solid Crystalline Particles

Correlation between crystallographic orientation of the carbon and the catalytic metal in filaments was demonstrated by Audier, Coulon, and Oberlin [98,99]. They established by HRTEM that truncated-conical catalyst particles made of different metal alloys were oriented with respect to the filament axis, the orientation being dependent only on the crystallographic system of the alloy and not on its composition. "In the case of all the metal composites prepared from alloys of bcc structure, the metal particle is a single crystal with a [100] axis parallel to the axis of the carbon tube, and the basal faces of the truncated cone, which appear free of carbon, are (100) faces." For fcc FeCo alloys, the [110] axis coincided with the filament axis and the metal-gas interface was (111). It was indeed well known from surface science that the reactivity of catalytic metals depends on crystallographic orientation. For example, graphite epitaxial growth on nickel is more favorable on (111) faces [100]. It was thus tempting to conclude that growth proceeds by dissolution of carbon through some facets and extrusion from others that have a stronger affinity for graphite and so govern the geometric alignment of the platelets in the filaments. This was justified theoretically in the case of Ni particles by extended Hückel molecular orbital calculations [101]. Graphite epitaxy is stronger with the (111) and (311) faces of Ni than with the (100) and (110) faces consistent with geometrical arrangements where some faces are carbon-covered and others are not. Yang and Chen observed that (100) faces are the most abundant at the metal-gas interface for filaments grown on nickel [101]. The role of epitaxy in the nucleation and growth of graphitic filaments by decomposition of 1,3-butadiene on nickel/Al_2O_3 has been analysed in detail by Zaikovskii et al [102]. Depending on the reaction temperature, cup-stacked or tubular filaments were grown according to the different mechanisms and catalyst structures. They confirmed that (111) flat faces offer epitaxial sites for (002) planes of graphite, and suggest that steps of (100) planes of nickel particles can favor formation of nanotubes at high temperature. In the case of filaments grown from Pd particles, no preferred orientation of the Pd planes with respect to graphite (002) was found [103]. Growth can occur without true epitaxy and shape only seems to have an influence on filament morphology. Kiselev et al. [104] observed that in the case of anisotropic multifaceted nickel particles, catalytic activity is not homogeneous and the extrusion velocity vector, a concept introduced by Amelinckx et al. to explain growth of helicolidal tubular filaments [97], is not constant, which induces topological defects in the filament structure. They confirmed

that facets incorporating carbon are (100) and (110). Different facets are found at the metal-carbon interface.

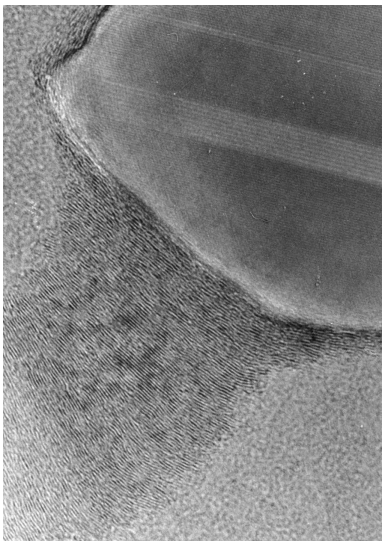

Fig. 12. HRTEM of a nanofibre synthesized from a CO + H_2 mixture over Fe particles

So it follows that filament morphology is governed to a large extent by particle shape and crystallographic structure, and we find in the literature a variety of filament microtextures. Murayama and Maeda reported synthesis of filaments made by the stacking of flat graphene layers arising from facets of the catalytic iron-containing particle (Fig. 12) [105]. Many authors have observed filaments with carbon layers at various inclination angles to the conical particle surface. Rodriguez et al. explained this apparent inclination by a faceting of the lateral surface of conical particles (see Fig. 13) [106]. Since adsorbed gases can modify the shape of supported nanoparticles [107], it may be that variation in the gas composition modifies filament morphology. For example, modification of particle faceting might explain the result of Nolan [108], confirmed by Pinheiro et al. [109], that adding H_2 to CO in the 500-600°C range leads to filaments where carbon layers are inclined to the filament axis (Fig. 13), whereas the absence of H_2 leads to nanotubes.

Growth of Filaments from Liquid Particles

So far we have discussed growth mechanisms supposing the particles were solid since the growth temperature was well below the melting point of the catalytic metal. This assumption is reasonable in the case of big par-

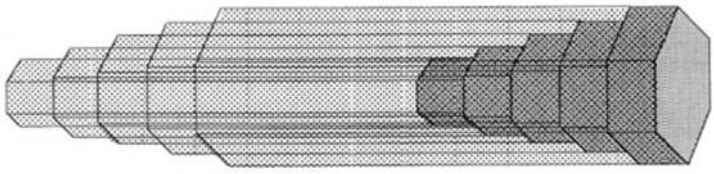

Fig. 13. Particle faceting according to Rodriguez [106]

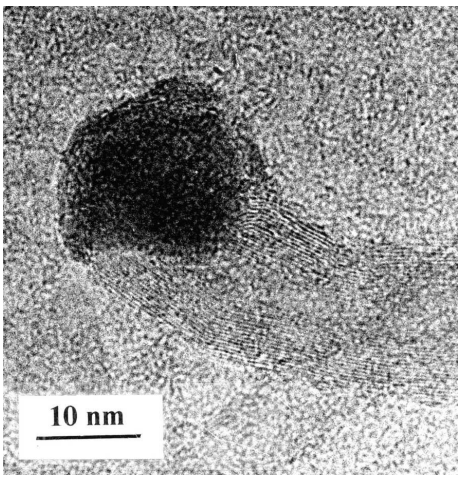

Fig. 14. HRTEM of a MWNT based on CO disproportionation over MgO-supported Co

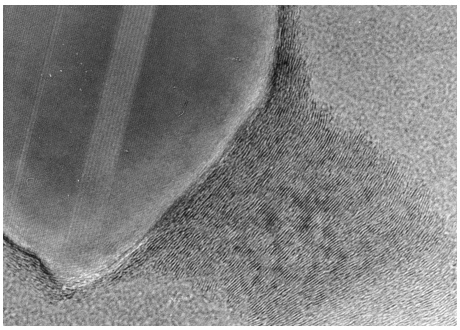

Fig. 15. HRTEM of a nanofibre obtained from a CO + H_2 mixture over MgO-supported Co

ticles ($\geq$10 nm in diameter) but is questionable when dealing with nanometre size germs. Tibbetts and Balogh showed recently that filaments can be grown from melted iron particles when the reaction temperature is above the iron/graphite eutectic [110]. In fact, filament growth from melted particles dates back to the 70s when Koyama discovered that carbon fibres could be grown from benzene between 1150 and 1290°C using hydrogen as a carrier gas [111]. These so-called vapour-grown-carbon-fibres (VGCF) have diameters larger than one micrometre and lengths longer than one millimetre (sometimes several centimetres). Oberlin et al. established that the growth resulted from a two-stage mechanism: catalytic growth of a "precursor" filament first occurs (thinner than 100 nanometres) and then thickening proceeds via the deposition of pyrolytic carbon layers [5]. Melting of the catalyst nanoparticles explains the unusual length of the precursor [110, 112] because it enhances the decomposition of hydrocarbons at the particle surface and/or the diffusion of carbon through or over the melted nanoparticle. In the case of VGCF, the growth temperature is lower than the eutectic temperature in the Fe-C system (1150°C) but surface tension lowers the melting point of small particles [112]. More accurate HRTEM observations [113–115] evidenced later that precursors were MWNT with cylindrical carbon layers (Fig. 16).

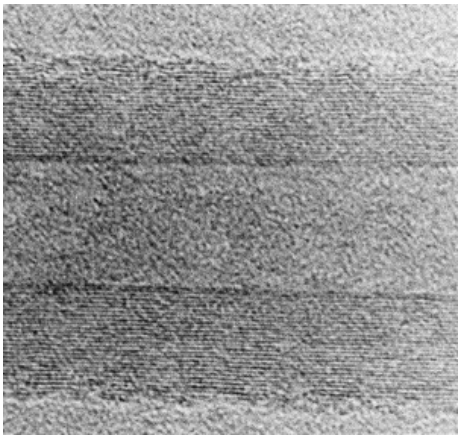

Fig. 16. Nanotubular precursor of a VGCF

The growth mechanism of these precursor nanotubes has been proposed by Baker [82, 85], Oberlin et al. [5] and Tibbetts [80]. The model adopted the concepts of the vapour-liquid-solid (VLS) dissolution-extrusion-like model first introduced by Wagner and Ellis [116, 117] in the sixties to explain the growth of silicon whiskers. In the VLS model, growth occurs by precipitation from a super-saturated catalyticl iquid droplet located at the top of the filament, into which carbon atoms are preferentially absorbed from the vapor phase. From the resulting super-saturated liquid, the solute contin-

uously precipitates, generally in the form of faceted cylinders (VLS-silicon whiskers [116]) or tubular structures [80]. According to Oberlin et al [5], carbon (as individual atoms or not) diffuses over the catalyst surface until it reaches a coalescence site (first, the contact circular line between the particle and its support, then the previously-formed carbon layers).

Melting of the catalytic particle was the ground for interpretation of sequential growth of nanofilaments over FeNi at 1080°C [118]. Li and co-workers studied the influence of pressure on the growth of nanotubes which were produced from acetylene decomposition at 750°C over supposedly liquid Fe particles [119]: whereas cylindrical layers were obtained with a low acetylene pressure (0.6 torr), inclined layers and bamboo-like occlusions occurred at higher pressures, the distance between two occlusions decreasing upon increasing the pressure. Krivoruchko and Zaikovski [120] suggested that iron nanoparticles are liquid at 700°C when oversaturated by carbon and Kukovitsky et al. discussed dissolution-extrusion involving Ni particles in the solid state at 700°C and in the liquid state at 800°C [121]. A voluminous theoretical literature is devoted to this topic, which will be considered again in SWNT growth.

Dynamics and Restructuration of Catalytic Nanoparticles During Growth

Although the importance of the particle state is well recognized, most observations have been done a posteriori so it is difficult to ascertain what really happens during growth. Helveg et al. [122] recently studied the growth of nanofibres in situ using time-resolved high-resolution TEM. They showed that the nanoparticle shape is modified dynamically during the growth, which has important consequences on the nanofibre morphology (see Fig. 17). The authors proposed a growth mechanism involving only surface diffusion. They checked that the core of the particles remained solid and that only surface diffusion modified its shape.

It is interesting to re-examine the morphology of nanocrystals located at the filament root in the light of these new results: the conical particles shown in many cases may well have been formed by stretching during the first layer growth, as suggested recently by X. Chen et al. [123]. Bamboo-structured filaments may also be the result of an extension-retraction mechanism without going through a liquid state. Another recent work on growth of nanofilaments on Pd nanoparticles suggests that a consumption of the catalytic metal occurs during the growth in addition to a modification of the particle shape [124]. Nanoparticles can therefore modify their shape rapidly without going through a solid-liquid phase transition. The carbon growth mechanism depends in fact on the particle dynamics which can be modified by various parameters such as temperature, gas pressure and metal composition. CVD growth using small catalytic nanoparticles is thus a fascinating domain where in situ experiments

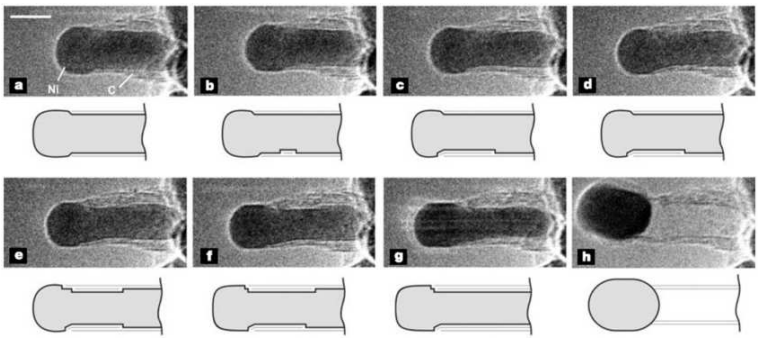

Fig. 17. Image sequence of a growing nanofibre illustrating the Ni particle dynamic behaviour (from Helveg et al. [122])

coupled with thermodynamic and kinetics studies will bring a wealth of new results in the near future.

3 Synthesis of MWNT and SWNT via Medium-Temperature Routes

3.1 From Carbon Nanofibres to Carbon Nanotubes by CCVD

We have seen in the previous section that the catalytic chemical vapour deposition (CCVD) methods are efficient to produce carbon filaments. These filaments, which are not necessarily hollow, even with fishbone-type or bamboo type structure, are often named carbon nanofibres when they have a small diameter ($< 100\,\text{nm}$). But single- or multi-walled carbon nanotubes (SWNT and MWNT respectively) are hollow and made up of one or several concentric graphene layers as described by Iijima [3]. Many works have been conducted first to adapt the CCVD methods to the synthesis of MWNT, and then also to the synthesis of SWNT. Besides the wall structure, the second particularity of CNT among other carbon filaments is their diameter which is much smaller, no more than a few nanometers for SWNT. Considering the previously described formation mechanisms in which each filament is generated from one catalytic particle, located either at the base or at the tip of the filament, the first aim in order to synthesize CNT, particularly SWNT, has been to decrease the size of the catalytic particles. The second aim has been to adjust the conditions of the reaction, often by modifying the value of the physical parameters or the nature of the reacting gas.

The synthesis of nanometer-sized metal particles has been widely studied. But their use as efficient catalytic agents to synthesize CNT supposes to prevent their coalescence during the heating up to the decomposition temperature of carbonaceous gases (600–1100°C). Thus, many ways have been

explored in order to obtain nanometer sized metal particles at these high temperatures. Refractory metals could be used because they are less prone to coalesce than other metals. However, albeit it has been shown that Mo nanoparticles can catalyze the formation of CNT [125], it has been widely evidenced that Co, Fe, Ni nanoparticles, alone or associated with Mo, V or W, are much more active. The formation or deposition of metal nanoparticles on finely divided and/or highly porous powders, which is often used in heterogeneous catalysis, can be efficient but only when the reaction temperature is not too high [126–129]. Another way is to generate the metal nanoparticles in-situ inside the reactor, preferentially at the reacting temperature, either from an organometallic precursor [130–134] or from a solid, by the selective reduction of an oxide solid solution [135–140] or of an oxide compound [141]. The use of moderate temperatures (600–800°C), which suppose to use carbonaceous gases which easily decompose, as CO or certain hydrocarbons, also prevents a too pronounced coalescence of catalytic nanoparticles [142, 143]. A very rapid heating of the catalyst to the reaction temperature can be also an alternative way [127].

Depending on the maximal temperature permitted to avoid or limit the coalescence of the catalytic particles, the carbonaceous gas can be either CO or hydrocarbons (CH_4, C_2H_2, C_2H_4, C_6H_6, ...). Generally, the carbonaceous gas is mixed with an inert gas (Ar, He or N_2) or with H_2 that allows to act on the hydrodynamic parameters or/and to modify the thermodynamic conditions. The reaction temperature must be adjusted to assure thermodynamic conditions favourable to the decomposition of the carbonaceous gas, i.e., for instance, not too high for CO and not too low for CH_4, but also to avoid the deposition of pyrolytic carbon on the CNT. However, it will be shown that, if MWNT are easily synthesized at rather low temperatures (600–800°C), a higher temperature (1000–1100°C) is generally preferred to synthesize SWNT. Often, it is useful to operate at the atmospheric pressure but, in some cases, lower or higher pressures have been proved to be determining [132, 144]. The gas flow must also be adjusted as a function of the quantity of catalyst, taking into account the reaction yield and the necessity to supply each catalytic particle with carbon. Most often, the reaction is conducted with a horizontal tubular furnace fitted with a silica glass tube supplied by a controlled flow of the gas mixture. Either the catalyst material is put as a bed on a plate in the middle of the reactor or is generated in-situ from an organometallic precursor. In this later case, another furnace, operating at low temperature, can be used to sublimate or vaporize the organic precursor. The furnace and the reactor can be vertical, when the catalyst is introduced in the form of a spray or when a fluidized bed of a catalyst powder is used.

Thus, a lot of strategies have been used to adapt the CCVD methods to the synthesis of CNT. All the parameters, related either to the catalyst or to the reaction conditions, are important and may interact. So, each method

must be considered as a whole and, for a given type of CNT (SWNT, small or large diameter MWNT), their efficiency can be evaluated as a function of the quantity and quality of the products. However, depending on the works, the characterization of the produced CNT may be minimal with only a few TEM or SEM images, sometimes without any elementary analysis of carbon or of the catalytic element(s), or can include several methods as, for instance, high resolution transmission electron microscopy (HRTEM), Raman spectroscopy, evaluation of reactivity by thermogravimetry analysis or temperature programmed oxidation, or specific surface area measurements. In the following sections, we will briefly describe a selection of synthesis works representative of the large variety of methods used for the different types of CNT. The particular cases of local grow and template synthesis of CNT will also be presented.

3.2 Synthesis of Carbon Multi-Walled Nanotubes (MWNT) by CCVD

Synthesis of MWNT Using Supported Catalysts

Previously to the report by Iijima [3] of the structure of MWNT, several authors [5, 82, 145] described the CCVD synthesis of carbon filaments, some of which, being not larger than a few tens of nanometers in diameter, probably were MWNT. But after Iijima's paper [3], Yacaman et al. [146] were the first, in 1993, to report the catalytic growth of the so-called carbon microtubules with fullerene structure, by decomposition at 700°C of C_2H_2 diluted in N_2 on graphite-supported Fe particles. The sample contains many other forms of carbon such as bamboo-shaped nanofibres, nanocapsules or nanoparticules, showing the poor selectivity of the method.

Later on, keeping C_2H_2-N_2 mixtures as the reacting gas, B. Nagy and his team, at Namur, has worked to optimize the preparation of metal nanoparticules on porous oxide supports [142,147,148]. Impregnation or ion-exchange or sol-gel methods routes, using metal salt solutions and silica gels, zeolites, alumina or alumina-silica as substrates, are followed by air calcination and sometimes pre-reduction in H_2/N_2 at 500°C and then treatment at 600-700°C in C_2H_2/N_2. The quantity and the characteristics of MWNT depend on catalytic materials and reaction parameters. In some cases, some filaments are helical or covered by disordered carbon. They showed that Fe, Co or Fe-Co alloys are better than Ni or Cu and that a lower temperature favours a lowering of the quantity of disordered carbon deposit but also a lower crystallinity of the CNT [142]. With Co on zeolite, bundles of SWNT were obtained besides MWNT [147]. A better selectivity was obtained using a sol-gel preparation or alumina-silica substrates [148]. Chen et al. [149, 150] obtained MWNT (Fig. 18) by generating the metal nanoparticles in-situ by the selective reduction of $Mg_{0.6}Ni_{0.4}O$. Using CO/He, MWNT with a cylindrical structure were formed from Ni particles whereas CH_4/He produces

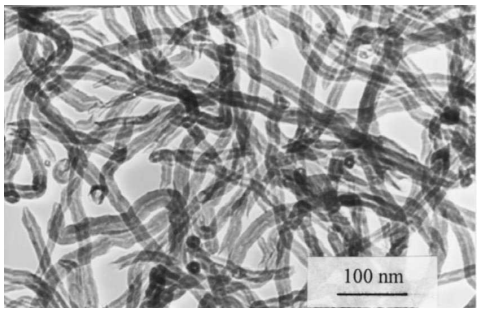

Fig. 18. Typical low resolution TEM image of MWNT synthesized by CCVD over supported catalysts [149]. Reproduced from P. Chen, X. Wu, J. Lin, H. Li, and K. L. Tan: Carbon **38**, 139 (2000), copyright 2000 with permission from Elsevier

carbon nanofibres with a conical structure. This method and the one using $Mg_{1-x}Co_{:mathrmx}O$ solid solutions [137] were adapted by Soneda et al. and Delpeux et al. [151,152]. With Co, C_2H_2 as hydrocarbon instead of CH_4 and a low temperature (600°C), 10-15 walls MWNT were obtained in great quantity (400 mass. % of the catalyst material). As reported by Flahaut et al. [137], the MgO substrate is then easily removed by dissolution in hydrochloric acid. Sun et al. [144] prepared 40 nm diameter Co-Ni particles by ionic exchange on zeolites, air calcination (500°C) and reduction (H_2/N_2, 500°C). The reaction (820°C) with C_2H_2/N_2 at a pressure of only 160 Torr led to very straight MWNT. Ning et al. [141] prepared a Mo rich (50 wt.%) Co-Mo-Mg oxide catalyst based on the very well crystallized $MgMo_2O_7$ compound. Very large quantities of bundles of MWNT (1500 mass. % of the catalyst material), about 10 nm in diameter, were obtained by decomposition of CH_4 on this catalyst, showing the great influence of Mo.

Synthesis of MWNT Using Catalytic Particles Formed in-situ from an Organometallic Precursor

With ferrocene vapour as Fe source and a CH_4/H_2 gas mixture (80 kPa, 900-1100°C), Qin et al. [153] obtained quite well graphitized MWNT embedded in disordered carbon. Using a two stage furnace (200°C, 900°C), Sen et al. [154] showed that if metallocene vapours (Fe, Co, Ni) carried by Ar/H_2 produce a mixture of MWNT and onion-like structures, the addition of C_6H_6 lead to high yields of MWNT whose thickness depends on the metallocene content. At higher temperatures (400°C, 1100°C), with a high gas flow (1000 sccm Ar or Ar/C_2H_2), large or very large quantities of bundles of aligned MWNT are synthesized [155]. The alignment of the NTC and the compacity of the bundle increases with the C_2H_2 flow.

Synthesis of MWNT Aligned in Bundles

By spin coating of a Fe nitrate solution on Al or SiO_2 substrate and heating up to 650–750°C under vacuum, Emmeneger et al. [156] obtained Fe clusters whose average diameter and density is controlled by the nitrate solution concentration and the temperature. The decomposition of C_2H_2 highly diluted in N_2 (2/98) at 0.5 bar and 630-750°C led to well aligned MWNT (10-15 µm length - Fig. 19). The cluster diameter and density determined the diameter and density of the MWNT. Terrones et al. [157] prepared laser-etched thin films of cobalt on SiO_2 on which well aligned MWNT (30-80 walls) were synthesized by pyrolysis of 2-amino-4.6-dichloro-s-triazine under Ar flow at 950°C. The growth of CNT, perpendicularly to the substrate surface, occurred only in the etched areas, catalyzed by cobalt particles (< 50 nm) which condensed and crystallized in these areas. Wei et al. [158] showed that pillars of densely packed MWNT grow on Ni thin films deposited on Si/SiO_2 substrates when exposed to a prevaporised xylene/ferrocene mixture carried by Ar. The authors proposed that the catalytically active species are Fe particles preferentially deposited on circular microcracks of the Ni films.

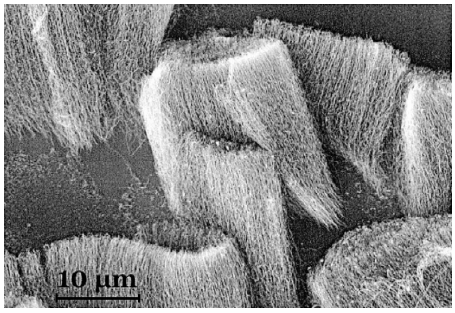

Fig. 19. SEM image of well-aligned CNT synthesized by thermal CCVD over Fe clusters supported on an aluminium substrate [156]. Reproduced from C. Emmenegger, P. Mauron, A. Zuttel, C. Nutzenadel, A. Schneuwly, R. Gallay, and L. Schlapbach: Appl. Surf. Sci. **162-163**, 452 (2000)

Localized Synthesis of Oriented MWNT

Many authors have developed methods to locally synthesize carbon filaments, densely packed on large areas and vertically aligned on Si/SiO_2 substrates, especially for application to field emission displays. Although the authors generally call these filaments nanotubes, it seems that they often are bamboo-shaped filaments. a et al. [159–161] prepared Ni, Co or Fe particles by etching a metal thin film with a dilute HF solution, followed by a thermal treatment in

NH_3 at 850-900°C. Vertically-aligned bamboo-shaped carbon filaments (80-120 nm in diameter, about 20 µm in length) were obtained by thermal CCVD of C_2H_2 at the same temperature. The filament diameter and growth rate were controlled by the parameters (flow and dwell time) of both NH_3 and C_2H_2 treatments. Ago et al. [162] synthesized Co particles (average diameter 4 nm) by a reverse micelle method. After a pretreatment in $H_2S/H_2/N_2$ at 400°C in order to activate and sulfurize Co nanoparticles, vertical filaments which seem to be true MWNT with a cylindrical structure were grown at 800-900°C in C_2H_2/N_2. Such oriented and well crystallized MWNT were also synthesized by Andrews et al. [163, 164] at 675°C using vapours issue from a ferrocene/xylene mixture carried by an Ar/H_2 flow.

Plasma enhanced CCVD methods (PE-CCVD), with sometimes the assistance of a hot filament or microwave have also been studied, mainly in order to improve the alignment and orientation of the carbon filaments. Ren et al. [165] used as catalyst a Ni thin film (16-60 nm) etched by an NH_3 plasma which was then exposed to a C_2H_2/ NH_3 plasma (1-10 Torr) in the presence of a hot filament, the temperature of samples being estimated at 666°C. The MWNT were very well aligned perpendicularly to the substrate when their density (quantity for a given surface area of substrate) is sufficient. Moreover, larger is the diameter of the MWNT, higher are their rigidity and their alignment (Fig. 20). Ho et al. and Wang et al. [166–168] generated Fe, Co or Ni particles by etching continuous or micro-patterned thin films (5-100 nm) with an H_2 plasma, which appears much more efficient than H_2 gas. The PE-CCVD was performed with C_2H_2/H_2 plasma (1-1.2 Torr, radio-frequency power of 100 W). The alignment of carbon filaments, which seem to be true MWNT [ta7], is more or less pronounced, depending on their density on the substrate. Cui et al. [169] used a PE-CCVD system assisted by microwave, firstly at 660-1000°C with a NH_3 plasma to etch a Fe thin film (10 nm) to obtained 100-200 nm particles, and then with a CH_4/NH_3 plasma to depose well aligned bamboo-shaped carbon filaments. The characteristics of the deposit depend essentially on the etching temperature and on the CH_4/NH_3 ratio.

Conclusions

Many CCVD methods have been developed to prepare MWNT and most of them use Fe, Co or alloy nanoparticles as catalyst, only a few using Ni nanoparticles which seem to be less active. Among the different forms of the catalytic materials, the use of nanoparticles supported on powders is probably more selective and this can be optimized by varying the nature, the specific surface area and the porosity of the substrate. After the CNT synthesis, the elimination of the substrate without damage to the CNT can be a problem and thus, substances such as MgO which are easily dissolved by non-oxidative acids are preferable. The generation of catalytic particles insitu in the reactor from vapours of organometallic precursors seems to be less

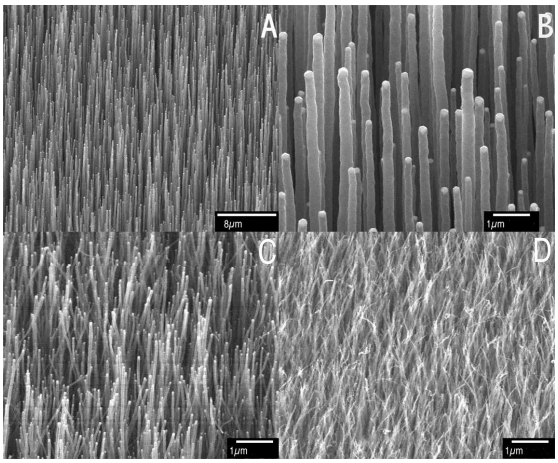

Fig. 20. SEM images of large arrays of well-aligned CNT synthesized by plasma-enhanced hot filament CCVD ; (**A, B**) large diameter (250 nm) CNT which are very rigid and very well aligned ; (**C-D**) thinner CNT (65 and 20 nm in diameter, respectively) showing that the alignment of CNT gradually decreases with their diameter reproduced [165]. Reproduced from Z. F. Ren, Z. P. Huang, J. W. Xu, J. H. Wang, P. Bush, M. P. Siegel, and P. N. Provencio: Science (Washington, D. C.) **282**, 1105 (1998), copyright American Society for the Advancement of Science

selective, but presents the advantage to avoid the step of the substrate elimination and is also easier to be adapted for a continuous production. Many gases may be used for the carbon supply, particularly C_2H_2 or CO which decompose at low temperatures. However, a better crystallinity of the MWNT is obtained when higher synthesis temperatures are used. The characteristics of the MWNT are more or less adjustable by the process parameters but the control of the MWNT diameter is clearly related to that of the nanoparticle diameter. The nature and the proportion of other forms of carbon, which are considered as impurities, are directly a function of the couple (nature of the carbonaceous gas - reactor temperature). The alignment of MWNT into bundles, more ore less packed, is easily obtained when great quantities are deposed on a limited area of substrate. For application to field emission displays, carbon filaments, densely packed on large areas and vertically aligned on Si/SiO_2 substrates can be synthesized either by thermal CCVD or by plasma assisted CCVD (without or with hot filament or microwave). Plasma treatments of metal thin films are very efficient to obtain metal particles. The nature of the carbon filaments (MWNT or bamboo-shaped filaments), their dimensional characteristics and density on the substrate are adjustable both by the characteristics and density of the metal particles and also by the carbon deposition parameters. The alignment of the filaments perpendicularly to the substrate clearly increases with their density on the substrate and with their diameter.

3.3 Synthesis of Carbon Single-Walled Nanotubes (SWNT) by CCVD

Methods Using Catalytic Particles Formed in-situ from an Organometallic Precursor

The CCVD synthesis of SWNT using an organometallic precursor for the catalytic nanoparticles requires the modification of the parameters used for the synthesis of MWNT. Satishkumar et al. [133] used the same reactor and same parameters than Rao et al. [155] except for a lower temperature in the first furnace (350°C instead 400°C) in which the metallocene (or the mixture of metallocenes) are sublimated, probably in order to lower the metallocene vapour partial pressure in the C_2H_2(5 vol.%)/Ar flow, and thus to reduce the size of the metal nanoparticles generated in the second furnace, at 1100°C. They also used vapours of $Fe(CO)_5$ carried by C_2H_2 and then mixed with Ar. SWNT (1-1.5 nm in diameter) were obtained, most of them being covered by disordered carbon. The SWNT quantity is higher with Fe or Co as catalyst and they seem cleaner with a Fe/Co mixture. Ci et al. [131] used ferrocene sublimated at very low temperature and carried by Ar mixed with very few C_2H_2 (< 1 vol.%). The obtained SWNT (0.3-1.8 nm in diameter) are individual or in small diameter bundles, cleaner than the previous ones [133] but the samples contain a lot of carbon capsules formed around Fe particles. Cheng et al. [130,170] used ferrocene vapours carried by a flow of H_2/C_6H_6 in which some thiophene vapours were also added. The obtained samples consists in long and wide ropes or ribbons formed of bundles of SWNT (1-3 nm in diameter), representing about 60 wt.% of the whole sample, about 10–12 wt.% of Fe and some disordered carbon deposits. It appears that the sulphur supply notably increases the proportion of SWNT. Wei et al. and Zhu et al. [134, 171] used a vertical reactor (1200°C, 1 atm) at the top of which a solution of n-hexane, ferrocene and thiophene carried by H_2 is introduced. Very long strands (> 10 cm) of well-organised bundles of SWNT were produced. Nikolaev et al. [132] developed the so-called "HiPCO" method, which is continuous and consists in the supply of two flows, a cold $Fe(CO)_5$/CO mixture flow and a pre-heated CO flow, giving 2-10 ppm of $Fe(CO)_5$ in the final flow. The influence of both the reactor temperature (800-1200°C) and pressure (1-10 atm) on the yield and characteristics of SWNT showed that the higher yield (44 wt.% of SWNT) and lowest diameters with a narrowest diameter distribution (0.6-1.3 nm) were obtained with the highest temperature and pressure (1200°C, 10 atm). Most SWNT are in bundles, regularly covered by many nanoparticles (Fig. 21), which are removed by combining gas and acid oxidations [172, 173].

Methods Using Supported Catalytic Nanoparticles

Supported metal nanoparticles can be generated in-situ, at a high temperature, by the selective reduction of an oxide solid solution [174]. When

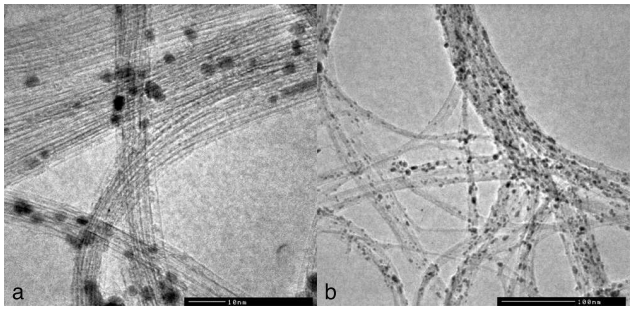

Fig. 21. High (**a**) and low (**b**) magnification TEM images of products obtained by the "HiPCO" method showing that the SWNT are free of disordered carbon and decorated with catalytic Fe nanoparticles [132]. Reproduced from P. Nikolaev, M. J. Bronikowski, R. K. Bradley, F. Rohmund, D. T. Colbert, K. A. Smith and R. E. Smalley, Chem. Phys. Lett. **313**, 91 (1999)), copyright 1999 with permission from Elsevier

the reducing gas mixture contains a hydrocarbon, CNT are simultaneously synthesized owing to the high catalytic activity of the metal nanoparticules (0.5-5 nm in diameter) which are located at the oxide grain surface [139, 140, 175, 176]. Indeed, these native metal particles are small enough to immediately catalyze the formation of SWNT. The first work on this method was reported in 97 by Peigney et al. [140] who used a CH_4/H_2 gas mixture to reduce $Al_{2(1-x)}Fe_{2x}O_3$ powders at 1070°C. The optimization of the characteristics of the solid solution and the parameters of the reaction was conducted by Laurent et al. [139] and Peigney et al. [175,176] using both macroscopic parameters and a microscopic characterization. The obtained CNT are mainly SWNT and double-walled nanotubes (DWNT), individual or gathered in small-diameter bundles (Fig. 22), without carbon nanofibres nor disordered carbon, the undesirable carbon form being essentially capsules surrounding Fe_3C particles. This method was then extended using $Mg_{1-x}M_xAl_2O_4$ (M = Fe, Co, Ni) powders as starting material, showing that, in this system, Co is the most efficient and mainly catalyze the formation of SWNT [138]. The quantity of CNT was increased by using CoFe instead of Co [136] or a ceramic foam instead of a bed of oxide powder [177]. Flahaut et al. [137] and Bacsa et al. [135] showed that the use of a $Mg_{1-x}Co_xO$ powder ($x \leq 0.1$) gives SWNT and DWNT which can be easily separated by the dissolution of MgO in a non-oxidative acid solution such as 1 mol.L^{-1} HCl, which does not damage the CNT. The obtained samples present a very high specific surface area (> 800 m^2/g) because the CNT are mainly individual [135,178]. An improvement of this method was reported in 2001 by Tang et al. [179] using a MgO-based powder with a higher specific surface area in which both Co and Mo elements are added during the oxide synthesis. The optimum Co/Mo ratio was determined to be 2/1 which corresponds to the minimum of the

D/G Raman bands ratio. In this case, CNT are supposed to be essentially SWNT, mainly gathered in bundles, and the reaction yield, calculated from the total weight of catalytic material, is 114 wt.%, much higher than without Mo addition (only 11 wt.%).

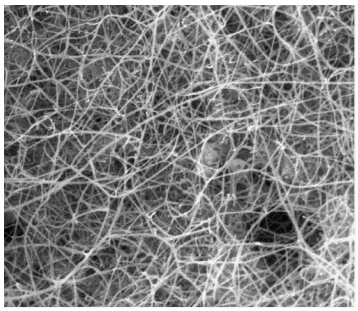

Fig. 22. SEM image of CNT (SWNT and DWNT), individual or gathered in small diameter bundles, upon the MgO substrate, synthesized by decomposition of CH_4 over Co nanoparticles which are generated in-situ by the selective reduction of a $Mg_{0.95}Co_{0.05}O$ oxide solid solution [135, 137]. CNT can be easily separated by the dissolution of MgO in a non-oxidative acidic solution which does not damage the CNT

Another way to obtain supported nanosized metal particles is to impregnate a substrate with one or several metallic salt solutions, to conduct a heat treatment in an oxidative atmosphere which gives pre-formed supported oxide particles and then to reduce them in-situ in the reactor under the action, at high temperature, of the carbonaceous gas and sometimes H_2. This method can be efficient to preserve the nanometric size of the particles because they are less prone to coalesce under heating in the oxide form than in the metal form. The very first synthesis of SWNT by a CCVD method was reported by Dai et al. [125], using Mo particles supported on a highly divided Al_2O_3 powder and pure CO at 1200°C. Small quantities of individual SWNT (1-5 nm in diameter) were obtained. Hafner et al. [128] used Fe/Mo (9/1) on a Al_2O_3 powder and, at 700-850°C, either CO or C_2H_4 and obtained much higher quantities of CNT than with Mo alone. The CNT are a mixture of SWNT and DWNT, the proportion of the latter being larger (70%) with C_2H_4, for 850°C. The main undesirable carbon form being capsules surrounding catalytic particles, the author conducted energetic calculations showing that a CNT is more stable than a capsule for a diameter not larger than 3 nm. Cassell et al. [126] also used Fe, FeMo or FeRu on a mixed substrate (δ, γ-)Al_2O_3-SiO_2 and CH_4 at 900°C. They reported a spacing effect of SiO_2 and an increase of the proportion of SWNT in the sample with Mo which they interpreted as a an aromatisation effect of the hydrocarbon. Colomer et al. [127] using Fe, Co, Ni or binary systems on Al_2O_3 or SiO_2 and C_2H_4/N_2 at 1080°C

showed that the Al_2O_3 substrate and Co or Fe (or mixed) are to be preferred. They obtained SWNT either essentially individual (1.6–6 nm in diameter) or in bundles (NTC diameter of 0.7 nm). Possibly, in the latter case, the SWNT which compose one bundle grew together radially from a large catalytic particle. Harutyunyan et al. [129], using Fe or Fe/Mo on Al_2O_3 and CH_4/Ar at 680-900°C, compared the efficiency of the catalytic materials without and with a pre-reduction treatment. They showed that the pre-reduction treatment (H_2/He, 500°C, 10-20h) allows to obtain almost as much SWNT at only 680°C as obtained with non pre-reduced materials at 900°C. Maruyama et al. [180] reported a low cost method using C_2H_5OH vapours at 600–900°C and a low pressure (5 Torr), with Fe/Co on a zeolite substrate. The authors claimed that they obtained very pure SWNT (Fig. 23), the high quality being a consequence of the etching effect of OH radicals attacking carbon atoms with a dangling bond. For optimized temperatures, the Raman spectra show well-defined RBM bands and very low D/G band ratios (Fig. 24) which confirm the high quality of the SWNT. Some authors reduced the pre-formed

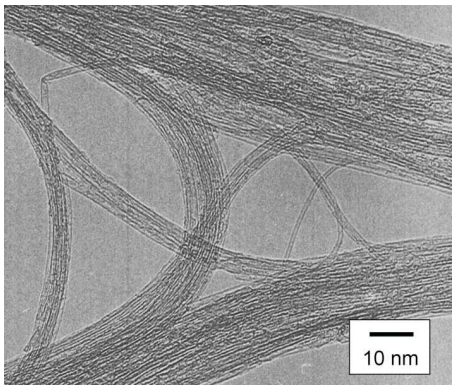

Fig. 23. TEM image of "as grown" SWNT synthesized by decomposition of ethanol over Fe/Co mixtures embedded in zeolite at 800°C [180]. Reproduced from S. Maruyama, R. Kojima, Y. Miyauchi, S. Chiashi, and M. Kohno: Chemical Physics Letters **360**, 229 (2002), copyright 2002 with permission from Elsevier

supported particles before the introduction of the catalytic material in the CNT synthesis reactor. Kitiyanan et al. [143, 181] prepared a catalytic material by impregnation of a SiO_2 substrate with Co and Mo salt solutions, calcination in air at 500°C which allows the crystallisation of the $CoMoO_4$ compound and pre-reduction in H_2 at 500°C. The CNT synthesis reaction was then performed at 700°C in a CO/He (1/1) gas mixture. The products contain essentially SWNT ($d \simeq 1$ nm) with only little disordered carbon and without MWNT, showing that the association of Co and Mo with an optimized ratio (1/2) gives a high selectivity. The influence of Mo was studied

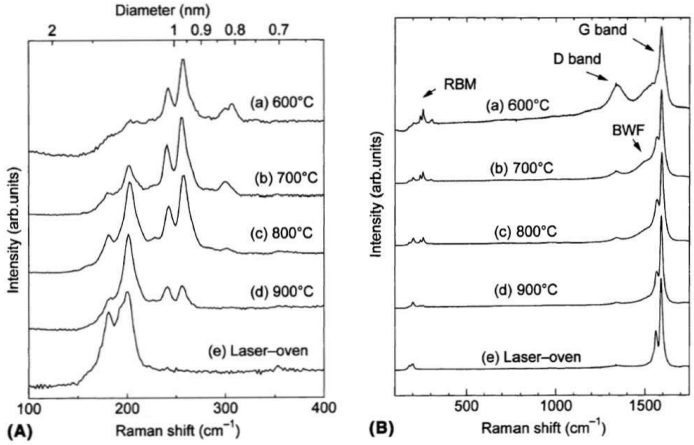

Fig. 24. Raman spectra ($\lambda = 488\,\text{nm}$) of"'as grown" SWNT synthesized by decomposition of ethanol over Fe/Co mixtures embedded in zeolite at various temperatures. (**A**) low frequency range showing well defined RBM bands; (**B**) large range spectra showing the very low D/B band ratios [180]. Reproduced from S. Maruyama, R. Kojima, Y. Miyauchi, S. Chiashi, and M. Kohno: Chemical Physics Letters **360**, 229 (2002), copyright 2002 with permission from Elsevier

by Herrera et al. [182] who claimed that the pre-reduction treatment only reduce the Co-based compounds which does not interacts with Mo but do not reduce Co molybdate like species, these being reduced in-situ in the reactor, leading to metallic Co and Mo carbide. An interesting work on the influence of the diameter of the catalytic particles on the characteristics of CNT was conducted by Cheung et al. [183]. Three classes of Fe nanoparticules, supported on oxidized Si, with narrow diameter distributions centered respectively around 3, 9 and 13 nm were prepared by thermal decomposition of $Fe(CO)_5$. By the treatment of these catalysts in C_2H_4 or CH_4 at 800-1000°C, CNT were obtained with about the same diameter than the initial catalytic clusters. However, 3 nm clusters produced a mixture of SWNT and DWNT and larger diameter clusters produced SWNTS with a lot of DWNT and MWNT (9 nm clusters) and only MWNT (13 nm clusters). These results show that the CNT diameter can be tailored by the size of catalytic particle but also confirm that sufficiently small catalytic particles ($< 3\,\text{nm}$) must be preferred to synthesize SWNT by CCVD methods.

Synthesis of Carbon Double-Walled Nanotubes (DWNT)

The synthesis of double-walled nanotubes (DWNT) has been researched by some authors, owing to their particular characteristics, intermediate between SWNT and MWNT. Most SWNT samples synthesized by CCVD also contain a more or less high proportion of DWNT [135,137,184,185] and thus, the

synthesis parameters can be adapted to obtain a large proportion of DWNT. Ren et al. [186] used ferrocene and thiophene vapours in CH_4/H_2 at 1100°C and obtained CNT samples with about 70% DWNT (1.6–2.9 nm in diameter), often in bundles, with some disordered carbon deposit. Flahaut et al. [187] adapted the method of Tang et al. [179] using a Co- and Mo-containing MgO-based oxide and obtained CNT samples with about 80% DWNT either individual or in small bundles (Fig. 25), without any disordered carbon deposit, and with a yield of 13 wt.%, calculated from the weight of the starting catalytic material.

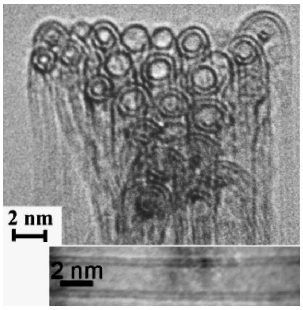

Fig. 25. HRTEM images of a bundle of DWNT and of an individual DWNT synthesized by decomposition of CH_4 over Co nanoparticles which are generated in situ by the selective reduction of a MgO-based oxide solid solution containing additions of Mo oxide [187]. Reproduced from E. Flahaut, R. Bacsa, A. Peigney, and C. Laurent: Chemical Communications, 1443 (2003), by permission of The Royal Society of Chemistry

Localized Synthesis of Carbon SWNT

Because the CNT manipulation is very difficult and can cause some damages which may modify their electronic properties, many researches are conducted to locally synthesize CNT in-situ on a preformed electronic substrate. Kong et al. [188] patterned silicon wafers, by a lift off process, with micrometer scale islands of catalytic material made of alumina nanoparticules impregnated by Fe and Mo salt solutions. CNT, many being SWNT (1–3 nm in diameter, tens of micrometers in length) were grown by CCVD with CH_4 at 1000°C during 10 min, some of them bridging the metallic islands. Franklin et al. [189] prepared Co, Mo and Al precursors of oxide and printed this material on the top of Si towers. After calcination at 500°C during 12 h, the CCVD is conducted at 900°C in CH_4 during 20 min giving numerous SWNT bridging the Si towers (Fig. 26). It seems that one of the key points of the method was the use of a bulk amount of conditioning catalyst which was placed upstream of the patterned substrate.

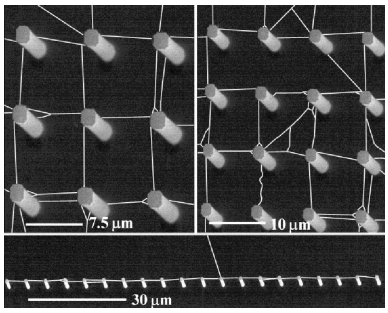

Fig. 26. SEM images of networks of suspended SWNT grown from silicon towers by the enhanced CCVD method described by Franklin et al. [189]. Reproduced from N. R. Franklin, and H. Dai: Adv. Mater. (Weinheim, Ger.) **12**, 890 (2000)

Conclusions

SWNT are efficiently prepared by CCVD using nanometric catalytic particles which can be either formed in-situ from an organometallic precursor in a gas flow or supported on a solid substrate material. In the first case, Fe particles are generally preferred and are formed from vapours of ferrocene or $Fe(CO)_5$. These syntheses are conducted at high temperatures (1100–1200°C) with C_2H_2 or C_6H_6 and it seems that some supply of sulphur is beneficial. Using $Fe(CO)_5$ and CO at 10 atm and 1200°C, the HiPCO method produces good quality SWNT by a continuous process. Many ways have been studied to prepare nanoparticles (generally Fe, Co or alloy) on an oxide substrate, which are sufficiently stable to act as catalyst at high temperatures. They can be generated in-situ, in the reactor, by selective reduction of an oxide solid solution, or pre-formed ex-situ as oxide particles which are reduced into metal during the reaction, or prepared in the metal form before the reaction. The addition of Mo containing species during the preparation of the catalyst is determinant to increase both the selectivity and the SWNT yield. Among the substrates, MgO is preferable because it can be easily removed with non-oxidative acids. CH_4, which decomposes at high temperatures, generally mixed with H_2, notably to avoid the formation of disordered carbon, is often preferred. The temperature of the reactor is chosen according to the nature and partial pressures of the carbonaceous and auxiliary gases. It has not yet been demonstrated that samples containing 100% SWNT can be prepared by CCVD. In comparison with SWNT produced by arc-discharge or laser ablation, CCVD SWNT samples have a larger distribution in diameter but their Raman spectroscopy spectra can nonetheless present a very small D band, which is characteristic of very few disordered carbon or defects, and often show very well-defined RBM modes, which is characteristic of populations with a well-defined diameter. Because many parameters are adjustable in the

CCVD method, the characteristics of CNT (SWNT or DWNT, diameter) are also adjustable.

3.4 Template Synthesis of Carbon Nanotubes

Porous materials, particularly those with cylindrical pores can be used as template to deposit carbon, without any catalysis step, which corresponds to chemical vapour deposition (CVD) methods or with the help of a catalytic particle (CCVD methods). Che et al. [190] used an alumina commercial membrane (60 µm thick, pores 200 nm in diameter) and obtained, by pyrolysis of C_2H_4 or pyrene (in a Ar flow) at 900°C, very well aligned carbon filaments which can either be hollow (nanotubular form - Fig. 26) or not (nanofibres) as a function of the deposition time (10 and 40 min, respectively). When the pores are impregnated with Co or Fe salts which give metal particles after calcination and then reduction in the reactor, the deposition process (here CCVD) gives carbon fibres which can grow out of the pores and fuse together in bundles. Heating the carbon nanofibres at 500°C during 36h is sufficient to obtain a well-graphitized structure. Jeong et al. [191] prepared an alumina porous membrane (200 µm thick, pores of 80 nm in diameter) by a controlled anodic oxidation of Al, and performed an electrolytic deposition of Co and a pre-reduction (H_2/Ar, 500°C). The CCVD deposit was made from a $C_2H_2/H_2/N_2$ gas mixture at 650°C (40 min) and produced graphitized MWNT which grew out of the pores. The sonication of the obtained material allow the cutting of the MWNT to lengths between 50 and 400 µm. Xie et al. [192] prepared mesoporous SiO_2 (pore diameter 30 µm) by a sol-gel method, and impregnated it with Fe nitrate. After calcination and pre-reduction (H_2/N_2, 550°C), well graphitized MWNT (around 30 nm in diameter) were obtained by CCVD from the decomposition of C_2H_2 at 700°C. The template method is efficient to synthesize open MWNT with a narrow distribution of diameter, very well aligned into the pores or more or less aligned when they grow outside the pores. The CCVD method is preferred when a good crystallinity of the MWNT is desired. The template method can also be used to synthesize SWNT. Tang et al. [193] obtained tripropylamine embedded in 0.73 nm channels of microporous aluminophosphate crystals which decomposed, by pyrolysis at 350–450°C, to give a monodimensional carbon deposit. A treatment at 500–800°C converted the deposit into crystallized SWNT with very small diameter (< 0.7 nm).

3.5 Conclusions

The results on the synthesis of CNT by CCVD methods have been published very recently, mainly from 1997 onwards. The key parameters of a successful method are of two kinds. Firstly, the parameters related to the starting material (i.e. the metal source and/or substrate) that aim at controlling the

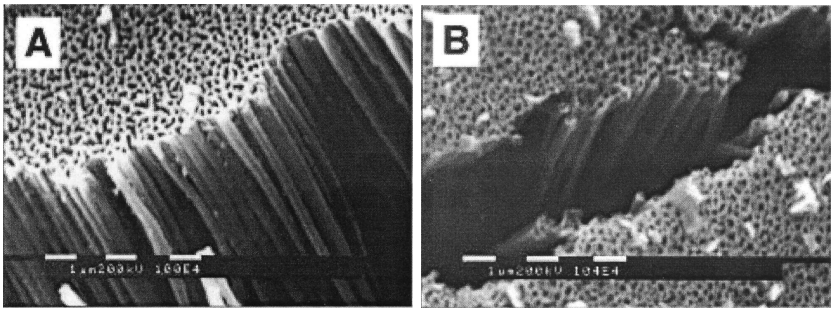

Fig. 27. SEM images of CNT obtained by chemical vapor deposition of carbon (CVD, without catalyst) on the walls of pores of an alumina membrane, using ethylene (**A**) and pyrene (**B**), during 10 min at 900°C. The template membranes have been dissolved in concentrated HF [190]. Reproduced with permission from G. Che, B. B. Lakshmi, C. R. Martin, E. R. Fisher, and R. S. Ruoff: Chem. Mater. **10**, 260 (1998), copyright 1998 American Chemical Society

formation of the catalytic metal nanoparticles with the appropriate diameter. Indeed, MWNT can be obtained preferentially to nanofibers, and SWNT (or DWNT) can be obtained preferentially to MWNT by decreasing of the size of the catalytic particles (generally Fe, Co) and stabilising their size at the high temperature of the reactor. Secondly the parameters related to the carbon deposition reaction, which include the appropriate choice of the carbonaceous gas, of the auxiliary gas(es), of the proportion and flow of the gases, of the reaction temperature and pressure.

CCVD methods are promising because they are of a low cost, they can be upscaled in continuous processes by multiple technical solutions, they involve a lot of parameters which can be optimized to adjust the selectivity towards the synthesis of SWNT, DWNT or MWNT, with small or large diameters. Moreover, the CCVD allows the localized and/or oriented growth of CNT. Until recently, CVD methods generally resulted in poor quality SWNTs or MWNTs. However the quality of the tubes produced in this way is becoming better and better, so that they are now used in transport devices as NT produced through high temperature routes.

4 Nucleation and Growth of C-SWNT

4.1 Summary of the Synthesis Conditions of C–SWNT: Similarities and Differences of the Different Synthesis Methods

We have seen in the previous sections that C–SWNTs can be produced via both high temperature routes and CCVD processes. In spite of obvious differences, synthesis conditions have all in common to involve a metal catalyst.

In the high temperature evaporation based routes, carbon and metallic elements (Co, Ni, Y, La, ...) are vaporized at temperatures above 3000 K and then condensed at lower temperatures in an inert gas (He, Ar) flow and single wall nanotubes are believed to form at about 1500 K. In particular, the use of a pulsed laser in the laser ablation method requires to place the reactor in an oven heated at at least 1300 K to obtain significant yields in SWNT. The CCVD based routes use the decomposition of an hydrocarbon gas (methane, ethylene, ...) or of CO at the surface of catalytic particles (Fe, Co, Ni) which are either supported on a substrate or synthesized in situ from a solid or liquid precursor and sprayed in the furnace heated at temperatures between 750 and 1200°C.

The analogies between these fairly different methods are actually remarkable: First, the morphologies of the SWNTs produced by the different techniques are very similar. In each case, SWNTs can be found isolated or self-assembled in crystalline bundles, their diameter varying from 0.7 to 5 nm. These correlations suggest that a common mechanism could explain the growth of SWNTS. Second, for all synthesis techniques, catalysts such as Ni, Co, Fe, Y, La or mixtures of them are necessary to obtain SWNTs. Several questions then arise which concern the role played by the temperature and the metallic catalyst: is the catalyst active at the atomic level or as a cluster, in a liquid or a solid state and through which catalytic reaction processes?

In nanotubes, carbon has a structure which is not very different from its most stable structure at equilibrium, i.e. graphite. Nanotubes can therefore be considered as particular sp^2 carbon structures. As for carbon fibers, understanding their formation requires an analysis of the transformation paths of carbon from the vapour to the solid state which themselves depend on the phase transformations involved in the catalyst-carbon systems. From an experimental point of view two types of methods are used. Structural determinations and chemical analyses of the synthesis products are made ex situ after the synthesis using local or global probes techniques whereas in situ diagnostics in evaporation-based synthesis reactors are now becoming available [43]– [39]. Among the techniques used in post-synthesis analyses, transmission electron microscopy plays a major role since it is the only technique able to provide structural and chemical informations [197]. In situ diagnostics inspect the temperature, nature of species issued from the target vaporization, time evolution of the matter aggregation after the initial vaporization (see Sect. 1). It is worth mentioning that there is no specific diagnostic, until now, able to identify the nanotube onset in high temperature processes and therefore to identify directly the role played by metal atoms. From a theoretical point of view, thermodynamic treatments at the mesoscopic level [198,200] as well as atomistic modelizations (starting from ab initio or empirical interatomic potentials) [201, 202] have been developed .

Although the situation is not completely clear yet, some realistic scenarii begin to emerge from these different approaches [204]. In the following,

we shall focus on the phenomenological models of nucleation and growth which can be deduced from microscopic analyses of the nanotubes and their catalysts in TEM [205] and from in situ diagnostics data, with a particular emphasis on the growth of nanotube bundles in the evaporation-based routes. Next section (Sect. 5) is devoted to atomistic simulations of growth mechanisms using ab initio or empirical interatomic potentials.

4.2 Towards a General Phenomenological Model of Nucleation and Growth

Analysis of the Link Between Catalyst Particles and SWNTs

Since samples generally consist of a mixture of metallic particles and of an entangled network of nanotubes, isolated or assembled into bundles. Observations have been paid, in a first step, to the identification of the relationships between particles and bundles. The entangled nature of nanotube networks makes these observations very difficult, since it is in general not possible to find the tube ends as mentioned in the first experimental investigations [34]. However, recent detailed high resolution transmission electron microscopy (HRTEM) analyses indicate that, actually, whatever the synthesis process [34,48,127,132,196,218], SWNT nucleate and grow from the catalytic particles [202]. Figs. 28–29 show different examples of SWNTs extremities observed in samples produced by different high and medium temperature techniques. In all cases, it is found that the nanotubes are attached by one extremity to small (5–20 nm in diameter) metallic particles although differences in the size of the particles, in the number of tubes per rope and in the crystallinity of the tubes are evident. The situation where the nanotubes are short (¡ 400 nm) is of particular interest since both tube extremities can be observed simultaneously, which is quite impossible for long tubes because of their entanglement : in those cases (Fig. 29 and Fig. 28c), it is clearly seen that one tube extremity is attached to the particle and the other is closed and empty. The situation shown in Fig. 29b, where numerous bundles corresponding to several tens of SWNTs emerge radially from a given particle, is called a sea urchin structure and has been observed for different catalysts [24, 52, 194, 207, 208]. Finally, very short tubes corresponding to bundle embryos or nuclei have been clearly identified and different situations are seen in Fig. 29c–e. Fig. 29c shows a bundle embryo whereas in Fig. 29d,e a single nanotube is emerging from the particle.

It results from these observations that there are basically two situations. In the first case the tube growth is *perpendicular* to the surface of the particle. This is the general situation encountered in the evaporation based route, where the particle are fairly large (5–20 nm) (Fig. 28a, d, e, f and Fig. 29a, b) (see also [209]) but it is sometimes observed in CCVD samples (see Fig. 28b) [127, 196]. In this growth mode, the tubes are most frequently arranged in bundles (see Fig. 28a, b, d) but single tubes emerging perpendicularly to

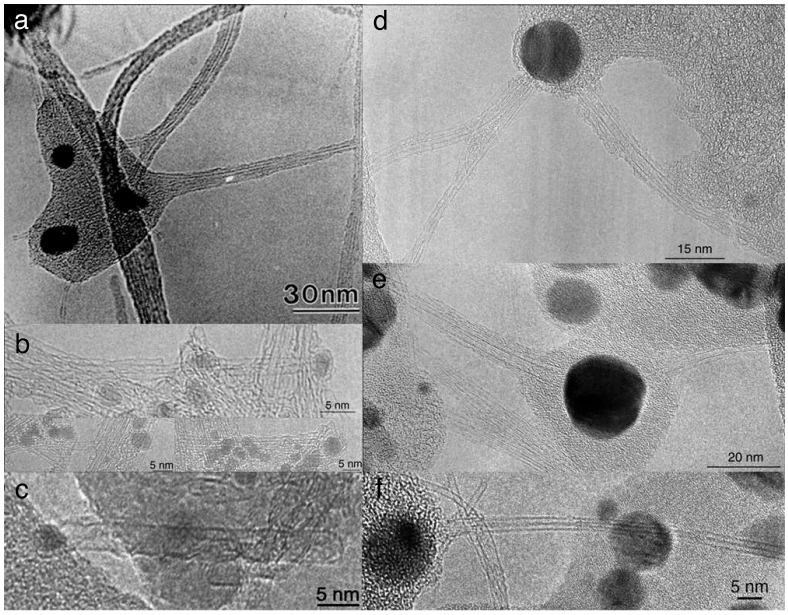

Fig. 28. HRTEM images (Jeol 4000FX, Cs = 3.2 mm)) of long SWNT ropes emanating from metallic particles synthesized by various methods : (**a**) electric arc discharge described in [20] with a Ni-Y catalyst where the Y/Ni ratio is equal to 0.2, (**b**) HIPCO CCVD process described in [132], (**c**) CCVD procedure described in [127,196]. (**c**) pulsed laser ablation described in [34], (**e**) and (**f**) continuous laser vaporization described in [48]. Note that in (**a**) the particle size is much smaller than in the other cases and that the ropes contain a reduced number of tubes. When the particle is large (**d, e**), two ropes or more can emerge from it. Futhermore, it is frequently observed, as it can be seen in (**a**), that bundles issued from distinct particles attract each other according to a branching process and form a composite rope [218]. Finally, note that in (**c**) the diameter of the tube is related to that of the particule in contrast with the situations shown in the other cases

the surface of the particles can also be observed as in Fig. 29d. In such cases, the diameters of the tube are not correlated with the size of the particle. In the second case, the growth is *tangential*; the particles are generally smaller (1–5 nm) and are found encapsulated at the tip of the tubes (Fig. 28c and Fig. 29e), thus determining their diameter. Many other examples can be found in the litterature as for instance in [125]. This growth process has, to our knowledge, only be observed in the CCVD methods.

Phenomenological Model of Nucleation and Growth

The tangential growth process, observed for CCVD SWNTs, should be similar to that put forward to explain the growth of vapour-grown carbon filaments

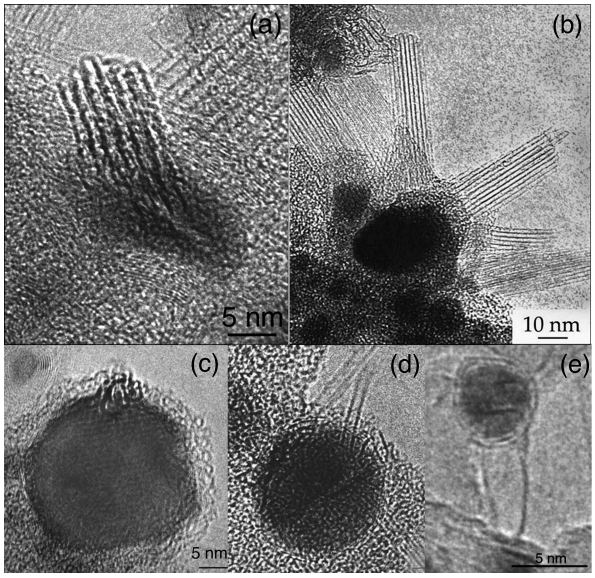

Fig. 29. HRTEM images of different short ropes attached to the metallic particles. Samples are synthesized with the electric arc and with a Ni-Y catalyst where the Y/Ni ratio is equal to 0.5 in (**a, b, c, d**) and by the CCVD process described in [127, 196] in (**e**). In (**a**) the rope is strongly inclined with respect the electron beam whereas in (**b**) different ropes are emerging radially from the particle in different spatial directions reminding to a sea-urchin hence the name given to these morphologies. In (**c**–**e**), the nanotubes are seen as elongated caps having a length between 3 and 5 nm. The image (**c**) shows embryos of a SWNT bundle. In other cases only one nanotube is emerging from the particle whose size is not correlated to that of the tube in the case (**e**). It is worth noticing that in this particular case, the graphitic walls of the tube are tangent to the surface of the particule whereas in the other cases, the tubular sheets are perpendicular to the particle surface

from liquid particles which is based on the VLS model (see Sect. 2 and Fig. 30a) [80, 85]: the nanotubes can be considered in this case as ultimately small carbon filaments (Fig. 30b) [125]. The process, sketched in Fig. 30, involves a chemisorption and decomposition of the carbonaceous gas at the surface of the particle, the dissolution and the diffusion of carbon within the particle and its segregation and graphitization parallely to the surface of the particle, once the particle gets saturated in carbon. A carbon cap (called yarmulke) is formed on the top of the catalytic particle which decreases the surface energy. Then, either the carbon shell continue to grow and cover the particle, deactivating it and forming a carbon capsule, or the cap lifts up, forming the cylindrical form of a SWNT, or a second cap is formed under the first one before their lift up, forming a DWNT. The carbon concentration gradient between the surface and the bulk of the particle insures the continuity of the

process as long as the temperature and gas supply, at a rate avoiding the catalyst poisoning, are maintained [220]. The diameter of the tube emerging from the graphitization process is naturally determined by the size of the particle which, during the growth, can either be rejected at the tip or be kept at the foot of the tube and attached to the support.

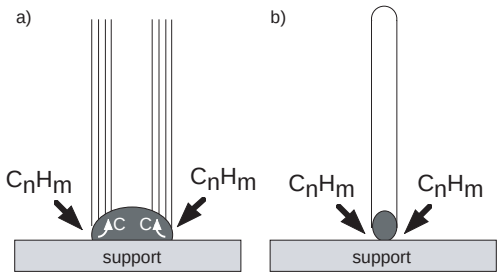

Fig. 30. a) Simplified schema for the formation of carbon filaments obtained from CCVD methods [80, 85] and its adaptation to the formation of SWNT growing tangentially to the surface of the particle in (**b**)) [125]

Such a process, however, fails to account for the situation, typical of the vaporization routes, where the growth is perpendicular to the particle. Different alternative models have been tentatively proposed in the recent years. First, a direct formation process in the gas phase has been considered [34]: catalyst acts through aggregates reduced to a few atoms located at the tip of the nanotube, either preventing its closure by scooting around and stabilizing the reactive dangling bonds or leading the tip to remain chemically active [203] or stabilizing structural defects and acting as attraction sites for carbon adatoms [210]. This model will be discussed in detail in Sect. 5. Other models involve the growth from a liquid metallic particle, the SWNT nucleation step being a highly debated issue. It has been suggested, in particular, that preformed fullerenes could play the role of nucleation seeds [211].

On the basis of the TEM observations described above, a simple model has been developed, which adopts the concepts of the so-called VLS (vapor-liquid-solid) model introduced for explaining the growth of silicon whiskers [116]. The adaptation of the VLS approach to the growth of SWNTs was first proposed by Saito et al [24, 206, 207], for explaining the formation of sea-urchin-like structures. It has been then extended to the formation of both individual SWNTs and SWNTs bundles, which are emerging perpendicularly from the particle [197, 202]. In this type of model, the growth of nanotubes is believed to proceed via solvation of carbon vapor into metal clusters, followed by the precipitation of carbon excess in the form of nanotubes. The mechanism is based on the ability of metals such as Ni, Co to dissolve carbon when liquid and to almost completely segregate upon solidification, therefore allowing

graphitization of carbon at temperatures as low as 1500K [45, 204]. These properties can be directly deduced from the thermodynamic phase diagrams of Ni (Co) - C systems recalled in Fig. 31 [45]. Fig. 32 presents a simplified

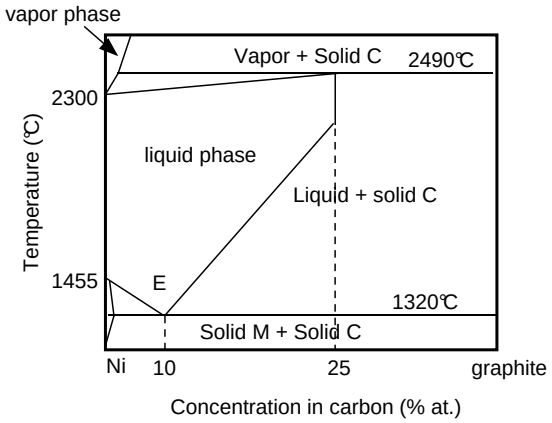

Fig. 31. Schematic phase diagram of the C-Ni system adapted from [45]. The C-Co diagram is quite similar

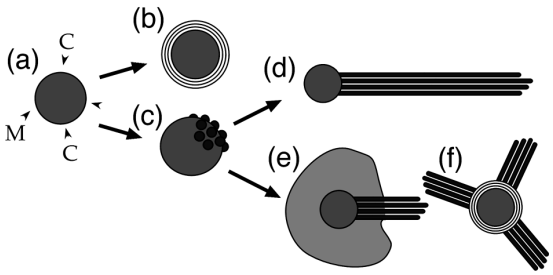

Fig. 32. Scenario derived from the VLS model, for the nucleation and growth of SWNT

sketch of the proposed scenario. The first step (Fig. 32a) of the process is the formation of a liquid nanoparticle of metal supersaturated with carbon. These nanoparticles originate from condensation of the metal plasma/vapor in the moderate temperature zone of vaporization based reactors. Upon cooling, the solubility limit of carbon decreases and carbon atoms segregate towards the surface where they precipitate. The second step (Fig. 32b, c) is the formation of nanotube nuclei at the surface of the particle which is competing with the formation of a graphitic sheet wetting the surface of the particle. The last step (Fig. 32d, e, f) is the nanotube growth which is likely to proceed by a

progressive incorporation of carbon at the interface particle - nanotube. This scenario, which implies a root growth mechanism, is supported by the different TEM observations presented above, for the nucleation step at least, and by ab initio calculations [202] (see Sect. 5). Furthermore, in situ diagnostics performed in laser methods [39, 42–44] and solar furnaces [54] (see Sect. 1) provide informations consistent with the first step. We discuss below in more details these different steps with a particular attention to the nucleation one which is the most crucial.

Particle Formation and Carbon Segregation

The presence of metal atomic vapours and of C_2 molecules is attested by the in situ diagnostics [39, 42, 43, 54] done in continuous and pulsed vaporization reactors. As expected from thermodynamic data (Fig. 31), carbon condenses first, about 100 µs after vaporization. In pulsed laser reactors, the signal corresponding to the metallic vapour disappears ten times later than the C_2 signal. Because of the high quenching rate, expected to be 105–106 K/s in continuous laser reactor [39] and solar furnace [44], carbon condenses in a low density amorphous state. Neither graphite nor diamond crystallites have been detected in the synthesis products. From in situ measurements [39, 42], metal condenses below 2300 - 2000°C resulting in the formation of liquid particles (Fig. 32a). The nanoparticle size is determined by parameters such as temperature gradients, gas pressure and flow, etc. [38, 40, 212]. At this stage, these particles can dissolve a substantial amount of carbon, up to 25 at. % at 2000°C as indicated by the phase diagrams (Fig. 31) and probably much more, up to 50 60 % [213], when the particle are very small. Phase diagrams (Fig. 31) also indicate that the solubility limit drastically decreases down to a few at. % as the temperature is falling down to the eutectic temperature (T = 1400°C), where the metal solidifies. The solidification gives rise to a phase separation between an almost pure metallic phase and a solid pure carbon phase. The phase separation proceeds by a segregation of carbon towards the surface of the metallic particle because of two combined effects: the drastic difference of energy of the respective surface tensions of metals and carbon [204] and the reduced particle size. This phenomenon of surface segregation has been confirmed by ab initio calculations done in the Co–C system [197, 202].

Nucleation

Once expulsed, carbon crystallizes at the surface of the particle according to two competing transformation paths (Fig. 32b, c), which lead either to graphene sheets wrapping the particle and wetting its surface or to SWNTs nuclei with graphitic walls perpendicular to the surface, that is, non wetting it. Since equilibrium surface energy arguments play in favor of the first configuration [204], it has to be assumed that the SWNTs nuclei result from a

particular surface process, for which the graphene sheet becomes unstable. As explained above, the segregation force increases upon cooling and is maximum close to the solidification. If the segregation velocity is low, carbon can be progressively and gently extruded in such a way that carbon atoms get organized by surface and bulk diffusion in the most stable configuration, that is, the graphene sheet. On the contrary, when the segregation velocity is high, the carbon flux is too rapid to permit, by diffusion, progressive incorporation of atoms at the edges of a graphene layer and because of this conflict surface instabilities occur.

The precise nature of these instabilities is for the moment a debated issue, discussed in detail in [204]. One can imagine dynamic instabilities as those involved in the formation of dendrites in solidification processes [214] or quasi static instabilities similar to those involved in crystal growth produced by molecular beam epitaxy deposition [215]. The latter analogy is very appealing indeed if one replaces the deposition flux by a segregating carbon flux. The equivalent of a layer-by-layer growth (or Frank-van der Merwe process) would be here the formation of graphene sheets whereas the formation of islands (Volmer-Weber or Stranski-Krastanov processes) would be equivalent to the growth of nanotubes (for details see [204]). The limit of these analogies lies in the difference in scales compared to the length and the diameter of the nanotubes: macroscopic size of the dendrites in the first scale, nanometer heigth of the islands in the second case. In all cases, the instability is governed by two control parameters: one is the surface energy and the second one can be, depending on the system in turn, a kinetic energy as in dendritic solidification, a concentration gradient, elastic and chemical energies which determine the wetting properties of the surface. In our case, the carbon surface tension is clearly one parameter, whereas the second one should be related to the chemical nature of the catalyst and to the kinetic conditions of cooling. In particular, the surface layer of the catalyst should have a particular structure and chemistry in such a way that its energy becomes unfavorable to the wetting of the graphene sheet, which is a condition required for the SWNT nucleation. We will see, in Sect. 4.3, how this condition is achieved in the case of the Ni-R.E. catalyst. Finally, since the nucleation of bundles can occur, the instability should be cooperative in order to explain the collective formation of an assembly of nanotubes. Recent observations done on bundles produced by CCVD [216] methods indicate that, for small bundles, all the tubes have the same helicity, attesting for a cooperative nucleation process.

Growth and End of the Growth

Once the nanotube nuclei are formed, growth should proceed through further incorporation of carbon. Carbon initially dissolved in the particle should continue to condensate at the root but this is not sufficient to produce long (one micron ore more) SWNTs bundles [197]. For instance, a nanoparticle of 15 nm in diameter and containing initially 50 at.%C can give rise to either

one SWNT of one micrometer long or to a bundle of ten SWNTs of 100 nm each [197]. Another source is therefore necessary which is naturally the density of the remaining amorphous carbon. The incorporation of this carbon can follow the dissolution-process based on a concentration gradient within the particle and invoked in the growth of filaments in CCVD methods or can directly be incorporated at the root of the nanotubes. This root growth process is also attested by atomistic simulations as shown in Sect. 5.

In order to achieve long nanotubes (Fig. 32d), the growth should therefore continue for a sufficient long time, as attested by in situ diagnostics, which indicate growth time longer than tens of ms, and post synthesis annealing experiments [42], until local temperatures are too low, leading to the solidification of the nanoparticles. These conditions defines a kind of stationnary regime where the kinetics of incorporation of carbon in the tube walls is compatible with the cooling kinetics and the carbon supply. These constraints certainly explain the necessity of using in the pulsed laser reactor an oven heated at around 1500K, that is at a temperature close to the metal solidification temperature [34, 36]. Such an oven is not necessary in continuous vaporisation methods [35, 37, 39, 52], since in this case the carrier gas is heated in the vicinity of the target and acts as a local furnace, as shown by in situ measurements (Sect. 1).

Different morphologies can arise, which are sketched in Fig. 32e, f, when the local conditions have been perturbed in such a way that the growth has stopped. According to the root growth process, looking at the feets of the nanotubes provide information on the end of the growth, and how this has been perturbed, before to stop. The remaining carbon, which was immediately available for the growth, can partly condense into amorphous carbon flakes embedding the particle (an example can be seen in Fig. 28) or into a few graphitic layers wrapping the particle and building a buffer layer between the nanotubes and the particle (examples can be seen in Fig. 29). The former case (Fig. 32e) suggests a rapid decay of the local temperature whereas the latter situation (Fig. 32f) means the occurrence of a bifurcation from the nanotube growth towards the continuous layers growth. This bifurcation is an additional proof that nanotubes and graphitic layers do not occur for the same local conditions of carbon segregation [219]. Different morphologies can thus emerge from a same particle provided that the local experimental conditions suited for their growth are successively achieved.

4.3 Microscopic Approach of the Nucleation for a Particular Family of Catalyst : the Case of the Ni-R.E. Catalysts

Experimental Procedure

The nucleation step, discussed in the previous section, has been investigated in detail in the case of the Ni (R.E. = Y, Ce, La) catalysts by examining the structure and the composition of the particles linked to the different

SWNTs morphologies. We focused on this particular class of catalysts since they are preferentially used in continuous vaporization routes such as the arc discharge method [20] and the continuous laser reactor [35, 40]. It has indeed been recognised that the highest SWNT production rate is achieved when a few amount of a rear earth element such as Y is added to the transition metal catalyst. To study the influence of the R.E. addition on the SWNT formation, different rare earth elements Y, Ce, La - with different compositions (from 0 to 100%) have been tested. SWNTs were synthesized by the arc discharge method with the conditions given in [20].

SWNTs Morphologies and Catalyst Composition

As a general result, identical results have been found for the three R.E. tested. The yield in nanotubes is extremely sensitive to the anode composition. The SWNT production rate has been found to be maximum for a nominal anode R.E /Ni. ratio between 0.2 and 0.5 and to drastically decrease by a factor up to ten out of this composition range. Futhermore two kinds of tube morphologies have been observed, in various proportions depending on the anode composition: long ropes as in Fig. 28a, or sea-urchin-like structures as in Fig. 29b. Pure Ni produces long ropes only (in low yield) whereas pure R.E. produced sea-urchin structures only. For intermediate anode compositions, both types of tubes are observed in a proportion related to the amount of R.E. . X-ray analysis of the composition of the particles has shown that long ropes are always linked to particles whose composition R.E. / Ni is lower than 11 at.% whereas particles of sea-urchin-like structures have a composition R.E. / Ni larger than 15 at.% [197]. As a reference, the composition of the particles which are not linked to SWNTs is completely random. Finally, this relationship between particle composition and SWNTs morphologies is found whatever the nominal R.E. / Ni anode ratio.

Particle Analyses

It results from this first analysis that the particle structure and composition are crucial parameters to be identified for explaining the differences observed between the SWNT morphologies. Chemical maps, chemical profiles and high resolution images have been recorded in TEM by combining HRTEM and EELS on numerous particles linked either to long ropes or to sea-urchin-like structures. In the case of long ropes, chemical maps shown in Fig. 33 reveal that the core of the particle is pure Ni whereas the surface is partially R.E. enriched. Line-scan profiles extracted along a section of the particle [219] provide a clear quantitative evidence of the spatial anticorrelation between Ni and R.E.. R.E. is not uniformly distributed at the surface but is concentrated in thin platelets which are clearly recognised in HRTEM images since they display a dot pattern different from the core (Fig. 33a, b). These differences

reveal that the composition variation has a structural counterpart. Analyses of the different patterns have revealed that the core has the FCC structure of nickel whereas the platelets have the structure of the carbide R.E.C_2 [204]. Furthermore, platelets have been found to display two important features: their thickness is in general restricted to 2–3 atomic layers and they are always oriented with their (110) plane parallel to the surface.

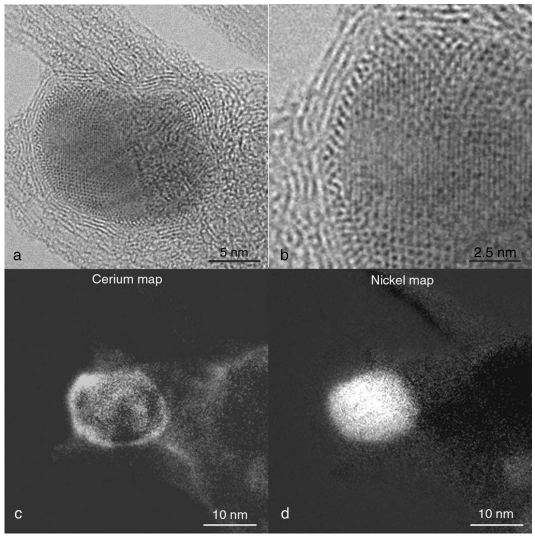

Fig. 33. (**a**) HRTEM image of a particle with an enlargment in **b**. (**c**) Ce, (**d**) Ni chemical maps (EFTEM images at Ce-N4,5 edge and Ni- M2,3 edge, Jeol 3010 equipped with a Gatan energy filter (GIF) operating at 300kV) of a particle linked to long SWNT ropes in the case of a Ni-Ce catalyst. Ce and C mostly located at the surface of the particle whereas Ni is located in the core of the particle. Furthermore, location of Ce and C is correlated with the observation, in the HRTEM image, of a strong white dot contrast which is not seen in the bulk of the particle and which is the evidence that the surface has a different crystalline structure than the bulk, adapted from [204]

The identification of the surface platelets is very crucial and provides the key of the SWNT nucleation. Indeed, their presence has been found to be directly related to the nucleation of SWNTs since a direct link between the ropes and the platelets has been frequently observed, as attested in the example shown in Fig. 34 (see also examples in [204]). The platelet is lying at the top of the particle in the plane of projection so as it is imaged by a fringe contrast and the feets of the SWNTs of the rope are clearly attached at the surface of the platelet.

The particles linked to sea-urchins are different. The same carbides are observed at the surface but now they cover uniformly the surface as a thin

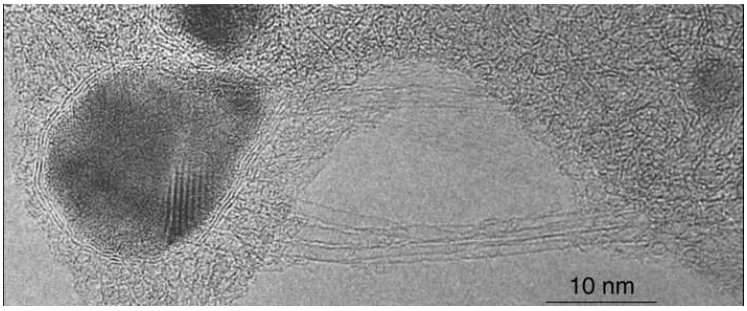

Fig. 34. HRTEM images illustrating the link between the carbide at the particle surface and the roots of the long ropes. The carbide platelet is lying at the top of the particle and seen with a fringe contrast, adapted from [204]

shell (2–3 layer thick) encapsulating the particle [219]. Furthermore, the core is now a complex Ni-R.E.-C compound such as the R.E.NiC_2 compound or the R.E.C_2 carbide itself when the catalyst is 100 % R.E. [[197, 208]. This total higher R.E. concentration is fully consistent with EDX analyses. In addition the core is frequently microcrystalline, which was not the case of pure Ni cores, suggesting rapid solidification due to rapid cooling conditions.

Nucleation Model: the Catalytic Role of Rare Earth Elements

The results presented above can be summarized as follows: the nanotube nucleation is directly linked to the presence of R.E.C_2 carbide at the surface of the particle, the number of nanotubes emerging from it being directly related to the covering of the particle by the carbide layers. Furthermore, the length of the tube is linked to the presence of R.E. in the core: when present, the length remains below 100 nm whereas in the other case there is no limitation in the length, nanotubes can achieve.

For explaining the role of the R.E. in the nucleation, one has first to explain the formation of the surface carbide. This results from the combination of two properties of the R.E. metals: their abilities to form a stable carbide, with melting temperatures higher than that of Ni (for example, the melting temperature of YC_2 is equal to 2415°C) and their low surface energy which is about ten times lower than that of carbon. This second effect induces a co-segregation of C and R.E. at the particle surface at temperatures higher than the solidification point of the particle. Once at the surface, because of the first effect, R.E. and C self assemble to form a chemically ordered surface layer, which is likely to be seen as a raft floating at the surface of the particle. More precisely, since the carbide layer is experimentally found to always have the (110) orientation, the chemical ordering of the surface layer should resemble the chemical ordering of the (110) plane of the carbide. This plane consists of a regular pattern of carbon pairs and of R.E. atoms [204]. It is

striking that the carbon pair spacing, equal to 0.12 0.13 nm, is very close to the first neighbour distance in the graphene structure. This peculiarity strongly suggests that the carbon pairs can serve as nucleation sites for a graphitic network perpendicular to the surface. This would be the starting point for the formation of SWNTs nuclei.

Furthermore, the presence of R.E. atoms mixed with the carbon pairs is thought to help stabilizing SWNTs nuclei thanks to a third property of R.E., which is its ability to transfer electrons to carbon. This effect has been studied thanks to simulations using a tight binding modeling of C–C interactions combined with Monte Carlo simulations [204]. These calculations have shown that when the number of electrons is increased, which mimics a charge transfer, the graphene sheet is destabilized in favour of configurations involving pentagons and heptagons. These defects introduce local curvatures which are necessary for building a SWNT nucleus linked by the foot to the surface [201, 209]. Therefore, it can be inferred from these simulations that charge transfer effect of R.E. plays in favor of the formation of a SWNT nucleus instead of a graphene layer.

In summary, the carbide surface layer can be seen as a diffuse carbon-rich interface between Ni and graphitic carbon where strong metalcarbon bonds are involved which modifies the properties of the surface of Ni in such a way to avoid the wetting of graphene layers. R.E. carbides are thus found to play an important role in the parameters controling the surface instability responsible for the SWNT nucleation.

The arguments put above make clear that the density of nucleation sites is directly determined by the R.E concentration of the particle. A low concentration gives rise to a partial carbide covering and to a few number of SWNTs assembled into a rope. This corresponds to the first SWNT morphology. On the contrary, a high concentration provides a complete surface covering by the carbide and an isotropic distribution of nucleation sites which results in the sea-urchin structure.

Let us now discuss the difference in length between long ropes and see-urchin structures. As said previously, growth stops when the particle solidifies or when the carbon source is exhausted. If the growth proceeds by the incorporation of carbon via a dissolution-precipitation process, the presence of a continuous carbide layer at the surface, at high concentration of R.E., can act as a poison to the dissolution process since the layer is saturated in carbon. The carbon initially dissolved in the particle is therefore the only feeding source for growth. In addition, the observation that R.E. rich particles are microcrystalline, indicates a solidification in a high temperature gradient. Since in situ temperature measurements indicate that higher the temperature higher the local temperature gradient [39], R.E. rich particles are likely to solidify at higher temperature than Ni. At such temperature, due to the corresponding high temperature gradient, the residence time of the particle at temperatures suitable for the growth has been very short. In Ni rich particles,

on the contrary, longer residence time can be achieved resulting in extended growth. Both effects poisoning and rapid solidification may explain why tubes of sea-urchins remain short whereas, at low R.E. concentration, long tubes are observed.

4.4 Conclusion

It is general conclusion from microscopic observations that, whatever the synthesis technique and the tube morphology, SWNTs nucleate and grow from catalyst particles. Depending on the synthesis technique, the tubes are observed to grow parallely or perpendicularly to the surface of the particle. In the former case, observed in CCVD synthesis techniques, the diameter of the tube is correlated to that of the particle which is trapped at the tip of the tube, whereas in the latter case, mostly found in vaporization based synthesis techniques, there is no correlation between the diameter of the tube and that of the particle.

Phenomenological models of nucleation and growth have been discussed with a particular emphasis on the perpendicular growth of nanotube bundles since in that case the classical models of growth working for carbon filaments can not be applied as they do for the parallel growth situation. There is now strong experimental evidence in favour of a root growth process where carbon, dissolved at high temperature in catalytic particles, segregates at the surface at lower temperature and forms tubes via a nucleation and growth process. Particular attention has been paid to the nucleation step where the main problem is to understand why carbon does not always form graphene sheets wrapping the particles. This competition necessarily involves a surface instability where one control parameter is the low surface tension of carbon compared to metal transition.

The origin of this instability has been studied in detail for a particular class of catalyst Ni–R.E. (R.E. = Y, Ce, La) in order to understand why some addition of the R.E. drastically increase the production yield. Whereas Ni has the property to dissolve carbon in the liquid state and to reject it in the solid state allowing the graphitization of carbon at temperatures as low as 1400 K, R.E. is found to be a co-catalyst of Ni playing the role of a surfactant. It co-segregates with C at the surface of the particle and forms a chemically ordered surface layer which mimics the structure of the $R.E.C_2$ carbide. This chemical modification of the surface of Ni certainly inhibits its wetting by a graphene sheet and therefore contributes to the nuclation process and to control it. Many questions remain however open such as for instance the extension of the surface arguments identified for the Ni-R.E. class to other classes of catalyst (metal transition mixtures for instance), the nature of the parameter controlling the tube helicity and its diameter.

5 Growth Mechanisms for Carbon Nanotubes : Numerical Modelling

5.1 Introduction

In the following, we will address from a theoretical point of view, the growth of multi-wall and single-wall carbon nanotubes. One of our objectives will be to show that presently available simulation techniques (semi-empirical and ab initio) can provide quantitative understanding not only of the stability, but also of the dynamics of the growth of carbon nanotube systems. We will try to summarize the microscopic insight obtained from these theoretical simulations, which will allow us to isolate the essential physics and to propose good models for multi-shell and single-shell nanotube growth, and to analyze a possible consensus for certain models based on experimental data.

5.2 Open- or Close-Ended Growth for Multi-Wall Nanotubes

Assuming first that the tube remains closed during growth, the longitudinal growth of the tube occurs by the continuous incorporation of small carbon clusters (C_2 dimers). This C_2 absorption process is assisted by the presence of pentagonal defects at the tube end, allowing bond-switching in order to reconstruct the cap topology [221, 222]. Such a mechanism implies the use of the Stone-Wales mechanism to bring the pentagons of the tip at their canonical positions at each C_2 absorption. This model explains the growth of tubes at relatively low temperatures ($\sim$1100°C), and assumes that growth is nucleated at active sites of a vapor-grown carbon fiber of about 1000 Å diameter. Within such a lower temperature regime, the closed tube approach is favorable compared to the open one, because any dangling bonds that might participate in an open tube growth mechanism would be unstable. However, many observations regarding the structure of the carbon tubes produced by the arc method (temperatures reaching 4000°C) cannot be explained within such a model. For instance, the present model fails to explain multilayer tube growth and how the inside shells grow often to a different length compared with the outer ones [223]. In addition, at these high temperatures, nanotube growth and the graphitization of the thickening deposits occur simultaneously, so that all the coaxial nanotubes grow at once, suggesting that open nanotube growth may be favored.

In the second assumption, the nanotubes are open during the growth process and carbon atoms are added at their open ends [223, 224]. If the nanotube has a random chirality, the adsorption of a C_2 dimer at the active dangling bond edge site will add one hexagon to the open end (see Fig. 35).

The sequential addition of C_2 dimers will result in the continuous growth of chiral nanotubes. However, for achiral edges, C_3 trimers are sometimes required in order to continue adding hexagons, and not forming pentagons. The introduction of pentagons leads to positive curvature which would start

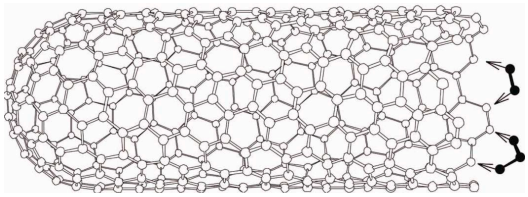

Fig. 35. Growth mechanism of a carbon nanotube (white ball-and-stick atomic structure) at an open end by the absorption of C_2 dimers and C_3 trimers (in black), respectively [222]

a capping of the nanotube and would terminate the growth (see Fig. 36). However, the introduction of a heptagon leads to changes in nanotube size and orientation (see Fig. 36). Thus, the introduction of heptagon-pentagon pairs can produce a variety of tubular structures, as is frequently observed experimentally.

This model is thus a simple scenario where all the growing layers of a tube remain open during growth and grow in the axial direction by the addition of carbon clusters to the network at the open ends to form hexagonal rings [224]. Closure of the layer is caused by the nucleation of pentagonal rings due to local perturbations in growth conditions or due to the competition between different stable structures. Thickening of the tubes occurs by layer growth on already grown inner-layer templates and the large growth anisotropy results from the vastly different rates of growth at the high-energy open endshaving dangling bonds in comparison to growth on the unreactive basal planes (see Fig. 36a). Figure 36c is a summary of various possibilities of growth as revealed by the diversity of observed capping morphologies. The open-end tube is the starting form (nucleus) as represented in (a). A successive supply of hexagons on the tube periphery results in a longer tube as illustrated in (b). Enclosure of this tube can be completed by introducing six pentagons to form a polygonal cap (c). Open circles represent locations of pentagons. Once the tube is enclosed, there will no more growth on that tube. A second tube, however, can be nucleated on the first tube side-wall and eventually cover it, as illustrated in (d) and (e) or even over-shoot it, as in (f). The formation of a single pentagon on the tube periphery triggers the transformation of the cylindrical tube to a cone shape (g). Similarly, the introduction of a single heptagon into a tube periphery changes the tube into a cone shape (h).The latter growth may be interrupted soon by transforming into another form because an expanding periphery will cost too much free energy to stabilize dangling bonds. It is emphasized here that controlling the formation of pentagons and heptagons is a crucial factor in the growth of carbon nanotubes. A final branch in the variations of tube morphologies concerns the semi-toroidal tube ends. This growth is characterized by the coupling of a pentagon and a heptagon. Insertion of the pentagon-heptaagon (5-7) pair into a hexagon network does not affect the sheet at all topologically. To realize this growth

process, first a set of six heptagons is formed on a periphery of the open-tube (i). The circular brim then expands in the directions indicated by arrows. Solid circles represent locations of the heptagons. In the next step, a set of six pentagons is formed on the periphery of the brim, which makes the brim turn around by 180°, as illustrated in (j). An alternative structure is shown in (k), in which a slightly thicker tube is extended in the original tube direction, yielding a structure which has actually not yet been observed. Finally, it should be emphasized that an open-end tube can choose various passes or their combinations. One example is shown in (l), in which the first shell grows as a normal tube but the second tube follows a semi-toroidal tube end.

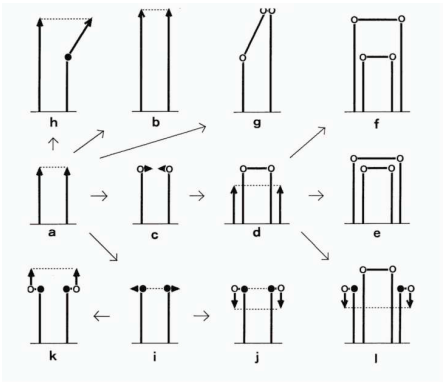

Fig. 36. Model for the open-end growth of the nanotube. (**a**) The tube ends are open while growing by accumulating carbon atoms at the tube peripheries in the carbon arc. Once the tube is closed, there will be no more growth on that tube but new tube shells start to grow on the side-walls. (**b**) Schematic representation of a kink-site on the tube end periphery. Supplying two carbon atoms (○) to it, the kink advances and thus the tube grows. But the supply of one carbon atom results in a pentagon which transforms the tube to a cone shape. (**c**) Evolution of carbon nanotube terminations based on the open-end tube growth. Arrows represent passes for the evolution. Arrow heads represents terminations of the tubes and also growth directions. Open and solid circles represents locations of pentagons and heptagons, respectively [225] (see text)

An electric field ($\sim 10^8\,\mathrm{V\ cm^{-1}}$) was also suggested as being the cause for the stability of open ended nanotubes during the arc discharge [223]. Because of the high temperature of the particles in the plasma of the arc discharge, many of the species in the gas phase are expected to be charged, thereby screening the electrodes. Thus the potential energy drop associated with the electrodes is expected to occur over a distance of 1 μm or less, causing very high electric fields. Later experiments and simulations confirmed that the electric field is in fact neither a necessary nor a sufficient condition for the growth of carbon nanotubes [226, 227]. Electric fields at nanotube tips

have been found to be inadequate in magnitude to stabilize the open ends of tubes, even in small diameter nanotubes (for larger tubes, the field effect drops drastically).

5.3 "Lip-lip" Interaction Model for Multi-Walled Nanotube Growth

Additional carbon atoms (spot-weld), bridging the dangling bonds between shells of a multilayered structure, have also been proposed for the stabilization of the open growing edge of multishell tubes [33]. For multiwall species, it is quite likely that the presence of the outer walls should stabilize the innermost wall, keeping it open for continued growth. Static *tight-binding* calculations performed on multilayered structures where the growing edge is stabilized by bridging carbon adatoms, show that such a mechanism could prolong the lifetime of the open structure [33].

Quantum molecular dynamics simulations were also performed to understand the growth process of multi-walled carbon nanotubes [228,229]. Within such calculations, the topmost atoms (dangling bonds) of the inner and outer edges of a bilayer tube rapidly move towards each other, forming several bonds to bridge the gap between the adjacent edges, thus verifying the assumption that atomic bridges could keep the growing edge of a nanotube open without the need of "spot-weld" adatoms (Fig. 37). At about 3000 K (a typical experimental growth temperature), the "lip-lip" interactions stabilize the open-ended bilayer structure and inhibit the spontaneous dome closure of the inner tube as observed in the simulations of single-shell tubes. These calculations also show that this end geometry is highly active chemically, and easily accommodates incoming carbon clusters, supporting a model of growth by chemisorption from the vapor phase.

In the "lip-lip" interaction model, the strong covalent bonds which connect the exposed edges of adjacent walls are also found to be highly favorable energetically within ab initio static calculations [230]. In the latter work, the open-ended growth is stabilized by the 'lip-lip" interactions, involving rearrangement of the carbon bonds, leading to significant changes in the growing edge morphology. However, using classical three-body potentials, the role of the "lip-lip" interactions is suggested to be relegated to facilitate tube closure by mediating the transfer of atoms between the inner and outer shells [231].

Successful synthesis of multi-wall nanotubes raises the question why the growth of such tubular structures often prevail over their more stable spherical fullerene counterpart [230]. It is furthermore intriguing that these nanotubes are very long, largely defect-free, and (unless grown in the presence of a metal catalyst) always have multiple walls. The "lip-lip" model explains that the sustained growth of defect-free multi-wall carbon nanotubes is closely linked to efficiently preventing the formation of pentagon defects which would cause a premature dome closure. The fluctuating dangling bond network present at the nanotube growing edge will also help topological defects to heal

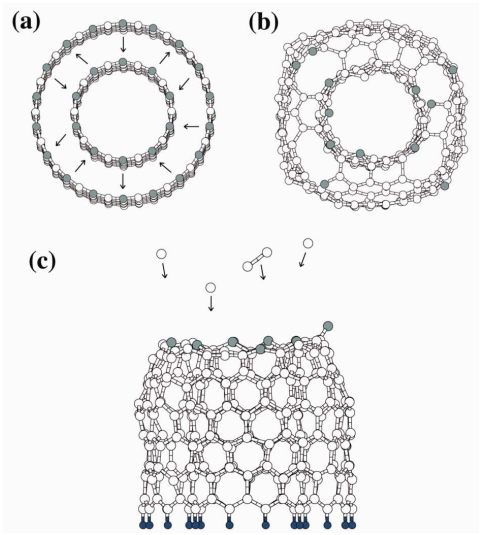

Fig. 37. Creation (**a**) and stabilization (**b**) of a double-walled (10,0)@(18,0) nanotube open edge by "lip-lip" interactions at ∼3000 K. The notation (10,0)@(18,0) means that a (10,0) nanotube is contained within an (18,0) nanotube. The direct incorporation (**c**) of extra single carbon atoms and a dimer with thermal velocity into the fluctuating network of the growing edge of the nanotube is also illustrated [228, 229]. The present system contains 336 carbon atoms (large white spheres) and 28 hydrogen atoms (small dark grey spheres) used to passivate the dangling bonds on one side of the cluster (bottom). The other low coordinated carbon atoms (dangling bonds) are represented as light grey spheres on the top of the structure

out, yielding tubes with low defect concentrations. With nonzero probability, two pentagon defects will eventually occur simultaneously at the growing edge of two adjacent walls, initiating a double-dome closure. As this probability is rather low, carbon nanotubes tend to grow long, reaching length to diameter rations on the order of $10^3 - 10^4$.

Semi-toroidal end shapes for multi-wall nanotubes are sometimes observed experimentally [225, 232]. The tube, shown in Fig. 38a does not have a simple double sheet structure, but rather consists of six semi-toroidal shells. The lattice images turn around at the end of the tube, so that an even number of lattice fringes is always observed. Another example is shown in Fig. 35b, in which some of the inner tubes are capped with a common carbon tip structure, but outer shells form semi-toroidal terminations. Such a semi-toroidal termination is extremely informative and supports the model of growth by "lip-lip" interactions for multi-wall nanotubes.

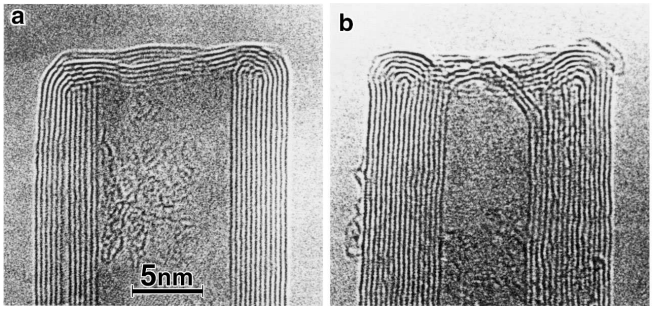

Fig. 38. Transmission electron micrographs of the semi-toroidal termination of multi-wall tubes, which consists of six graphitic shells (**a**). A similar semi-toroidal termination, where three inside tube shells are capped (**b**) [225]

5.4 Is Uncatalyzed Growth Possible for Single-Wall Nanotubes ?

The growth of single-shell nanotubes, which have a narrow diameter distribution (0.7–2 nm), differs from that of multishell tubes insofar as catalysts are necessary for their formation. This experimental fact is consequently an indirect proof of the existence of covalent lip-lip interactions which are postulated to be indispensable in a *pure carbon atmosphere* and imply that all nanotubes should have multiple walls. Single-wall tubes with unsaturated carbon dangling bonds at the growing edge are prone to be etched away in the aggressive atmosphere that is operative under typical synthesis conditions, which again explains the absence of single wall tubes in a pure carbon environment.

There have been several works based on classical, semi-empirical and quantum molecular dynamics simulations attempting to understand the growth process of single-shell tubes [228, 229, 233–235]. Most importantly, these studies have tried to look at the critical factors that determine the kinetics of open-ended tube growth, as well as studies that determine the relative stability of local-energy minimum structures that contain six-, five-, and seven-membered carbon rings in the lattice. Classical molecular dynamics simulations show that wide tubes which are initially open can continue to grow straight and maintain an all-hexagonal structure [234, 235]. However, tubes narrower than a critical diameter, estimated to be about ~ 3 nm, readily nucleate curved, pentagonal structures that lead to tube closure with further addition of carbon atoms, thus inhibiting further growth. Continued carbon deposition on the top of a closed tube yields a highly disordered cap structure, where only a finite number of carbon atoms can be incorporated, implying that uncatalyzed defect-free growth cannot occur on single-shell tubes.

First-principles molecular dynamics simulations [228] show that the open end of single-walled nanotubes closes spontaneously, at experimental tem-

peratures (2000 K–3000 K), into a graphitic dome with no residual dangling bonds (see Fig. 39). Similar self-closing processes should also occur for other nanotubes in the same diameter range, as is the case for most single-wall nanotubes synthesized so far. The reactivity of closed nanotube tips was also found to be considerably reduced compared to that of open end nanotubes. It is therefore unlikely that single-walled nanotubes could grow by sustained incorporation of C atoms on the closed hemifullerene-like tip. This is in agreement with the theoretical finding that C atoms are not incorporated into C_{60} [236].

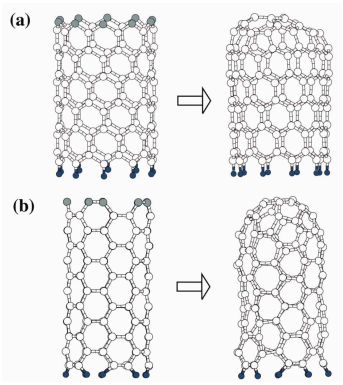

Fig. 39. Spontaneous closure of two single-walled nanotubes: (**a**) (10,0) zigzag tube and (**b**) (5,5) armchair tube. Both nanotubes have a fully reconstructed closed-end configuration with no residual dangling bonds [228, 229]. The present systems contains 120 carbon atoms (large white spheres) and 10 hydrogen atoms (small dark grey spheres) used to passivate the dangling bonds on one side of the two clusters (bottom). The other low coordinated carbon atoms (dangling bonds) are represented as light grey spheres on the top of the structure.

5.5 Catalytic Growth Mechanisms for Single-Wall Nanotubes

All these classical and quantum simulations, described above, may explain why single-wall nanotubes do not grow in the absence of transition metal catalysts. However, the role played by these metal atoms in determining the growth has been inaccessible to direct observation and is therefore a highly debated issue. Plausible suggestions include metal atoms initially decorating the dangling bonds of an open fullerene cluster, thus preventing it from closing.

One of the first assumption proposed in the literature [34] was that, in high temperature routes, one or a few metal atoms sit at the open end of a precursor fullerene cluster, which will be determining the uniform diameter of the tubes (the optimum diameter being determined by the competition

between the strain energy due to curvature of the graphene sheet and the dangling bond energy of the open edge. The role of the metal catalyst is to prevent carbon pentagons from forming by "scooting" around the growing edge (see Fig. 40).

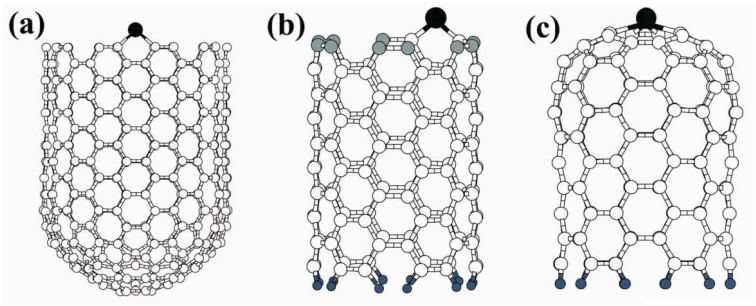

Fig. 40. (**a**) View of a (10,10) armchair nanotube (white ball-and-stick atomic structure) with a Ni (or Co) atom (large black sphere) chemisorbed onto the open edge [34]. The metal catalyst keeps the tube open by "scooting" around the open edge, insuring that any pentagons or other high energy local structures are rearranged to hexagons. The tube shown has 310 C atoms. (**b**) Catalytic growth of a (6,6) armchair single-walled nanotube. The metal catalyst atom cannot prevent the formation of pentagons, leading to tube closure (**c**) at experimental temperatures (1500 K) [203]. The present systems contains 1 cobalt atom (large black sphere), 120 carbon atoms (white spheres) and 12 hydrogen atoms (small dark grey spheres) used to passivate the dangling bonds on one side of the two clusters (bottom). The other low coordinated carbon atoms (dangling bonds) are represented as light grey spheres on the top of the structure (left)

Static ab initio calculations have investigated this scooter model and have shown that a Co or Ni atom is strongly bound but still very mobile at the growing edge [237]. However, the metal atom locally inhibits the formation of pentagons that would initiate dome closure. In addition, in a concerted exchange mechanism, the metal catalyst assists incoming carbon atoms in the formation of carbon hexagons, thus increasing the tube length. With a non-vanishing concentration of metal atoms in the atmosphere, several catalyst atoms will eventually aggregate at the tube edge, where they will coalesce. The adsorption energy per metal atom is found to decrease with increasing size of the adsorbed cluster [237]. The ability of metal clusters to anneal defects is thus expected to decrease with their increasing size, since they will gradually become unreactive and less mobile. Eventually, when the size of the metal cluster reaches some critical size (related to the diameter of the nanotube), the adsorption energy of the cluster will decrease to such a level that it will peel off from the edge. In the absence of the catalyst at the tube edge, defects can no longer be annealed efficiently, thus initiating tube closure.

This mechanism was consistent with first experimental observations that no "observable" metal particles are left were detected on the grown tubes [34]. Although the scooter model was initially investigated using static ab initio calculations [237], first-principles molecular dynamics simulations were also performed [203] in order to study the growth of single-wall tubes within a scheme where crucial dynamical effects are explored by allowing the system to evolve free of constraints at the experimental temperature (Fig. 40b). Within such a simulation at 1500 K, the metal catalyst atom is found to help the open end of the single-shell tube close into a graphitic network which incorporates the catalyst atom (see Fig. 40c). However, the cobalt-carbon chemical bonds are frequently breaking and reforming at experimental temperatures, providing the necessary pathway for carbon incorporation, leading to a closed-end catalytic growth mechanism.

This model, where the Co or Ni catalyst keeps a high degree of chemical activity on the nanotube growth edge, clearly differs from the uncatalyzed growth mechanism of a single-wall nanotube discussed above, which instantaneously closes into an chemically-inert carbon dome. The model, depicted in Fig. 40b, supports the growth by chemisorption from the vapor phase, according to the so-called vapour-liquid-solid (VLS) model, as proposed long ago for carbon filaments by Baker [82,85], Oberlin et al. [5], and Tibbetts [80].

Although the VLS model is initially a macroscopic model based on the fluid nature of the metal particle which helps to dissolve carbon from the vapor phase and to precipitate carbon on the walls, the catalytic growth model for the single-wall nanotubes considered here can be seen as its analogue, with the only difference being that the catalytic particle is reduced to one or a few metal atoms. In terms of this analogy, the quantum aspects of a few metal atoms at the growing edge of the single-shell tube has to be taken into account. In the catalytic growth of single-shell nanotubes, it is no longer the "fluid nature" of the metal cluster (VLS model), but the chemical interactions between the Co or Ni $3d$ electrons and the π carbon electrons, that makes possible a rapid incorporation of carbon atoms from the plasma. The cobalt $3d$ states increase the DOS near the Fermi level, thus enhancing the chemical reactivity of the Co-rich nanotube tip [203].

The observation of SWNTs produced in CCVD by preformed catalytic particles [125], which are encapsulated at the tip (Fig. 28) and thus are closely correlated with the tube diameter size (from 1 to 5 nm), demonstrates the validity of the VLS model on a nanometer scale, as already described in Sect. 4, Fig. 30. Such configurations are not found for high temperature routes, since actual observations show that nanotubes have grown from particles with no correlation between particle size and tube diameter. Since tube tips, especially for long tubes, cannot be easily observed, it cannot be excluded that the growth could also proceed from a very small particle located at the tip as in the CCVD situation. Precisely because of the enhancement of the chemical activity due to the presence of metal catalyst particles at the

experimental growth temperature, the Co–C bonds are frequently reopened and the excess of cobalt could be ejected from the nanotube tip, making its observation impossible.

The presence of any remaining metal catalyst atoms at the free nanotube tip in high temperature routes (even in very small undetectable amounts) can therefore not be excluded. The presence of such ultra-small catalyst particles, which is certainly not easy to establish experimentally, should strongly influence the field emission properties of these single-shell tubes [238] and could explain some field emission patterns observed at the nanotube tip. Magnetic susceptibility measurements and magnetic STM could be used to investigate the presence of metal catalysts at the nanotube tip, as such experimental techniques are sensitive to tiny amounts of magnetic transition metals. At this stage, a better experimental characterization method for the atomic structure of single-walled nanotube tips is required.

5.6 Root Growth Mechanism for Single-Wall Nanotubes

We now turn to the phenomenological model, presented in Sect. 4, Fig. 32, which accounts for the situation obseved in high temperature routes where nanotubes are found to nucleate from large particles and to grow from the root. We briefly summarized this model. Carbon and metal atoms, issued from the vaporization of the target, condense and form alloy particles. As these particles are cooled, carbon atoms, dissolved in the particle, segregate onto the surface, because the solubility of the surface decreases with decreasing temperature. As the system is cooled, soot is formed. The sizes of the soot particles are several tens of nm wide, and are identified by TEM observations as embedded metal clusters surrounded by a coating of a few graphitic layers. Some singularities at the surface structure or atomic compositions may catalyze the formation of single-wall tubes, thereby providing another mechanism for the growth of single-wall carbon nanotubes. After the formation of the tube nuclei, carbon is supplied from the core of the particle to the root of the tubes, which grow longer maintaining hollow capped tips. Addition of carbon atoms (or dimers) from the gas phase at the tube tips (opposite side) also probably helps the growth.

Many single-shell nanotubes are observed to coexist with catalytic particles and often appear to be sticking out of the particle surfaces. One end of the tubule is thus free, the other one being embedded in the particle, which often has a size exceeding the nanotube diameter by well over one order of magnitude.

Classical molecular-dynamics simulations [201] reveal a possible atomistic picture for this root growth mode for single-wall tubes. According to the model, carbon atoms precipitate from the metal particle, migrate to the tube base, and are incorporated into the nanotube network, thereby leading to defect-free growth. More recent classical molecular dynamics calculations, using empirical potentials for C–C bonds [239, 240] aim at simulating the

nucleation step in order to show how carbon atoms segregate at the surface of the metallic particle and self-organize to built a nanotube nucleus.

To go beyond this classical approach, the metal-carbon segregation process was investigated at the atomic level using quantum molecular dynamics [202, 204]. A 153 atom mixed Co–C cluster was created by extracting a sphere 1.3 nm in diameter from a hexagonal close-packed (HCP) Co structure, and by replacing randomly 2/3 of the Co atoms by C atoms (Fig. 41). The mixed cluster was then heated up to 2000K. After a thermalisation period of 5ps at 2000K (Fig. 41a), the temperature was gradually decreased to 1500K using a thermal gradient of 100 K/ps. After 5ps at 1500K, most of the C atoms (about 80%) segregate to the surface of the cluster, while the Co atoms migrate to its center (Fig. 41b). The C atoms at the surface move very quickly and form a network composed of connected linear chains and some aromatic rings. The creation of an hexagon connected with two pentagons is remarkable (Fig. 41c) and can be considered as a first stage of the nucleation process. The theoretical investigation of the nucleation pathway for single-wall nanotubes on a metal surface has recently been studied by a series of ab initio total energy calculations [209]. Incorporation of pentagons at an early stage of nucleation was found to be energetically favorable as they reduce the number of dangling bonds and facilitate curvature of the structure and bonding to the metal. In addition, the nucleation of a closed cap or a capped SWNT at the metal surface is overwhelmingly favored compared to any structure with dangling bonds or to fullerenes.

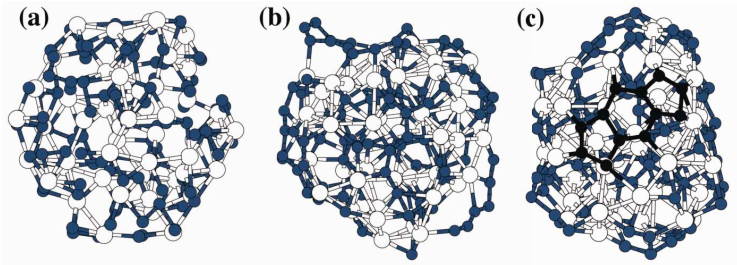

Fig. 41. Segregation process in a cluster containing 51 Co atoms (big white spheres) and 102 C atoms (small gray spheres) when the temperature drops from 2000K to 1500K. (a) The cluster is first heated up to 2000K, leading to random positions of Co and C within the sphere volume. (b) The temperature is gradually decreased to 1500K. C atoms segregate to the surface while Co atoms migrate to the center. (c) Carbon linear chains and aromatic rings (in black) are created at the surface of the cluster. Total simulation time: 25ps.

When the nucleation has started, modeling the migration of carbon atoms at the surface of a catalyst particle and their incorporation to the SWNT base have also been performed using quantum molecular dynamics [202, 204].

Figure 8 represents a SWNT closed at one end by half a C_{60} molecule while the reactive open part is deposited on a double layer of HCP cobalt, satisfying most of the dangling bonds (Fig. 42a). Twenty carbon atoms have been added at the surface of the metal particle in order to observe a migration process to the root of the nanotube. The global system is then heated up to 1500 K. After 15ps of simulation, 5 carbon atoms had diffused to the tube base and were incorporated in the nanotube body (Fig. 42b). Even if the time scale of such simulations prevents us from studying the further evolution of the root growth, this incorporation as well as the absence of formation of a closed fullerene-like molecule suggest that this root growth mechanism is a good candidate to explain the emergence of carbon nanotubes from large metal catalyst particle. Our QMD simulation shows that the role of the catalyst is not only to stabilize the forming tube, but also to provide fluctuating Co–C bonds in the middle of which new carbon atoms are easily incorporated.

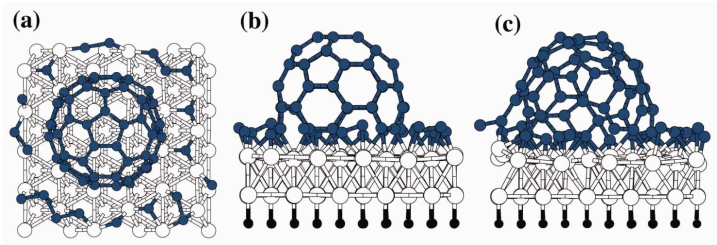

Fig. 42. Root growth mechanism for SWNTs extruded from large catalytic nanoparticles. A small (6,6) nanotube portion capped by a perfect fullerene-like hemisphere is placed on a slab of HCP Co, with 20 additional isolated carbon atoms on the particle surface. The model contains 74 carbon atoms (small gray spheres), 59 cobalt atom (big white sphere), and 30 hydrogen atoms (small black spheres at the bottom) terminating the metal particle in order to satisfy the dangling bonds. Hydrogen atoms and the last layer of Co are kept fixed during the simulation. Top (**a**) and side (**b**) views of the starting configuration at 0K. (**c**) Incorporation in the honeycomb network of the nanotube root of 5 extra carbon atoms which have diffused on the nanoparticle surface at 1500K. Total simulation time : 15ps

In summary, we have provided experimental and theoretical arguments in favour of a root growth mechanism for single wall nanotubes. Since the QMD simulations are extremely time and memory consuming, such technique cannot really be used in a systematic manner to increase the length and time scales and to vary relevant parameters. Simplified models using tight-binding potentials are currently under development to undertake appropriate large scale simulations [204, 241]

5.7 Conclusion

Since their discovery in 1991, great progress has been made in the understanding of carbon nanotube growth. There has been a constant fruitful interplay between theoretical calculations and experimental measurements which has enhanced our insight into the formation processes of these ultimate carbon fibers.

Several mechanisms, as described above, have been proposed to account for the growth mechanisms of single-wall and multi-wall carbon nanotubes with or without the presence of any catalyst. The key role played by the metal catalyst is crucial for understanding the growth of single-shell tubes at the microscopic level. However, the actual role of the metal or alloy is not yet completely solved, although experimental observations and numerical simulations converge to plausible scenarii depending on the synthesis route. Ab initio calculations have been very successful and helpful to simulate and to understand different processes. They are however inadequate to simulate the whole nucleation process. Empirical methods appear to be relatively suited for simulating the growth but fail to describe the nucleation. At the present stage, semi-empirical simulations are the most promising ones.

Probably the most intriguing problem is to understand the microscopic mechanism and optimum conditions for the formation of well-designed single-wall nanotubes. Although it has been argued that the armchair nanotube structure is favored energetically [34], experimental conditions under which these tubules would be grown with good control are still not yet well known. Nonetheless, as more experimental data become available to correlate the atomic structure and the synthesis conditions, and more is known about the growth at the atomic level, it is hoped that controlled growth of single-walled carbon nanotubes with designed structures will be achieved soon. In addition, with further experimental confirmation of their unique properties, there will be a great incentive to develop industrial-scale production methods.

6 $B_xC_yN_z$ Composite Nanotubes

We now turn to the case of composite $B_xC_yN_z$ nanotubes. As compared to the carbon case, there has been much less work devoted to understanding at the microscopic level their growth mechanisms. An additional complexity is added by the presence of several atomic species and the related "chemical frustrations". Further, while good empirical or tight-binding parameters exist for carbon, the problem of charge transfer between species render the use of empirical approachs more difficult.

6.1 $B_xC_yN_z$ Nanotubes

While the experimental techniques developed for their synthesis have been described in Sect. 1, it is important to recall here briefly that such synthesis

approaches can be divided into two families: the high-temperature techniques, including arc discharge [65–68] and laser ablation [69] and the medium-temperature ones, such as CVD [242,243] or thermal decomposition of molecular precursors [244,245]. In addition to these synthesis routes, a substitution reaction on preformed carbon nanotubes has been proposed [246–248].

The importance of synthesis temperature becomes even more crucial in the case of composite $B_xC_yN_z$ nanotubes because of the tendency towards segregation into pure carbon or BN domains. Such a segregation is driven by thermodynamics as it has been shown indeed that B–N and C–C bonds are more stable than C–N or C–B ones [249, 250]. We note however that the segregation in domains means the diffusion of atoms during the growth process (we assume here that the source of B, C and N atoms is rather uniform). As a result, the topology of synthesized $B_xC_yN_z$ nanotubes will depend on the competition between thermodynamics and kinetics.

At low temperature, the growth is kinetically driven and the diffusion is limited. The systems obtained are relatively homogeneous at a few bond length scale. This can be inferred from the electronic properties of $B_xC_yN_z$ systems synthesized by CVD or substitution reactions which appear to be photoluminescent with a band gap ranging between 1- 3 eV [243, 251, 252]. The analysis of the electronic properties (see Chap. 4) shows that such band gaps can only be explained in the limit of very homogeneous systems.

At high temperature, thermodynamics is the main factor and one observe systems with segregated pure BN or carbon domains. The segregation can take place either within a single tube wall, leading to the formation of dots or metal/insulator C/BN junctions [253], or the segregation can be complete, namely one observe, in the case of MWs systems, pure carbon tubes concentric with pure BN tubes [68, 248].

6.2 B-Doped Nanotubes

The limiting case of B-doped nanotubes, with a boron content equivalent to 1 % in the body, is quite surprising. It has been shown that B-doped nanotubes synthesized by arc-discharge tend to be much longer than their pure cabon analog [66, 254]. Further, they exhibit an improved crystallinity and seem to be *s*elected towards the zigzag helicity [255].

Such an increase in nanotube length has been explained on the basis of ab initio [255] and tight-binding [256] total energy and molecular-dynamics simulations. It has been shown that in the case of zig-zag tubes, boron atoms can behave as surfactant during the open-end growth of the nanotubes. One therefore can explain that a small amount of B atoms can greatly influence the growth process. The presence of B atoms on the tube lips was further shown to reduce the probability of final closure of the tubes onto closed caps. Indeed, as a charge transfer from B to C destabilizes any B–B bonding by electrostatic repulsion, such disfavored bonds were seen to re-open sponta-

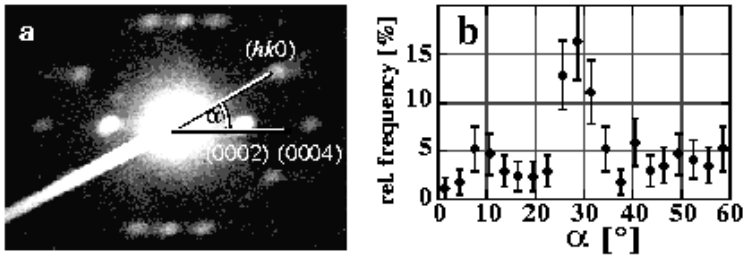

Fig. 43. (Left) Electron diffraction pattern of a B-doped tube (Right)Statistical analysis of the angular distribution of the *hk0* reflections. The value $\alpha = 30\,\mathrm{deg}$ corresponds to the zigzag geometry [255]

neously at synthesis temperature (1500-2000 K). Such retarded closure can be invoked to explain the exceptional length of B-doped tubes.

The surfactant mechanism could only be evidenced for zigzag tubes. For armchair geometries, B atoms tend to sink into the carbon tube body. This observation provides some understanding on why the long B-doped nanotubes were observed to be mainly of the zigzag type. Such an helicity selection proposes a first route towards the synthesis of carbon nanotubes with well-defined geometrical, and thus electronic, properties.

Concerning the body of the tube, total energy calculations [250] and STS experiments [257] tend to favor the model of segregated islands of pure BC_3-like domains. Ab initio DFT simulations show that B atoms can gain as much as $0.5\,\mathrm{eV/atom}$ by segregating. Again, the existence of segregation in B-doped systems should strongly depend on the synthesis conditions.

6.3 BN Tubes

We close this review on the growth mechanisms of nanotubes by the important case of pure BN systems. There are several specific features in the topology of BN tubes that differ significantly from the carbon case. A puzzling observation is that BN nanotubes tend to have a reduced number of layers. This was evidenced in the case of uncatalyzed arc-discharge growth techniques with the presence of a large number of bi-layer and even mono-layer nanotubes [57,58]. Further, single-wall BN tubes have been grown with "catalyst-free" CVD [258] and laser ablation [64] techniques. The absence of metal catalyst does not rule out however some catalytic effect. It has been suggested [64] that the liquid boron droplets observed in laser assisted growth may play the role of the metallic droplet in the root-mechanism growth of SW nanotubes (see Fig. 44). Further, the role of Hf or Ta in early arc discharge experiments (used to render the electrode conductive) is still unclear [57,58].

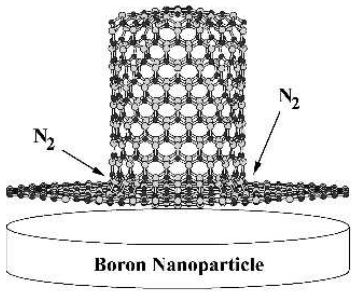

Fig. 44. Symbolic representation of a root-growth mechanism assisted by B-droplets [64]

Another intriguing observation is the selection of chirality towards the zigzag geometry observed for laser-ablation grown single-wall BN tubes [64]. On the basis of ab initio MD simulations [259], the importance of maintaining a local 1/1 BN stoichiometry was emphasized as local unbalance would lead to amorphous system. In particular, in the case of open-end growth, pure boron (or N) lips present in the case of zigzag tubes was shown to lead to amorphization, supporting the idea that the growth of SW zigzag BN tubes reported in Ref. [64] is based on a root-growth approach.

We note finally that the cost associated with the formation of homopolar B–B or N–N bonds leads to the formation of rather flat BN tips, a fact that can be explained by the presence of squares in the final cap of the tube [57, 58, 258–260].

References

1. H.W. Kroto, J.R. Heath, S.C. O'Brien, R.F. Curl, and R.E. Smalley: Nature **318**, 216 (1985)
2. W. Krätschmer, L.D. Lamb, K. Fostiropoulos, and D.R. Huffman: Nature **347**, 354 (1990)
3. S. Iijima: Nature **354**, 56 (1991)
4. R. Bacon: Appl. Phys. Lett. **31**, 283 (1960)
5. A. Oberlin, M. Endo, T. Koyama: J. Cryst. Growth **32**, 335 (1976)
6. S. Farhat, I. Hinkov, and C.D. Scott: Journal Nanosci. Nanotech. **4**, 377 (2004)
7. H. Lange, K. Saidane, M. Razafinimanana and A. Gleizes: J. Phys. D: Appl. Phys. **32**, 1024 (1999)
8. T.W. Ebbesen and P.M. Ajayan: Nature **358**, 220 (1992)
9. T.W. Ebbesen: Annu. Rev. Mater. Sci. **24**, 235 (1994)
10. S. Iijima and T. Ichihashi: Nature **363**, 603 (1993)
11. W.K. Maser, P. Bernier, J. M. Lambert, O. Stephan, P.M. Ajayan, C. Colliex, V. Brotons, J.M. Planeix, B. Coq, P. Molinié, and S. Lefrant: Synth. Met. **81**, 243 (1996)

12. C.H. Kiang, W.A. Goddard III, R. Beyers, and D.S. Bethune: Carbon **33**, 903 (1995)
13. P.M. Ajayan J.M. Lambert, P. Bernier, L. Barbedette, C. Colliex, and J.M. Planeix: Chem. Phys. Lett. 215, 509 (1993)
14. J.M. Lambert, P.M. Ajayan, and P. Bernier: Synth. Met. **70**, 1475 (1995)
15. C.H. Kiang, W.A. Goddard III, R. Beyers, J.R. Salem, and D.S. Bethune: J. Phys. Chem. **98**, 6612 (1994)
16. D.S. Bethune, C.H. Kiang, M.S. de Vries, G. Gorman, R. Savoy, and J. Vazquez, R. Beyers: Nature **363**, 605 (1993)
17. S. Seraphin: In: *Proceedings of the Symposium on "Recent Advances in the Chemistry and Physics of Fullerenes and Related Materials"* ed by K.M. Kadish and R.S. Ruoff (The Electrochemical Society Inc .1994)
18. S. Seraphin and D. Zhou: Appl. Phys. Lett. **64**, 2087 (1994)
19. J.M. Lambert, P.M. Ajayan, P. Bernier, J.M. Planeix, V. Brotons, B. Coq, and J. Castaing: Chem. Phys. Lett. **226**, 364 (1994)
20. C. Journet, W.K. Maser, P. Bernier, A. Loiseau, M. Lamy de la Chapelle, S. Lefrant, P. Deniard, R. Lee, and J. E. Fischer: Nature **388**, 756 (1997)
21. X. Lin, K. Wang, V.P. Dravid, R.P.H. Chang, and J.B. Ketterson: Phys. Lett. **64**, 181 (1994)
22. P.M. Ajayan, C. Colliex, J. M. Lambert, P. Bernier, L. Barbedette, M. Tence, and O. Stephan: Phys. Rev. Lett. **72**, 1722 (1994)
23. S. Seraphin, D. Zhou, J. Jiao, M.A.Minke, S.Wang, T. Yadav, and J.C.Withers: Chem. Phys. Lett. **217**, 191 (1994)
24. Y. Saito, K. Kawabata, and M. Okuda: J. Phys. Chem. **99**, 16076 (1995)
25. A. Loiseau and H. Pascard: Chem. Phys. Lett. **256**, 246 (1996)
26. C. Guerret-Piécourt, Y. Le Bouar, A. Loiseau, and H. Pascard: Nature **372**, 761 (1994)
27. M. Ata, A.J. Hudson, K. Yamaura, and K. Kurihara: J. Appl. Phys. **4207** (1995)
28. C.H. Kiang, W.A. Goddard III, R. Beyers, J.R. Salem, and D.S. Bethune: J. Phys. Chem. Solids **57**, 35 (1996)
29. S. Subramoney, R.S. Ruoff, D.C. Lorents, and R. Malhotra: Nature **366**, 637 (1993)
30. X. Zhao, M. Ohkohchi, M. Wang, S. Iijima, T. Ichihashi, and Y. Ando: Carbon **35**, 775 (1997)
31. L.P.F. Chibante, A. Thess, J.M. Alford, M.D. Diener, and R.E. Smalley: J. Phys. Chem. **97**, 8696 (1993)
32. – SES Research, www.sesres.com
    – Nanocarblab (NCL) , www.nanocarblab.com
    – Nanoledge, www.nanoledge.com
    – Materials and Electrochemical Research (MER , www.opus1.com/ mercorp
    – Carbon Solutions, www.carbonsolution.com
33. T. Guo, P. Nikolaev, A. G. Rinzler, D. Tomanek, D.T. Colbert, and R. E. Smalley: J. Phys. Chem. **99**, 10694 (1995)
34. A. Thess, R. Lee, P. Nikolaev, H. Dai, P. Petit, J. Robert, C. Xu, Y. Hee, S.G. Kim, A.G. Rinzler, D.T. Colbert, G.E. Scuseria, D. Tomnek, J.E. Fischer, and R. Smalley: Science **273**, 483 (1996)

35. W.K. Maser, E. Munoz, R.E. Smalley, A.M. Benito, M.T. Martinez, G.F. de la Fuente, Y. Maniette, E. Anglaret, and J.-L. Sauvajol: Chem. Phys. Lett. **292**, 587 (1998) ; E. Munoz, W. Maser, A.M. Benito, M.T. Martinez, G.F. de la Fuente, A. Righi, J.-L. Sauvajol, E. Anglaret, and Y. Maniette: Appl. Phys. A **70**, 145 (2000)
36. S. Bandow, A. Asaka, Y. Saito, A.M. Rao, L. Grigorian, E. Richter, and P.C. Ecklund: Phys. Rev. Lett. **80**, 3779 (1998)
37. T. Ishigaki, S. Suzuki, H. Kataura, W. Krtschmer, and Y. Achiba: Appl. Phys. A **70**, 121 (2000)
38. A. Foutel-Richard: PhD thesis, Conservatoire National des Arts et Métiers, Paris (2003)
39. N. Dorval, A. Foutel-Richard, M. Cau, A.Loiseau, B. Attal-Trtout, J.L. Cochon, D. Pigache, P. Bouchardy, V. Krger, and K.P. Geigle: J. Nanosc. and Nanotech. **4**, 450 (2004)
40. M. Castignolles, A. Foutel-Richard, A. Mavel, J.-L. Cochon, D. Pigache, A. Loiseau, and P. Bernier: In *Electronic Properties of Novel Materials Science and Technology of Molecular Nanostructures* ed by H. Kuzmany, J. Fink, M. Mehring, S. Roth, (American Institute of Physics, 2002), p 385
41. A.A. Puretzky, D.B. Geohegan, X. Fan, and S.J. Pennycook: Appl. Phys. Lett. **76**, 182, (2000); A.A. Puretzky, D.B. Geohegan, X. Fan, and S.J. Pennycook: Appl. Phys. A **70**, 153, (2000)
42. A.A. Puretzky, H. Schittenhelm, X. Fan, M.J. Lance, L.F. Allard, Jr., and D.B. Geohegan: Phys. Rev. B **65**, 245425 (2002)
43. S. Arepalli, P. Nikolaev, W. Holmes, and C.D. Scott: Appl. Phys. A. **70**, 125 (2000); C.D. Scott, S. Arepalli, P. Nikolaev, and R.E. Smalley: Appl. Phys. A **72**, 573 (2001)
44. F. Kokai, K. Takahashi, M. Yudasaka, R. Yamada, T. Ichihashi and S. Iijima: J. Phys. Chem. B **103**, 4346 (1999); F. Kokai, D. Kasuya, K. Takahashi, M. Yudasaka, and S. Iijima,: Appl. Phys. A **73**, 40(2001)
45. *Binary of phase alloys diagrams*, T.B. Massalski ed (ASM International,1990)
46. F. Kokai, K. Takahashi, M. Yudasaka, and S. Iijima: J. Phys.Chem. B **104**, 6777 (2000)
47. G. De Boer, S. Arepalli, W. Holmes, P. Nikolaev, C. Range, and C. Scott: J. Appl. Phys. **89**, 5760 (2001)
48. J.-L. Cochon, J. Gavillet, M. Lamy de la Chapelle, A. Loiseau, M. Ory, and D. Pigache: In *Electronic Properties of Novel Materials Science and Technology of Molecular Nanostructures* ed by H. Kuzmany, J. Fink, M. Mehring, S. Roth, (American Institute of Physics, 1999), p 237
49. L.P.F. Chibante, A. Thess, J. M. Alford, M.D. Diener, and R.E. Smalley: J. Phys. Chem. **97**, 8696 (1993)
50. C.L. Fields, J.R. Pitts, M.J. Hale, C. Bingham, A. Lewandowski, and D.E. King: J. Phys. Chem. **97**, 8701 (1993)
51. D. Laplaze, P. Bernier, L. Barbedette, J.-M. Lambert, G. Flamant, M. Lebrun, A. Brunelle, and S. Della-Negra. C. R. Acad. Sci. **318**, 733 (1994)
52. D. Laplaze, P. Bernier, W.K. Maser, G. Flamant, T. Guillard, and A. Loiseau: Carbon **36**, 685 (1998)

53. T. Guillard, S. Cetout, L. Alvarez, J.-L. Sauvajol, E. Anglaret, P. Bernier, G. Flamant, and D. Laplaze: Eur. Phys. J. B **5**, 251 (1999)
54. D. Laplaze , L. Alvarez , T. Guillard , J.M. Badie , and G. Flamant: Carbon **40**, 1621 (2002)
55. G. Flamant, D. Luxembourg, J.F. Robert, and D. Laplaze: Solar Energy **77**, 73 (2004)
56. N.G. Chopra, R.J. Luyken, K. Cherrey, V.H. Crespi, M.L. Cohen, S.G. Louie, and A. Zettl: Science **269**, 966 (1995)
57. A. Loiseau, H. Pascard, F. Willaime, N. Demoncy, and G. Hug, Phys. Rev. Lett. **76** 4737 (1996)
58. M. Terrones, W.K. Hsu, H. Terrones, J.P. Zhang , S. RamoSa, J.P. Hare, R. Castillo, K. Prassides, A.K. Cheetham, H.W. Kroto, and D.R.M. Walton: Chem. Phys. Lett, **259**, 568 (1996)
59. Y. Saito and M. Maida: J. of Phys. Chem A **103**, 10, 1291 (1999)
60. J. Cumings and A. Zettl: Chem. Phys. Let. **316**, 211 (2000)
61. D. Golberg, Y. Bando, M. Eremets, K. Takemura, K. Kurashima, and H. Yusa: Appl. Phys. Lett. **69**, 2045 (1996)
62. D.P. Yu, X.S. Sun, C.S. Lee, I. Bello, S T. Lee, H.D. Gu, K.M. Leung, G.W. Zhou, Z.F. Dong, and Z.Zhang: Appl. Phys. Lett. **72**, 1966 (1998)
63. G.W. Zhou, Z Zhang, Z.G. Bai, and D.P. Yu: Sol. St. Com. **109**, 555 (1999)
64. R.S. Lee, J. Gavillet, M. Lamy de la Chapelle, A. Loiseau, J.-L. Cochon, D. Pigache, J. Thibault, and F. Willaime: Phys. Rev. B **64**, 121405 (2001)
65. O. Stephan, P.M. Ajayan, C. Colliex, P. Redlich, J.M. Lambert, P. Bernier, and P. Lefin: Science **266**, 1683 (1994)
66. P. Redlich, J. Loeffler, P.M. Ajayan, J. Bill, F. Aldinger, and M. Ruhle: Chem. Phys. Lett. **260**, 465 (1996)
67. Z. Weng-Sieh, K. Cherrey, N.G. Chopra, X. Blase, Y. Miyamoto, A. Rubio, M.L. Cohen, S.G. Louie, A. Zettl, and R. Gronsky: Phys. Rev. B **51**, 11229 (1995)
68. K. Suenaga, C. Colliex, N. Demoncy, A. Loiseau, H. Pascard, and F. Willaime: Science **278**, 653 (1997)
69. Y. Zhang, H. Gu, K. Suenaga, S. Iijima: Chem. Phys. Lett. **279**, 264 (1997)
70. K. Suenaga, F. Willaime, A. Loiseau, and C. Colliex: Applied Phys. A **68**, 301 (1999)
71. R.T.K. Baker, P.S. Harris, The formation of filamentous carbon, In: *Chemistry and Physics of Carbon*, 14, ed by P.L.Walker Jr. and P.A.Thrower (Marcel Dekker, 1978) pp 83-165
72. K.P. De Jong and J.W. Geus: Catal. Rev.-Sci.Eng. **42**, 481 (2000)
73. N.M. Rodriguez: J.Mater.Res. **8**, 3233 (1993)
74. P.E. Nolan, D.C. Lynch, and A.H. Cutler: J. Phys. Chem. B **102**, 4165 (1998)
75. M. Pérez-Cabero, E. Romeo, C. Royo, A. Monzón, A. Guerrero-Ruíz, and I. Rodríguez-Ramos: J. Catal. **224**, 197 (2004)
76. J. Wei and E. Iglesia: J. Catal. **224**, 370 (2004)
77. I. Alstrup: J. Catal. **109**, 241 (1988)
78. I. Barin, Thermochemical data of pure substances, VCH (1989)

79. J.R. Rostrup-Nielsen: J. Catal. **27**, 343 (1972)
80. G.G. Tibbetts: J. Cryst. Growth **66**, 632 (1984)
81. P.K. De Bokx, A.J.H.M. Kock, E. Boellaard, W. Klop, and J.W. Geus: J. Catal. **96**, 454 (1985)
82. R.T.K. Baker, M.A. Barber, P.S. Harris, F.S. Feates, and R.J. Waite: J.Catal. **26**, 51 (1972)
83. R.T.K. Baker, P.S. Harris, R.B. Thomas, and R.J. Waite: J.Catal.**30**, 86 (1973)
84. R.T.K. Baker, Electron microscopy studies of the catalytic growth of carbon filaments, In: *Carbon Fibers Filaments and Composites*, ed by J.L.Figueiredo, C.A.Bernardo, R.T.K.Baker, and K.J.Hüttinger (Kluwer 1989) pp 405-440
85. R.T.K. Baker: Carbon **27**, 315 (1989)
86. A.V. Melechko, V.I. Merkolov, D.H. Lowndes, M.A. Guillorn, and M.L. Simpson: Chem. Phys. Lett. **356**, 527 (2002)
87. J.R. Rostrup-Nielsen, and D.L. Trim: J. Catal. **48**, 155 (1977)
88. M. Audier, and M. Coulon, L. Bonnetain: Carbon **21**, 105 (1983)
89. M. Audier and M. Coulon: Carbon **23**, 317 (1985)
90. J.-W. Snoeck, G. F. Froment, and M. Fowles: J. Catal. **169**, 240 (1997)
91. A. Sacco Jr, F.W.A.H. Geurts, G.A. Jablonski, S.Lee, and R.A. Gately: J. Catal. **119**, 322 (1989)
92. G.A. Jablonski, F.W.A.H. Geurts, A. Sacco Jr, and R.R. Biderman: Carbon **30**, 87 (1992)
93. J.P. Pinheiro and P. Gadelle: J.Phys.Chem.Solids **62**, 1015 (2001)
94. J.P. Pinheiro, P. Gadelle, C. Jeandey, and J.L. Oddou: J.Phys.Chem.Solids **62**, 1023 (2001)
95. J.P. Pinheiro, Croissance catalytique sous CO de carbone filamentaire et nanotubulaire, PhD thesis, Université Joseph Fourier (Grenoble1) (1999)
96. J.P. Pinheiro, S. Herreyre, and P. Gadelle, Carbon'97, 23rd biennial conference on carbon, Extended abstracts, 340-341
97. S. Amelinckx, X.B. Zhang, D. Bernaerts, X.F. Zhang, V. Ivanov, and J.B. Nagy: Science **265**, 635 (1994)
98. M. Audier, M. Coulon, and A. Oberlin: Carbon **18**, 73-76 (1980)
99. M. Audier, A. Oberlin, and M. Coulon: Journal of Crystal Growth **55**, 549 (1981)
100. H.E. Grenga, and K.R. Lawless: J. Appl. Phys. **43**, 1508 (1972)
101. R.T. Yang and J.P. Chen: J. Catal. **115**, 52-64 (1989)
102. V.I.Zaikovskii, V.V.Chesnokov, and R.A.Buyanov: Kinetics and Catalysis **42**, 813 (2001), (translated from Kinetika i Kataliz)
103. H. Terrones, T. Hayashi, M. Muoz-Navia, M. Terrones, Y.A. Kim, N. Grobert, R. Kamalakaran, J. Dorantes-Dvila, R. Escudero, M.S. Dresselhaus, and M. Enro: Chem. Phys. Lett. **343**, 241 (2001)
104. N.A. Kiselev, J.L. Hutchison, A.P. Moravsky, E.V. Rakova, E.V. Dreval, C.J.D. Hetherington, D.N. Zakharov, J. Sloan, and R.O. Loutfy: Carbon **42**, 149 (2004)
105. H. Murayama, T. Maeda: Nature **345**, 791 (1990)
106. N.M. Rodriguez, A. Chambers, R.T.K. Baker: Langmuir **11**, 3862 (1995)
107. P.L. Hansen, J.B. Wagner, S. Helveg, J.R. Rostrup-Nielsen, B.S. Clausen, H. Topsøe: Science **295**, 2053 (2002)

108. P.E. Nolan, M.J. Schabel, D.C. Lynch, A.H. Cutler: Carbon **33**, 79 (1995)
109. P. Pinheiro, M.C. Schouler, P. Gadelle, M. Mermoux, E. Dooryhée: Carbon **38**, 1469 (2000)
110. G.G. Tibbetts, M.P. Balogh: Carbon **37**, 241 (1999)
111. T. Koyama: Carbon **10**, 757 (1972)
112. F. Benissad, P. Gadelle, M. Coulon, L. Bonnetain: Carbon **26**, 425 (1988)
113. M. Endo, K. Takeuchi, K. Kobori, K. Takahashi , H.W. Kroto, A. Sarkar: Carbon **33**, 873 (1995)
114. Ph.Serp, J.L. Figueiredo: Carbon **34**, 1452 (1996)
115. Q.T. Le, M.C. Schouler, J. Garden, P. Gadelle: Carbon **37**, 505 (1999)
116. R.S. Wagner and W.C. Ellis: Appl. Phys. Lett. **4**, 89 (1964)
117. R.S. Wagner et W.C. Ellis: Trans. Met. Soc. AIME **233**, 1053 (1965)
118. V. Jourdain, H. Kanzow, M. Castignolles, A. Loiseau, P. Bernier: Chem. Phys. Lett. **364**, 27 (2002
119. W.Z. Li, J.G. Wen, Y. Tu, Z.F. Ren: Appl. Phys. A **73**, 259 (2001)
120. O.P. Krivoruchko, V.I. Zaikovski: Kinetics and Catalysis **39**, 561 (1998) (translated from Kinetika i Kataliz)
121. E.E. Kukovitsky, S.G. L'vov, N.A. Sainov, V.A. Shustov, L.A. Chernozatonskii: Chem. Phys. Lett. **355**, 497 (2002)
122. S. Helveg, C. López-Cartes, J. Sehested, P.L. Hansen, B.S. Clausen, J.R. Rostrup-Nielsen, F. Abild-Pedersen, J.K. Nørskov: Nature **427**, 426 (2004)
123. X. Chen, R. Wang, J. Xu, and D. Yu: Micron **35**, 455 (2004)
124. Y. Breton, R. Fleurier, J.-P. Salvetat, A.-L. Thomann, M. Verstraete, and J.-C. Charlier: App. Phys. Lett. **85**, 5376 (2004)
125. H. Dai, A.G. Rinzler, P. Nikolaev, A. Thess, D.T. Colbert, and R.E. Smalley: Chem. Phys. Lett. **260**, 471 (1996)
126. A.M. Cassell, J.A. Raymakers, J. Kong, and H. Dai: J. Phys. Chem. B **103**, 6484 (1999)
127. J.F. Colomer, G. Bister, I. Willems, Z. Konya, A. Fonseca, J.B. Nagy, and G. Van Tendeloo: Chem. Commun. (Cambridge), 1343 (1999)
128. J.H. , M.J. Bronikowski, B.R. Azamian, P. Nikolaev, A.G. Rinzler, D.T. Colbert, K. A. Smith, and R.E. Smalley: Chem. Phys. Lett. **296**, 195 (1998)
129. A.R. Harutyunyan, B.K. Pradhan, U.J. Kim, G. Chen, and P.C. Eklund: Nano Letters **2**, 525 (2002)
130. H.M. Cheng, F. Li, G. Su, H. Y. Pan, L.L. He, X. Sun, and M. S. Dresselhaus: Appl. Phys. Lett. **72**, 3282 (1998)
131. L. Ci, S. Xie, D. Tang, X. Yan, Y. Li, Z. Liu, X. Zou, W. Zhou, and G. Wang: Chem. Phys. Lett. **349**, 191 (2001)
132. P. Nikolaev, M.J. Bronikowski, R.K. Bradley, F. Rohmund, D.T. Colbert, K.A. Smith, and R.E. Smalley: Chem. Phys. Lett. **313**, 91 (1999)
133. B.C. Satishkumar, A. Govindaraj, R. Sen, and C.N.R. Rao: Chem. Phys. Lett. **293**, 47 (1998)
134. H.W. Zhu, C.L. Xu, D.H. Wu, B.Q. Wei, R. Vajtai, and P.M. Ajayan, Science **296**, 884 (2002)
135. R.R. Bacsa, C. Laurent, A. Peigney, W.S. Bacsa, T. Vaugien, and A. Rousset: Chem. Phys. Lett. **323**, 566 (2000)

136. E. Flahaut, A. Govindaraj, A. Peigney, C. Laurent, A. Rousset, and C.N.R. Rao: Chem. Phys. Lett. **300**, 236 (1999)
137. E. Flahaut, A. Peigney, C. Laurent, and A. Rousset: J. Mater. Chem. **10**, 249 (2000)
138. A. Govindaraj, E. Flahaut, C. Laurent, A. Peigney, A. Rousset, and C.N.R. Rao: J. Mater. Res. **14**, 2567 (1999)
139. C. Laurent, A. Peigney, and A. Rousset: J. Mater. Chem. **8**, 1263 (1998)
140. A. Peigney, C. Laurent, F. Dobigeon, and A. Rousset: J. Mater. Res. **12**, 613 (1997)
141. Y.S. Ning, X.B. Zhang, Y.W. Wang, Y L. Sun, L.H. Shen, X.F. Yang, and G. Van Tendeloo: Chemical Physics Letters **366**, 555 (2002)
142. V. Ivanov, J.B. Nagy, P. Lambin, A. Lucas, X B. Zhang, X.F. Zhang, D. Bernaerts, G. Van Tendeloo, and S. Amelinckx: Chem. Phys. Lett. **223**, 329 (1994)
143. B. Kitiyanan, W.E. Alvarez, J.H. Harwell, and D.E. Resasco: Chem. Phys. Lett. **317**, 497 (2000)
144. L.F. Sun, J.M. Mao, Z.W. Pan, B.H. Chang, W Y. Zhou, G. Wang, L.X. Qian, and S.S. Xie: Appl. Phys. Lett. **74**, 644 (1999)
145. F. Benissad, P. Gadelle, M. Coulon, and L. Bonnetain: Carbon **26**, 61 (1988)
146. M. J. Yacaman, M. M. Yoshida, L. Rendon, and J.G. Santiesteban: Appl. Phys. Lett. **62**, 657 (1993)
147. A. Fonseca, K. Hernadi, P. Piedigrosso, J.F. Colomer, K. Mukhopadhyay, R. Doome, S. Lazarescu, L.P. Biro, P. Lambin, P. A. Thiry, D. Bernaerts, and J.B. Nagy: Appl. Phys. A: Mater. Sci. Process. A **67**, 11 (1998)
148. A. Kukovecz, Z. Konya, N. Nagaraju, I. Willems, A. Tamasi, A. Fonseca, J.B. Nagy, and I. Kiricsi: Phys. Chem. Chem. Phys. **2**, 3071 (2000)
149. P. Chen, X. Wu, J. Lin, H. Li, and K.L. Tan: Carbon **38**, 139 (2000)
150. P. Chen, H.B. Zhang, G.D. Lin, Q. Hong, and K.R. Tsai: Carbon **35**, 1495 (1997)
151. S. Delpeux, K. Szostak, E. Frackowiak, S. Bonnamy, and F. Beguin: Journal of Nanosc., and Nanotech. **2**, 481 (2002)
152. Y. Soneda, L. Duclaux, and F. Beguin: Carbon **40**, 965 (2002)
153. L.C. Qin: J. Mater. Sci. Lett. **16**, 457 (1997)
154. R. Sen, A. Govindaraj, and C.N.R. Rao: Chem. Phys. Lett. **267**, 276 (1996)
155. C.N.R. Rao, R. Sen, B.C. Satishkumar, and A. Govindaraj: Chem. Commun., 1525 (1998)
156. C. Emmenegger, P. Mauron, A. Zuttel, C. Nutzenadel, A. Schneuwly, R. Gallay, and L. Schlapbach: Appl. Surf. Sci. **162-163**, 452 (2000)
157. M. Terrones, N. Grobert, J.P. Zhang, H. Terrones, J. Olivares, W.K. Hsu, J.P. Hare, A.K. Cheetham, H.W. Kroto, and D.R.M. Walton: Chem. Phys. Lett. **285**, 299 (1998)
158. B.Q. Wei, Z.J. Zhang, P.M. Ajayan, and G. Ramanath: Carbon **40**, 47 (2002b)
159. C.J. Lee, S.C. Lyu, Y. R. Cho, J.H. Lee, and K.I. Cho: Chem. Phys. Lett. **341**, 245 (2001)
160. C.J. Lee and J. Park: Carbon **39**, 1891 (2001)

161. C.J. Lee, J. Park, S.Y. Kang, and J.H. Lee: Chem. Phys. Lett. **326**, 175 (2000)
162. H. Ago, T. Komatsu, S. Ohshima, Y. Kuriki, and M. Yumura: Appl. Phys. Lett. **77**, 79 (2000)
163. R. Andrews, D. Jacques, A.M. Rao, F. Derbyshire, D. Qian, X. Fan, E.C. Dickey, and J. Chen: Chem. Phys. Lett. **303**, 467 (1999)
164. A.M. Rao, D. Jacques, R.C. Haddon, W. Zhu, C. Bower, and S. Jin: Appl. Phys. Lett. **76**, 3813 (2000)
165. Z.F. Ren, Z.P. Huang, J.W. Xu, J.H. Wang, P. Bush, M.P. Siegel, and P.N. Provencio: Science **282**, 1105 (1998)
166. G.W. Ho, A.T.S. Wee, J. Lin, and W.C. Tjiu: Thin Solid Films **388**, 73 (2001)
167. H. Wang, J. Lin, C.H.A. Huan, P. Dong, J. He, S.H. Tang, W.K. Eng, and T.L.J. Thong: Applied Surface Science **181**, 248 (2001)
168. Y.H. Wang, J. Lin, C.H. A. Huan, and G.S. Chen: Appl. Phys. Lett. **79**, 680 (2001)
169. H. Cui, O. Zhou, and B.R. Stoner: J. Appl. Phys.**88**, 6072 (2000)
170. H.M. Cheng, F. Li, X. Sun, S.D.M. Brown, M.A. Pimenta, A. Marucci, G. Dresselhaus, and M.S. Dresselhaus: Chem. Phys. Lett. **289**, 602 (1998)
171. B. Wei, R. Vajtai, Y.Y. Choi, P.M. Ajayan, H. Zhu, C. Xu, and D. Wu: Nano Letters **2**, 1105 (2002)
172. I.W. Chiang, B.E. Brinson, A.Y. Huang, P.A. Willis, M.J. Bronikowski, J.L. Margrave, R.E. Smalley, and R.H. Hauge: J. of Phys.Chem. B **105**, 8297 (2001)
173. W. Zhou, Y.H. Ooi, R. Russo, P. Papanek, D.E. Luzi, J. E. Fischer, M.J. Bronikowski, P.A. Willis, and R.E. Smalley: Chem. Phys. Lett. **350**, 6 (2001)
174. X. Devaux, C. Laurent, and A. Rousset: Nanostruct. Mater. **2**, 339 (1993)
175. A. Peigney, C. Laurent, O. Dumortier, and A. Fousset: J. Eur. Ceram. Soc. **18**, 1995 (1998)
176. A. Peigney, C. Laurent, and A. Rousset: J. Mater. Chem. **9**, 1167 (1999)
177. S. Rul, C. Laurent, A. Peigney, and A. Rousset: J. Eur. Ceram. Soc. **23**, 1233 (2003)
178. A. Peigney, C. Laurent, E. Flahaut, R.R. Bacsa, and A. Rousset: Carbon **39**, 507 (2001)
179. S. Tang, Z. Zhong, Z. Xiong, L. Sun, L. Liu, J. Lin, Z.X. Shen, and K.L. Tan: Chem. Phys. Lett. **350**, 19 (2001)
180. S. Maruyama, R. Kojima, Y. Miyauchi, S. Chiashi, and M. Kohno: Chemical Physics Letters **360**, 229 (2002)
181. W.E. Alvarez, B. Kitiyanan, A. Borgna, and D.E. Resasco: Carbon **39**, 547 (2001)
182. J.E. Herrera, L. Balzano, A. Borgna, W.E. Alvarez, and D.E. Resasco: Journal of Catalysis **204**, 129 (2001)
183. C.L. Cheung, A. Kurtz, H. Park, and C.M. Lieber: Journal of Physical Chemistry B **106**, 2429 (2002)
184. P. Coquay, A. Peigney, E. De Grave, R.E. Vandenberghe, and C. Laurent: J. Phys. Chem. B **106**, 13199 (2002)

185. E. Flahaut, A. Peigney, and C. Laurent: J. Nanosci. Nanotech. **3**, 151 (2003)
186. W. Ren, F. Li, J. Chen, S. Bai, and H.-M. Cheng: Chem. Phys. Lett. **359**, 196 (2002)
187. E. Flahaut, R. Bacsa, A. Peigney, and C. Laurent: Chemical Communications, 1442 (2003)
188. J. Kong, H.T. Soh, A.M. Cassell, C.F. Quate, and H. Dai: Nature **395**, 878 (1998)
189. N.R. Franklin, and H. Dai: Adv. Mater. **12**, 890 (2000)
190. G. Che, B.B. Lakshmi, C.R. Martin, E. R. Fisher, and R. S. Ruoff: Chem. Mater. **10**, 260 (1998)
191. S.-H. Jeong, O.-J. Lee, K.-H. Lee, S.H. Oh, and C.-G. Park: Chemistry of Materials **14**, 1859 (2002)
192. S.S. Xie, B.H. Chang, W.Z. Li, Z.W. Pan, L.F. Sun, J.M. Mao, X.H. Chen, L.X. Qian, and W.Y. Zhou: Adv. Mater. **11**, 1135 (1999)
193. Z.K. Tang, H.D. Sun, J. Wang, J. Chen, and G. Li: Bull. Mater. Sci. **22**, 329 (1999)
194. L. Alvarez, T. Guillard, J.-L. Sauvajol, and G. Flamant, D. Laplaze: App. Phys. A **70**, 169 (2000)
195. H.M. Cheng, F. Li Su, G. Pan, H.Y. Pan, L.L. He, X. Sun, and M.S. Dresselhaus: Appl. Phys. Lett. **2**, 3282(1998)
196. J.-F. Colomer, C. Stéphan, S. Lefrant, G. Van Tendeloo, I. Willems, Z. Konya, A. Fonseca, C. Laurent, and J.B. Nagy, Chem. Phys. Lett. **317**, 83 (2000)
197. J. Gavillet, A. Loiseau, F. Ducastelle, S. Thair, P. Bernier, O. Stéphan, J. Thibault, and J.-Ch. Charlier: Carbon **40**, 1649 (2002)
198. H. Kanzow and A. Ding: Phys. Rev. B **60** (1999) 11 180; H. Kanzow, C. Lenski, and A. Ding: Phys. Rev. B **63**, 125402 (2001)
199. V.L. Kusnetzov, A. N. Usoltseva, A.L. Chuvillin, E. D. Obratzova, J.-M. Bonard: Phys. Rev. B **64**, 235401(2001)
200. A. Gorbunov, O. Jost, W. Pompe, and A. Graff: Carbon **40**, 113 (2002)
201. A. Maiti, C.J. Brabec, and J. Bernholc: Phys. Rev. B **55**, 6097 (1997)
202. J. Gavillet, A. Loiseau, C. Journet, F. Willaime, F. Ducastelle, and J.-Ch. Charlier: Phys. Rev. Lett. **87**, 275504 (2001)
203. J.-Ch. Charlier, G.-M. Rignanese, X. Blas, De Vita, and R. Car: unpublished (2003)
204. J. Gavillet, J. Thibault, O. Stéphan, H. Amara, A. Loiseau, Ch. Bichara, J.-P. Gaspard, and F. Ducastelle: J. Nanosc. and Nanotech. **4**, 346 (2004)
205. A. Loiseau and F. Willaime: Appl. Surface Science **164**, 227 (2000)
206. Y. Saito, M. Okuda, N. Fujimoto, T. Yoshikawa, M. Tomita, and T. Hayashi: Jpn. J. Appl. Phys. 1 **33**, L526 (1994)
207. Y. Saito, M. Okuda, N. Fujimoto, T. Yoshikawa, M. Tomita, and T. Hayashi: Jpn J. Appl. Phys. **33**, 526 (1994) ; Y. Saito: Carbon **33**, 979 (1995)
208. D. Zhou, S. Seraphin, and S. Wang: Appl. Phys. Lett.**65**, 1593 (1994)
209. X . Fan, R. Buczko, A. A. Puretzky, D.B. Geohegan, J.Y. Howe, S.T. Pantelides, and S.J. Pennycook:Phys. Rev. Lett. **90**, 145501 (2003)
210. A.N. Andriotis, M. Menon, and G.E. Froudakis: Phys. Rev. Lett. **85**, 3193 (2000)

211. H. Kataura, Y. Kumazawa, Y. Maniwa, Y. Ohtsuka , R. Sen, S. Suzuki, and Y. Achiba: Carbon **38**, 1691(2000)
212. O. Jost, A.A. Gorbunov, J. Mller, W. Pompe, A. Graff, R. Friedlein, X. Liu, and M.S. Golden, J . Fink: Chem. Phys. Lett. **339**, 297 (2001) ; O. Jost, A.A. Gorbunov, J. Mller, W. Pompe, X. Liu, P. Georgi, L. Dunsch, M.S. Golden,and J . Fink: J. Phys. Chem. B **106**, 2875 (2002)
213. A. Gorbunov, O. Jost, W. Pompe, and A. Graff: Appl. Surface Science **197–198**, 563 (2002)
214. J.S. Langer: Rev. Mod. Phys. **52**, 1 (1980)
215. A. Zangwill: *Physics at surfaces*, (Cambridge University Press 1998)
216. J.-F. Colomer, L. Henrard, Ph. Lambin, and G. Van Tendeloo: Phys . Rev. B **64**, 125425 (2001) ; Eur. Phys. J. B **27**, 111 (2002)
217. A. Loiseau, N. Demoncy, O. Stéphan, C . Colliex,and H. Pascard: In *Science and Applications of Nanotubes* ed Tomanek and Enbody (Kluwer Academic/Plenum Publishers, New York 2000), p1.
218. L. Henrard, A. Loiseau, C. Journet, and P. Bernier: Eur. Phys. J. B **13**, 661 (2000)
219. A. Loiseau, J. Gavillet, F. Ducastelle, J. Thibault, O. Stéphan, P. Bernier, and S. Thair: C. R. Physique **4**, 967 (2003)
220. J. B. Nagy, G. Bister, A. Fonseca, D. Mehn, Z. Konya, I. Kiricsi, Z. E. Horvath, and L. P. Biro: J. Nanosci. Nanotech. **4**, 326 (2004)
221. M. Endo and H.W. Kroto: J. Phys. Chem. **96**, 6941 (1992)
222. R. Saito, M. Fujita, G. Dresselhaus, and M.S. Dresselhaus: Mater. Sci. Eng. B**19**, 185 (1993)
223. R.E. Smalley: Mater. Sci. Eng. B**19**, 1 (1993)
224. S. Iijima, T. Ichihashi, and Y. Ando: Nature **356**, 776 (1992)
225. S. Iijima: Mater. Sci. Eng. B**19**, 172 (1993)
226. A. Maiti, C.J. Brabec, C.M. Roland, and J. Bernholc: Phys. Rev. Lett. **73**, 2468 (1994)
227. L. Lou, P. Nordlander, R.E. Smalley: Phys. Rev. B **52**, 1429 (1995)
228. J.-C. Charlier, A. De Vita, X. Blase, and R. Car: Science **275**, 646 (1997)
229. J.-C. Charlier, X. Blase, A. De Vita, and R. Car: Appl.Phys. A **68**, 267 (1999)
230. Y.-K. Kwon, Y.H. Lee, S.-G. Kim, P. Jund, D. Tománek, and R.E. Smalley:Phys. Rev. Lett. **79**, 2065 (1997)
231. M. Buongiorno Nardelli, C. Brabec, A. Maiti, C. Roland, and J. Bernholc:Phys. Rev. Lett. **80**, 313 (1998)
232. S. Iijima: MRS Bulletin **19**, 43 (1994)
233. D.H. Robertson, D.H. Brenner, and J.W. Mintmire: Phys. Rev. B **45**, 12592 (1992)
234. A. Maiti, C.J. Brabec, C.M. Roland, and J. Bernholc: Phys. Rev. B **52**, 14850 (1995)
235. C.J. Brabec, A. Maiti, C. Roland, and J. Bernholc: Chem. Phys. Lett. **236**, 150 (1995)
236. B.R. Eggen, M.I. Heggie, G. Jungnickel, C.D. Latham, R. Jones, and P.R. Briddon: Science **272**, 87 (1996)
237. Y.H. Lee, S.-G. Kim, P. Jund, and D. Tománek: Phys. Rev. Lett. **78**, 2393 (1997)
238. D.L. Carroll, P. Redlich, P.M. Ajayan, J.-C. Charlier, X. Blase, A. De Vita,and R. Car: Phys. Rev. Lett. **78**, 2811 (1997)

239. Y. Shibuta and S. Maruyama: Chem. Phys. Lett. **382**, 381 (2003)
240. F. Ding, K. Bolton, and A. Rosén: J. Chem. Phys. **121**, 2775 (2004)
241. H. Amara: PhD Thesis, Université Paris 6 (2005)
242. J. Yu et al.: Appl. Phys. Lett. **77**, 1949 (2000)
243. D. Goldberg et al.: Chem. Phys. Lett. **359**, 220 (2002)
244. M. Terrones et al.: Chem. Phys. Lett. **257**, 576 (1996)
245. R. Sen et al.: Chem. Phys. Lett. **287**, 671 (1998)
246. W. Han et al.: Appl.Phys.Lett. **73**, 3085 (1998)
247. D. Golberg et al.: Chem. Phys. Lett. **308**, 337 (1999)
248. D. Golberg et al.: Appl. Phys. Lett. **82**, 1275 (2003)
249. A.Y. Liu et al.: Phys. Rev. B **39**, 1760 (1988)
250. X. Blase et al.: Appl. Phys. A **68**, 293-300 (1999) ; ibid., Comp. Mat. Sci. **17**, 107-114 (2000)
251. M.O. Watanabe, S, Itoh, T. Sasaki, K. Mizushima: Phys. Rev. Lett. **77**, 187 (1996) ; Erratum, Phys. Rev. Lett. **77**, 2846 (1996) ; Y. Chen, J.C. Barnard, R.E. Palmer, M.O. Watanabe, T. Sasaki: Phys. Rev. Lett. **83**, 2406 (1999)
252. X.D. Bai, E.G. Wang, J. Yu, H. Yang: Appl. Phys. Lett. **77**, 67 (2000); J. Yu, J. Ahn, S.F. Yoon, Q. Zhang, Rusli et al.: Appl. Phys. Lett. **77**, 1949 (2000)
253. X. Blase et al.: Appl. Phys. Lett. **70**, 197 (1997)
254. D.L. Carroll et al., Carbon **3**6, 753 (1998)
255. X. Blase et al., Phys. Rev. Lett. **8**3, 5078-5081 (1999)
256. E. Hernández et al., J. Chem. Phys. **1**13, 3814 (2000)
257. D. L. Carroll et al.: Phys. Rev. Lett. 81, 2332-2335 (1998)
258. E. Bengu et al.: Phys. Rev. lett. **86**, 2385 (2001)
259. X. Blase et al., Phys. Rev. Lett. **8**0, 1666 (1998)
260. K.M. Rogers et al, Chem. Phys. Lett. **3**32, 43 (2000)